SOURCE PARAMETERS AND SEISMOTECTONICS OF THE CENTRAL NEW MADRID SEISMIC ZONE

Zuyuan Liu, B.S., M.S.

A Digest Presented to the Faculty of the Graduate School
of Saint Louis University in Partial Fulfillment of
the Requirements for the Degree of
Doctor of Philosophy

1997

DIGEST

The New Madrid Seismic Zone (NMSZ) is the most seismically active area of the central and eastern United States. During the winter of 1811 and 1812, three catastrophic earthquakes (moment magnitude ~ 8) occurred. The possibility of recurrence of such large earthquakes and the greatly increased population of the area provides an impetus for seismotectonics investigation for reducing earthquake hazards. Current seismicity delineates four major fault segments of the NMSZ. The geometry and nature of the active faulting in the central NMSZ are still not well understood.

To understand the seismotectonics of the NMSZ, source parameters were determined, using three-component PANDA data and waveform modeling techniques. These were combined with the JHD relocation to obtain a three-dimensional picture of fault slips.

Body wave propagation in the sediment of the NMSZ was modeled. A wave modeling procedure to determine source parameters was developed. A source parameter data set consisting of focal mechanisms and seismic moments was obtained. A seismotectonic model of the NMSZ was developed. The stress field of this area, the geometry and nature of the active faults in the central NMSZ, as well as the relationship to geologic features were inferred. Seismogenesis of the NMSZ was discussed.

The depth distribution of microearthquake hypocenters indicates a seismic surface that dips to the W or SW with variable dip angle in the central NMSZ. We divided the central NMSZ into three segments.

The SE segment is oriented N30°W, 45°SW and is characterized by thrust type focal mechanisms. A striking NE conjugate fault with right-lateral oblique reverse motion was also found. The central segment strikes NS, dips 30°W and displays thrust mechanisms. The NW segment is a listric fault with a strike N40°W and a dip 70°SW near the surface and 35°SW at depth >10 km. Focal mechanisms along this segment imply left-lateral oblique-reverse slip. The Reelfoot scarp, its northern extension, the Lake County Uplift are the surface expressions of faulting along the central and NW segments. A N84°E maximum horizontal stress was inferred in the central and SE segment by averaging P-axes direction, whereas N65°E maximum horizontal stress was inferred for the northern end of the central NMSZ. At the southern intersection of the central NMSZ with the right-lateral southern axial arm, we observed both right-lateral strike-slip and thrust faulting. Two cross fault systems occur at the northern intersection of the NW segment with the right-lateral N-E arm and the left-lateral westerly arm of the NMSZ. We defined a new active arm of the NMSZ that strikes NE with right-lateral strike-slip that is parallel to the southern axial arm and is located in the southern most of NMSZ. The seismicity in the SE segment of the central NMSZ may be explained by the intersection with the new arm.

The existence of the interpreted weak zone and/or increased pore pressure may be contributing factors for the occurrence of earthquakes of the NMSZ. The stress concentrated around the periphery of the individual intrusions may also be a contributing factor.

EARTHQUAKE MODELING AND ACTIVE FAULTING IN THE NEW MADRID SEISMIC ZONE

Zuyuan Liu, B.S., M.S.

A Dissertation Presented to the Faculty of the Graduate School
of Saint Louis University in Partial Fulfillment of
the Requirements for the Degree of
Doctor of Philosophy

1997

COMMITTEE IN CHARGE OF CANDIDACY:

Professor Robert B. Herrmann,
Chairperson and Advisor

Professor Brian J. Mitchell,

Assistant Professor Charles J. Ammon

Professor David Crossley

ACKNOWLEDGEMENTS

I would like to thank my advisor, Dr. Robert B. Herrmann, for his constant advice and guidance throughout this study. The comments and reviews by Dr. Brian J. Mitchell, Dr. Charles J. Ammon and Dr. David Crossley are greatly appreciated.

I thank Dr. Brian J. Mitchell for his concern and encouragement during my period of study. I wish to express my gratitude to Dr. Jer-Ming Chiu of the University of Memphis for the high quality PANDA data and Dr. J. Pujol of the University of Memphis for sending his JHD relocation results for use in this study.

I also remember and express gratitude to the late Dr. Otto W. Nuttli for inviting me to United States of America, which ultimately led to this work.

Encouragements provided by Dr. Benwen Li are greatly appreciated.

The kind involvement of faculty, staff, and friends at Saint Louis University are also very appreciated. I would like to thank the colleagues and friends at State Seismological Bureau, China for their understanding and support.

Finally, nothing I can say would be enough to express my appreciation to my sister, brother and my daughter for their concern and encouragement in realizing this goal. I shall always remain grateful to my late father and mother who motivated me for this career.

TABLE OF CONTENTS

CHAPTER 1 INTRODUCTION		1
1.1	Research Objectives	1
1.2	Geophysical and tectonic background	7
1.2.1	Introduction	7
1.2.2	Geophysical setting	8
1.2.3	Seismicity and major geophysical features in Reelfoot Rift	13
1.2.4	Seismic refraction and reflection surveys	17
1.2.5	Tectonic setting	19
1.3	The Mississippi Valley Embayment seismicity	26
1.3.1	The New Madrid earthquakes of 1811-1812	27
1.3.2	Paleoseismology, neotectonics and recurrence intervals for large earthquakes	29
1.3.3	Present day seismicity	30
1.3.4	Seismicity surveys	31
1.3.5	The velocity and attenuation model	33
1.3.6	Focal mechanisms and stress field	36
1.3	Summary	39
CHAPTER 2 SYNTHETIC SEISMOGRAMS		41
2.1	Introduction	41
2.2	Cagniard de-Hoop technique	42
2.2.1	Response of shear dislocation sources in a homogeneous half-space	43
2.2.2	High frequency solution for a multilayer problem	52
2.2.3	Full Cagniard solution	55
2.3	Wavenumber-frequency integration	59
2.4	Comparison of techniques	63
CHAPTER 3 INVERSION FOR FAULTING PARAMETERS		68
3.1	Grid search inversion	68
3.2	Moment tensor inversion	72
3.2.1	The moment tensor	72
3.2.2	Moment tensor inversion	79
3.3	Confidence limits and data importance	82
3.3.1	Introduction	82
3.3.2	Application of confidence limit to the study	86

3.4 Maximum normalized cross-correlation coefficient and the smallest sum of squares between observed and predicted waveforms 88
3.5 Data processing 93

CHAPTER 4 EARTHQUAKE SOURCE PARAMETERS AND SEISMOTECTONICS 100

4.1 Introduction 100
4.2 Focal mechanisms of the central NMSZ 105
4.2.1 Microearthquake distribution with depth 105
4.2.2 Focal mechanisms and active faulting 105
4.2.3 A new structure in the South NMSZ 128
4.2.4 Stress field analysis of the central NMSZ 130
4.2.5 Seismic moment 132
4.3 Discussion 134
4.3.1 A seismotectonic model 135
4.3.2 Seismogenesis of the NMSZ 140
4.4 Summary 141

CHAPTER 5 CONCLUSIONS 145

5.1 Contributions of this study 145
5.2 Future research areas 146

BIBLIOGRAPHY 152

VITA AUCTORIS 164

LIST OF FIGURES

1.1 The location of New Madrid Seismic Zone in the USA. The heavy black square roughly outlines the working area in this study. 2

1.2a Relationship of earthquake epicenters, plutons, rift boundaries, faults, and major geologic features in the northern Mississippi Embayment region (Hildenbrand and Hendricks, 1995). 4

1.2b Seismicity (1974-1995) and focal mechanisms of larger earthquakes of the New Madrid Seismic Zone. The four major seismicity patterns and the nature of three of them were defined by Stauder *et al*., (1976), Herrmann (1979) and Herrmann and Ammon (1997). 0907 was estimated in this study. 6

1.3 Regional geophysical features. Black bodies represent dense, magnetic plutons of Ordovician-Cretaceous age (except the Bloomfield pluton, which may be Cambrian or older). Gray bodies denote intrusive complexes of Cambrian through Cretaceous age. Igneous bodies A-P and V produce anomalies: A and C-F: Arkansas transform fault; C: Magnet Cove and Little Rock; G, N, O, and P: intrusive complexes within the graben; M: Bloomfield pluton; L, K, J, H: the boundary intrusive bodies. PGL, Paducah gravity lineament; SCML, south-central magnetic lineament (Hildenbrand and Hendricks, 1995). 9

1.4 Shaded-relief map of the first-vertical derivative of the reduced-to-pole magnetic anomaly data. Illumination is from the west (Hildenbrand and Hendricks, 1995). 11

1.5 Complete Bouguer gravity map of the New Madrid seismic zone with earthquake epicenters and boundaries of major geophysical features. Open triangles denote earthquake epicenters detected by the Missouri Valley regional seismic network from 1975 to 1991. Letters B, I to S, and V represent anomalies discussed in text. MTC, DNM, and NMC denote seismic zones. PGL represents the Paducah gravity lineament. Dashed lines are the approximate boundaries of the igneous complexes within the graben, expressed as anomalies O and N. M: Bloomfield pluton (Hildenbrand and Hendricks, 1995). 15

1.6 Regional geology and previous seismic experiments. Lines 1 and 2 are refraction lines [Steinhard and Meyer, 1961; McCamy and Meyer, 1966]. Lines 3 and 4 are Consortium for Continental Reflection Profiling (COCORP) reflection lines (Nelson and Zhang, 1991). Lines 5 and 6 are reflection lines [McKeown *et al*, 1990]. All the other lines are from the U. S. Geological Survey (USGS) 1990 refraction project (Ginzburg *et al*., 1983; Mooney *et al*.; 1983; Hamilton and Mooney, 1990). The locations of a number of additional shorter reflection lines are given by Nelson and Zhang (1991) (Liao and McMechan, 1996). 18

1.7 Structural setting of the New Madrid seismic zone (Johnston and Schweig, 1996). 22

1.8 The Kentucky (or New Madrid) bend of the Mississippi River in 1812, showing river locations of the principal eyewitnesses to the F1 earthquake (all were in the Kentucky bend area). Dash-dot line shows the 1995 river course (approximate centerline). The Reelfoot scarp has barbs on the hanging wall block and is dotted where inferred. Note that present-day New Madrid is ~ 2 km north of its 1812 location. Locations C-C' are profile endpoints for Figure 1.9 (Johnston and Schweig, 1996). 24

1.9 (a) Topography of Reelfoot scarp from locations C to C' (Figure 1.8). The elevation profile is shown relative to the inferred master thrust fault for event F1, but this crustal profile has no vertical exaggeration. There are no data that show Reelfoot fault through the P_z section; also no hypocenters are located there. (b) A similar geometry and relationship between elevation change and a shallow-dipping thrust rupture plane for the 1964 M 9.2 Alaska earthquake. The box RF shows the size of the Reelfoot fault profile in (a) at this scale. (Johnston and Schweig, 1996). 25

2.1 Cagniard de-Hoop contour in the complex p-plane, (a) given by (2.2.8) is shown in the complex p-plane, beginning at t = 0 on the negative real p-axis, turning on to a branch of a hyperbola at t = R/β, and continuing into the first quadrant. (b) for a receiver at post-critical distance (From Aki and Richards, 1980). 53

2.2a Synthetics at distance of 9.7 km using wave-number integration technique. 66

2.2b Synthetics at distance of 9.7 km using Cagniard de-Hoop technique. 67

3.1 Definition of the Cartesian coordinates (x1,x2,x3) and (x = x_1, y = x_2, z = x_3). The origin is at the epicenter. Strike is measured clockwise from north, dip from horizontal down, and slip counterclockwise from horizontal. u and μ are the slip vector and fault normal, respectively (modified after Aki and Richards, 1980) 74

3.2 Nine generalized couples representing M_{pq} in (3.2.2) (modified after Aki and Richards, 1980). 77

3.3a The result of grid search for event 1103. The arrow shows the focal mechanism (strike=355°, dip=60°, and rake=65°) of the smallest misfit between synthetic and observed P-, SV-, and SH- amplitudes. The angle between arrow and horizontal line (anticlockwise) is rake. The shading area suggests the focal parameters with a 90%, 95% and 99% confidence of F-test, respectively. 89

3.3b P- and T- axes of the event 1103 using grid search. The circle shows the best source parameter. The dark, light gray and gray area correspond to the 90%, 95%, and 99% confidence bounds of the F-test, respectively. 90

3.3c The smallest misfit focal mechanism of event 1103. The compressional P-wave observations are shown by +. The projection is lower hemisphere. 91

3.3d Comparison between 3-component observed and synthetic velocity seismograms of event 1103 at 5 stations. The length of each time history is 4.25 sec. P-, SV- and SH-amplitudes used in the inversion are indicated by circles. Synthetic seismograms were obtained by using the corresponding focal parameters in Figure 3.3c, which were obtained from 9 stations' data. The number by each trace is the maximum velocity (cm/s). The direct P-, SV- and SH-wave amplitudes, even some converted phases (PS, SP which were not used in the inversion) of synthetic seismograms are consistent with those of observed seismograms. 88

3.4a The result of grid search of event 0647. The arrow shows the focal mechanism (strike=135°, dip=55°, and rake=10°) of the smallest misfit between synthetic and observed P-, SV-, and SH-amplitudes. The angle between arrow and horizontal line (anticlockwise) is rake. The dark, light gray and gray suggests the focal parameters with a 90%, 95% and 99% confidence of F-test, respectively. 88

3.4b P- and T- axes of the event 0647 using grid search. The circus shows the best focal parameter. The dark, light gray and gray area are corresponding the 90%, 95%, and 99% confidence of F-test, respectively. 88

3.4c The smallest misfit focal mechanism of event 0647. Compression qudrad rants was shown by +. The projection is lower hemisphere. 88

3.4d Comparison between 3-component observed and synthetic velocity seismograms of event 0647 at 5 stations. The length of each time history is 4.25 sec. Synthetic seismograms were obtained by using the corresponding focal parameters in Fig.3.4c, which were obtained from 9 station data. The number by each trace is the maximum velocity value (cm/s). The P-, SV- and SH-, even some converted phases (PS, SP which were not used in the inversion) of synthetic seismograms are consistent with those of observed seismograms. 88

4.1 Seismicity (1974-1995) and focal mechanisms of larger earthquakes of the New Madrid Seismic Zone (Herrmann and Canas, 1978; Hermann and Ammon, 1997). 0907 was determined in this study. The four major seismicity patterns and the nature of three of them were defined (Stauder *et al*. 1976; Herrmann *et al*. 1978). 101

4.2 PANDA locations and seismicity of the NMSZ during the period of Oct. 1989 - Dec. 1992 determined by CERI. 103

4.3 JHD hypocenters of the central NMSZ. The relationship between focal mechanisms and JHD hypocenters will be studied in the 7 parts: SE segment, southern intersection, central segment, NW segment, westerly arm, N-E arm, and southern axial arm. 104

4.4 The depth distribution of hypocenters: white : 4-7 km, gray: 7-10 km, black: 10-12 km and 54 focal mechanisms. The distribution of the shallow earthquakes is along the east boundary of the NMSZ, also the shallow events show some NE striking zone parallel to the SW axial seismic arm. Focal mechanism color and size indicate the focal depth and magnitude (m_{Lg} = 1.5-4.6). Dilatation quadrants are shown by white; the projection is lower hemisphere. Note the different styles of faulting in different segments of the central NMSZ. 105

4.5a Focal mechanisms of 7 events at SE segment of the central NMSZ determined using waveform modeling. 108

4.5b Focal mechanisms and hypocenters of the central NMSZ, the SE segment (white), will be discussed in detail in Figure 4.5c. 109

4.5c Cross section of earthquake hypocenters with strike N30°W and projection of the focal mechanisms onto a vertical plane. This picture clearly defines two conjugate faults. One striking N30°W and dipping 45°SW is a principal structure, which is a reverse fault. The other strikes NE and dips SE, which is a right-lateral oblique reverse fault. Upper left corner shows a surface view of projected area and all events which will be projected to the central line. All projection information is on the upper caption. 110

4.6a Focal mechanisms of 15 events at the southern intersection. Two major styles of strike-slip and reverse faulting are shown. The mechanism of 0308 indicates a typical right-lateral strike-slip faulting at SW axial arm. See caption of Figure 4.5a. 112

4.6b The focal mechanisms and hypocenters of the central NMSZ, southern intersection (white), will be discussed in detail in Figure 4.6(c). 113

4.6c Cross section of earthquake hypocenters with strike N30°W and the vertical plane focal mechanism projections of 15 events at southern intersection. Most of the activity occurred on or above a plane striking NNW and dipping ~40°SW, which defines a thrust faulting, most strike-slip motion occurred on the hanging wall of the thrust fault. 114

4.6d Azimuthal variations in source duration from empirical Green's function method (data from Xie *et al*, 1997). Note the narrow source duration (i01, o11, i09) and the higher amplitudes in N-NNW direction and wider width (i18, i19) in South. This indicates the direction of the rupture is toward the northwest. 115

4.7a The focal mechanisms and hypocenters of the central NMSZ, SW axial arm (white), will be discussed in detail in Figure 4.7(b). 116

4.7b Cross projection along central line of SW axial arm (N30°W) indicates a vertical fault with width ~ 8 km and depth 2-10 km. Focal mechanisms for 0308, 1130, 0114, 0647, 0003, and 0004 show the vertical nodal planes, which supports concluding that the axial arm is a right-lateral strike-slip fault. 117

4.8a The focal mechanisms and hypocenters of the central NMSZ. The central segment (black) will be discussed in detail in Figure 4.8c. 118

4.8b Focal mechanisms at the central segment (white)of NMSZ. Complex focal mechanisms are observed. The mechanisms of 0928, 1446, 0213, 1335 and 0235 suggest the central segment is a major thrust fault. The strike-slip motions may reflect interaction with nearby seismic faults (see text). 119

4.8c Cross section of earthquake hypocenters with strike North in the area between Northern and southern intersections. A structure striking north and dipping 35°W was defined clearly. The projection of the focal mechanism onto the vertical plane of 1446, 1335, 0928, 0235 and 0213 suggest the structure is thrust fault. The lack of agreement between the nodal plane and the seismicity pattern are also observed. This indicates the strong effect of neighboring faults. 120

4.9a Focal mechanisms at the NW segment. Note the horizontal NE trending P-axis and the major vertical nodal planes striking NW with left-lateral strike-slip motion, which parallel the seismic pattern. 123

4.9b The focal mechanisms and hypocenters of the central NMSZ, NW segment (white), will be discussed in detail in Figure 4.9c. 124

4.9c Cross section of earthquake hypocenters with strike N40°W in the NW segment suggests a listric structure striking N40°W dipping ~70°SW near surface and ~35°SW in depth > 9 km. The projection of the focal mechanism onto the vertical plane of 0429, 0431, 0435, 0441 (all depths<5 km) indicate a reverse motions with large left-lateral slip on a vertical nodal plane striking NW. Those of 0823, 0830, 1839, 1507, 1548 suggest left-lateral oblique reverse motion on similar striking nodal planes with smaller dip angles with deeper depth than that of 04 events. Those of 2250 and 0911 show major reverse faulting on similar striking plane. 125

4.10a The focal mechanisms and hypocenters of the central NMSZ, westerly arm (white), will be dicsussed in detail in Figure 4.10b. 126

4.10b Cross section perpendicular to N80°W suggests the westerly arm is a narrow vertical (width ~4 km) fault striking ~NWW with left-lateral strike-slip motion. 127

4.11a Focal mechanisms and hypocenters of the central NMSZ, N-E arm (white), will be discussed in detail in Figure 4.11b." 128

4.11b Cross section perpendicular to N20°E indicates the NE arm is a vertical fault with width of 8 km and depth 4 - 14 km. Vertical plane projections of 1057 and 1844 suggest this is a right-lateral strike-slip fault. 129

4.12 Focal mechanism of 0907, total 45 P-first motions from PANDA and regional networks are used. The focal mechanism is similar to those of SW axial arm. 131

4.13a Projection of P-axis onto horizontal. The length of the projected bar is proportional to the degree that the axis is horizontal, e.g., a vertical axis has zero length. Note the uniform orientations. 132

4.13b Projection of T-axis onto horizontal. The length of the projected bar is proportional to the degree that the axis is horizontal, e.g., a vertical axis has zero length. Note the somewhat uniform orientations. 133

4.14 Relationship between M_0 and m_{Lg}. 134

4.15 A sketch map of seismotectonic model of the NMSZ (Herrmann and Canas *et al*. 1978; Herrmann, 1979; Herrmann and Ammon, 1997 and this study) 136

LIST OF TABLES

3.1	Results of moment tensor inversion of event 1103.	83
3.2	Range of focal mechanisms with 90% confi dence.	88
3.3	Table 3.3 Velocity and attenuation model in New Madrid Seismic Zone	98
3.4	Reliability test of method.	99
4.1	Locations and source parameters of microearthquakes in the central NMSZ	102

CHAPTER 1

INTRODUCTION

1.1 Research Objectives

The New Madrid Seismic Zone (NMSZ) lies within the Mississippi Valley of the central United States of America (Figure 1.1). The main goal of this study is to determine the focal mechanisms and seismic moment of the microearthquakes in the central NMSZ using three-component PANDA (Portable Array for Numerical Data Acquisition) data and waveform modeling techniques. The spatial distribution of microearthquakes was defined by Joint Hypocenter Determination (JHD) relocation techniques (Pujol, 1997). The stress field of this area, the geometry and style of the active faults of the central NMSZ will be obtained. Finally, a seismotectonic model will be developed according to a well defined three dimensional picture of fault slip. A further goal is to determine the attenuation of body waves in the shallow sediment of this region (Liu *et al*. 1994). A systematic seismotectonics study will provide direct information for strong ground motion estimation and seismic hazard analysis in the NMSZ area.

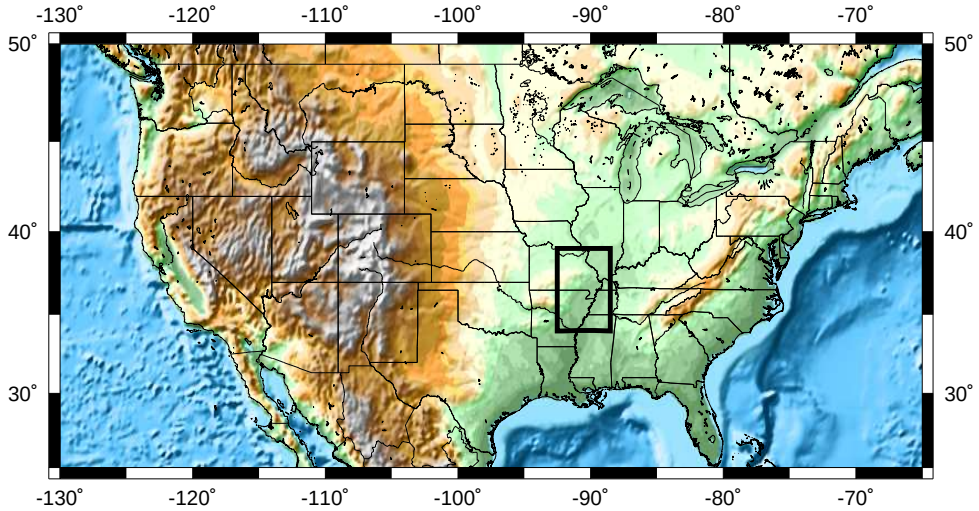

Fig. 1.1. The location of New Madrid Seismic Zone in the USA. The heavy black square roughly outlines the working area in this study.

Four aspects make this study important. (1), the NMSZ is the most seismically active area of the central and eastern United States. During winter of 1811 and 1812, three catastrophic earthquakes, with moment magnitude 8.1 (16 December, 1811), 7.8 (23 January, 1812), 8.0 (07 February, 1812) (Nuttli, 1973b, 1974, 1981a, b; Nuttli and Herrmann, 1984; Nuttli and Zollweg, 1974; Mitchell *et al*. 1991; Johnston, 1996; Johnston and Schweig, 1996) occurred in the NMSZ. The strong ground motion of the 07 February, 1812 breached the Mississippi River in three places. It made the river run backward through a sharp bend near New Madrid, and for a spectacular moment created a roaring waterfall. The three earthquakes were felt throughout much of the U.S. and as far away as Quebec (Nuttli, 1973). From paleoseismology studies, pre 1811-1812 earthquakes (magnitude ≈ 8) have been found. These studies confirm that the 1811-1812 earthquakes were not one-time events (Johnston and Schweig, 1996). Because of regional

seismic monitoring in and around this area since 1974, more than 4000 earthquakes with magnitude > 1.5 have been located. This indicates that the NMSZ recently still quite active.

The governing tectonic structure of the area is a continental rift (Figure 1.2a) estimated to be of late Precambrian age. Worldwide, all large (M>7) continental interplate earthquakes appear to occur in such extensional rifting tectonics (Johnston *et al*. 1994, 1996). The possibility of recurrence of such large earthquakes and the greatly increased population of the area provides an impetus for ground motion estimation and seismic hazard analysis, which depend on the knowledge of earthquake parameters and earth structure. Unlike the San Andreas fault, however, no direct surface faulting evidence is available because thick sediment layer covers the Mississippi Embayment. Therefore, a systematic focal mechanism study of microearthquakes in this area will provide direct information on regional seismotectonics.

(2), current seismicity delineates four major fault segments of the New Madrid Seismic Zone (Figure 1.2b). Seismicity, cross faulting, morphologic and geologic features make the 70 km long central part of the NMSZ a interesting seismicity segment. Two major northeast-striking zones with right lateral strike-slip movement may cause strong compression in the New Madrid left step. Segall and Pollard (1980) suggested that these left steps store elastic strain energy and may be sites of large earthquakes. The earthquake (M = 8.0) of Feb. 07, 1812 occurred here (Johnston and Schweig, 1996). However, the geometry and nature of the active faulting of the central NMSZ remain

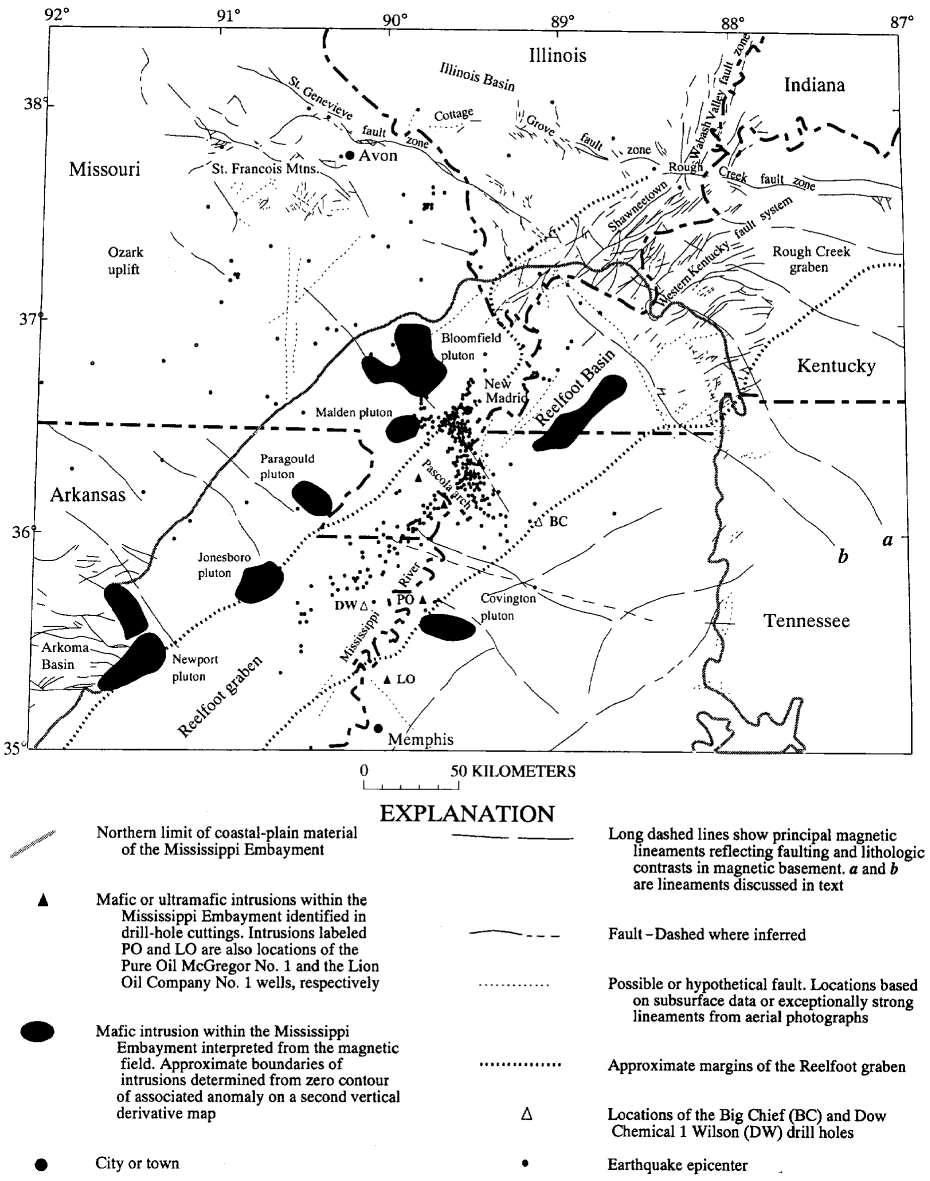

Fig. 1.2a. Relationship of earthquake epicenters, plutons, rift boundaries, faults, and major geologic features in the northern Mississippi Embayment region (Hildenbrand and Hendricks, 1995).

unclear. Therefore, I focus on the central part of the NMSZ, its behavior of active faulting, and the relationships between the active faulting and the regional stress field, morphologic, geology and seismicity.

Because interaction of adjacent fault segments may lead to variable stress pattern which may be reflected in focal mechanisms, this focal mechanism study may define the mechanical relations between the distinct seismicity segments, and therefore result in better understanding of the processes of cross faulting in the left-step area.

(3), previous focal mechanism studies show a somewhat complex picture in the central segment of the NMSZ. A number of authors have obtained very different focal mechanisms using only P-first motion (Herrmann and Canas, 1978; Herrmann, 1979; Andrews *et al.*, 1984; Nicholson *et al*. 1984; Yang *et al.*, 1994). The limited focal sphere coverage makes the focal mechanisms of small earthquakes suspect. In this study, we shall try to get the best focal mechanisms using waveform modeling techniques using recent velocity and attenuation models. The spatial distribution of the microearthquakes was determined using JHD relocation (Pujol, 1997). The 40 three-component PANDA stations, operated by CERI (The Center for Earthquake Research and Information) of University of Memphis (Chiu *et al*., 1992) working during a 3 year period, provides high quality digital observations. I combine focal mechanisms with precise hypocenter of determinations to examine earthquake mechanisms in three-dimensions.

(4), the NMSZ is located in a failed rift system of the Mississippi Embayment. the unusual seismicity of the NMSZ in relation to the central United States makes it important to understand earthquake and faulting in relation to the typical intraplate earthquake system.

New Madrid Seismic Zone

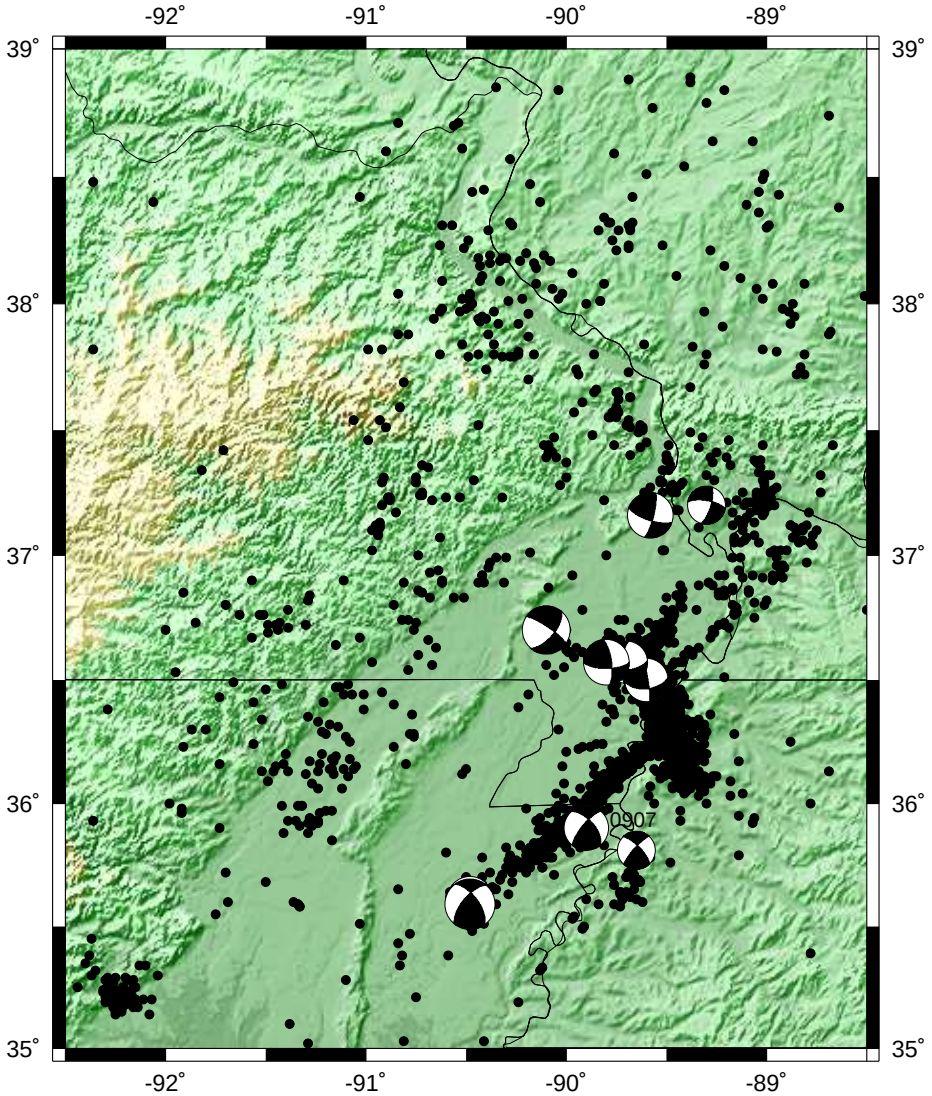

Fig. 1.2b. Seismicity (1974-1995) and focal mechanisms of larger earthquakes of the New Madrid Seismic Zone. The four major seismicity patterns and the nature of three of them were defined by Stauder *et al*., (1976), Herrmann (1979) and Herrmann and Ammon (1997). 0907 was estimated in this study.

In the following review I provide the seismological, geophysical and tectonic background for this study. The review also places the contribution of this study in the larger perspective of earthquake studies.

1.2 Geophysical and tectonic background

1.2.1 Introduction

Magnetic and gravity data together delineate an ancient rift system that may be related to the cause of present day earthquakes in the Mississippi Embayment area (Hildenbrand, 1982; Hildenbrand and Hendricks, 1995; Hildenbrand *et al*. 1996). Burke and Dewey (1973) suggested that the Mississippi Embayment originated as a Mesozoic failed-arm rift. Ervin and McGinnis (1975) synthesized gravity with seismic refraction, stratigraphic, and petrologic data and suggested that the rift, which they called the Reelfoot rift, was formed in late Precambrian or early Paleozoic time and was reactivated in the Cretaceous (Cordell, 1977) indicating a "fossil rift cushion" at the base of the crust. Such an anomalously dense, lower crustal layer is compatible with interpretations based on the explanation of seismic refraction data by McCamy and Meyer (1966), and on the correlation of seismic refraction and gravity data by Mooney *et al*. (1983).

The Reelfoot rift possibly developed along a preexisting shear zone in early Paleozoic time and extends from east-central Arkansas to

western Kentucky, where it seems to merge with the Rough Creek grabens (Hildenbrand, 1985; Hildenbrand and Hendricks, 1995). The near-surface manifestation of the rift is defined as Reelfoot graben (Hildenbrand, 1985), which contains the area of principal present-day seismicity (Figure 1.2a,b).

1.2.2 Geophysical setting

Since 1974, detailed aeromagnetic and gravity surveys in the northern Mississippi Embayment and surrounding region were initiated by the U.S. Geological Survey to delineate structures that may be responsible for the seismicity (Hildenbrand, 1985). The magnetic and gravity data provide a geologic picture of the subsurface that indicates a long and complex tectonic and magmatic history. Different tectonic processes during and subsequent to the formation of the Reelfoot rift have produced three distinct regions with comparatively different structures (Hildenbrand and Hendricks, 1995): southern terminus, central section and northern terminus (Figure 1.3).

1) Southern terminus

The Reelfoot rift developed during the late Proterozoic-early Paleozoic opening of the Iapetus (proto-Atlantic) Ocean. In Hendricks (1988) model, the proto-North American continent began to breakup near the beginning of Cambrian time to form a passive margin along the eastern and southern edge of the present-day craton. In

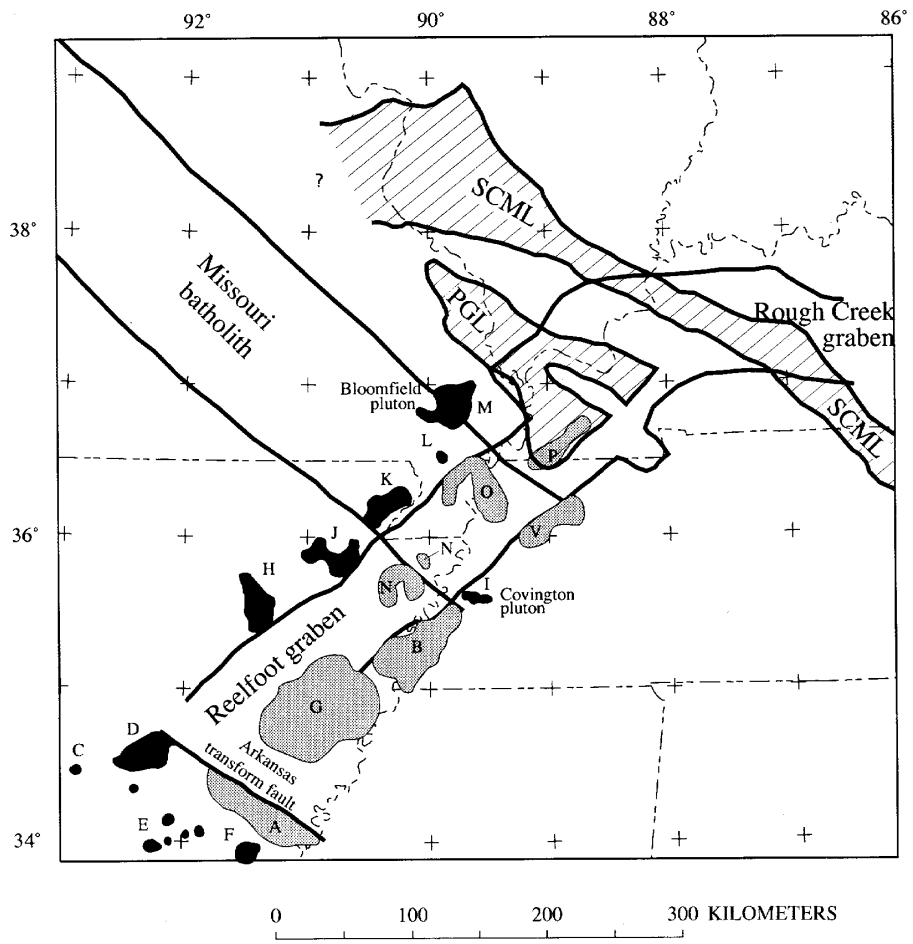

Fig. 1.3. Regional geophysical features. Black bodies represent dense, magnetic plutons of Ordovician-Cretaceous age (except the Bloomfield pluton, which may be Cambrian or older). Gray bodies denote intrusive complexes of Cambrian through Cretaceous age. Igneous bodies A-P and V produce anomalies: A and C-F: Arkansas transform fault; C: Magnet Cove and Little Rock; G, N, O, and P: intrusive complexes within the graben; M: Bloomfield pluton; L, K, J, H: the boundary intrusive bodies. PGL, Paducah gravity lineament; SCML, south-central magnetic lineament (Hildenbrand and Hendricks, 1995).

southwestern Arkansas, a triple junction was formed in Cambrian time (about 550 Mya). At this junction, the Reelfoot rift and Oklahoma aulacogen represented two of the failed arms and extended into

the craton at high angles from bends in the North American continental margin. A southeast-trending transform fault is referred to here as the Arkansas transform fault in eastern Arkansas (Figure 1.3). This transform fault forms the southern terminus of the Reelfoot rift. The magnetic and gravity high along the northwest-trending Arkansas transform fault (A and C-F, Figure 1.3) delineate mafic or ultramafic intrusions of Cretaceous age at about 1.5 km depth. Two major igneous complexes, Magnet Cove and Little Rock (C and D, Figure 1.3) formed in Late Cretaceous time near the juncture of the Arkansas transform fault and the northwest margin of the Reelfoot graben.

2) Central section

From east-central Arkansas to southwestern Kentucky, the Reelfoot rift is clearly expressed as a north-east-trending, 70 km wide feature with exceptionally linear margins (Figure 1.3). The straight margins of the rift are apparent because of a reduced magnetic field (Figure 1.4) over the rift produced by infilling of nonmagnetic sedimentary rocks of the deep basin formed as the crust was pulled apart. The gravity map highlights the shape of the large valley filled with low-density sedimentary rocks and the flanking dense igneous intrusions. The pronounced magnetic and gravity high along the Reelfoot graben margins represent large igneous plutons or intrusive complexes by Hildenbrand (1985), Hildenbrand and Hendricks (1995). However, in several regions within the graben, igneous intrusive complexes may have been emplaced in Paleozoic rocks. These intrusive complexes are

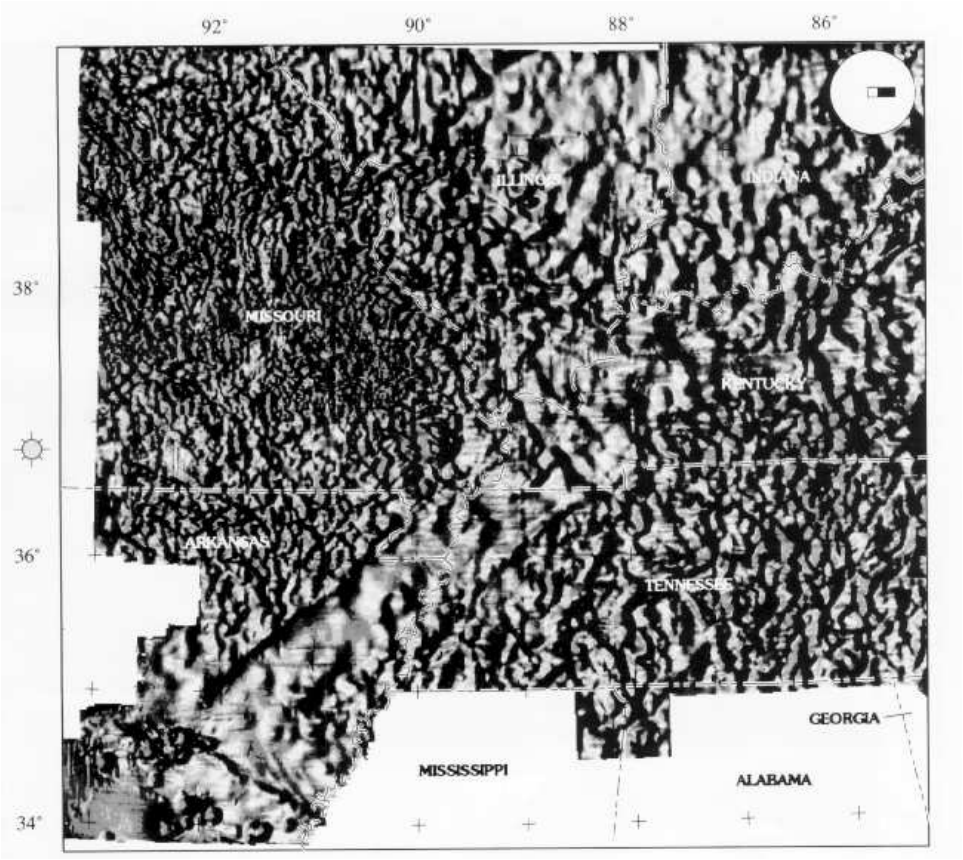

Fig. 1.4. Shaded-relief map of the first-vertical derivative of the reduced-to-pole magnetic anomaly data. Illumination is from the west (Hildenbrand and Hendricks, 1995).

characterized by magnetic and gravity highs (anomalies G, N, O, and P, in Figure 1.3, also M: Bloomfield pluton). For example, seismic reflection data over the igneous intrusions expressed as anomaly O indicate that Precambrian basement is roughly 5 km deep. The average increase in sediment thickness associated with the Reelfoot graben is therefore closer to 4.5 km. As we will discuss, the seismic activity of the New Madrid Seismic Zone is strongly related with the intrusive pluton or complex (Figure 1.3).

The New Madrid Seismic Zone is located where the Reelfoot rift intersects a striking NW-SE gravity feature called the Missouri Gravity Low (MGL, also called Missouri batholith) (Hildenbrand and Hendricks, 1995; Hildenbrand *et al*., 1996), which is a prominent linear gravity low trending SE across Missouri and into the Mississippi Embayment region (Figure 1.3). The magnetic features are parallel to the MGL. The linear surface trends, such as mapped faults, folds, and linear features, follow the MGL. The gravity low probably resulted from an crustal, lower density, 11 km-thick batholith, called the Missouri batholith (Hildenbrand, 1995, 1996). The New Madrid Seismic Zone is located in intersection of the MGL and the Reelfoot rift.

In the northern end of the Reelfoot graben, Hildenbrand (1985) modeled the gravity and seismic refraction data and defined an anomalously dense, lower crustal layer at a depth of 26 km beneath the graben. The crust-mantle boundary in this part of the Midcontinent is normally 40 km deep. Anomalous crust reaches a maximum thickness of 18 km beneath the New Madrid Seismic Zone.

3) Northern terminus

Hildenbrand (1982) suggested that the Reelfoot graben continues northeastward in the Mississippi Embayment, eventually merging with or intersecting across the Rough Creek graben in southern Illinois and western Kentucky (Figure 1.3). The Reelfoot and Rough Creek grabens represent two failed rift arms. A third rift arm extended northeastward along the Wabash valley fault system, while

the fourth arm extended northwest near St.Louis (Braile *et al.*, 1982, 1986). They named this entire system and its quadruple junction the New Madrid rift complex (Figure 1.2a). The abrupt change in the trend of the Reelfoot rift (northeast) to the trend of the Rough Creek graben (east) may be due to: 1) rifting that propagated northeastward and then followed existing east-west structures in western Kentucky that represented a path of less resistance, a change in stress from dilatation to shear would cause a trend change; 2) the competent, homogeneous batholithic rocks beneath the eastern flank of the Ozark Uplift may have represented a result of encountering a crustal obstacle, that diverted rift propagation.

At the juncture of the Reelfoot graben and Rough Creek graben, Hildenbrand *et al.*, (1996) defined the PGL (Paducah Gravity Lineament) as a broad, northwest-trending gravity high. The gravity high crosses the bend in the Reelfoot graben as it joins with the Rough Creek graben (Figure 1.5), which may represent a block-faulted region.

1.2.3 Seismicity and major geophysical features in Reelfoot Rift

The major interrelationship between seismicity and geophysics features can be found in Figure 1.5 (Hildenbrand and Hendricks, 1995). These include: 1) many of the epicenters of the New Madrid seismic zone are within the region defined by the intersection of the Missouri Gravity Low and the Reelfoot graben. The correspondence of

seismicity and this intersection is remakable, considering that the only active section along the 400 km long Reelfoot rift axis occurs only within this 100 km-widen intersection zone. Thus, there seems to be an intimate relationship between earthquake occurrence and the intersection zone of the Missouri batholith and the Reelfoot graben (Hildenbrand and Hendricks, 1995; Hildenbrand *et al.*, 1996); 2) another correlation is the widening of seismic zones in the regions underlain by igneous intrusions. Earthquakes between intrusive complexes N and O (dashed lines Figure 1.5) occur in a tight cluster (Hildenbrand and Hendricks, 1995); 3) the Covington and Bloomfield plutons (anomalies I and M) have earthquake concentrations near their edges. In particular, seismicity near the Covington pluton indicates that the southeast margin at the Reelfoot graben is active. The pluton may prevent the development of seismicity. The Bloomfield pluton also appears to influence the distribution of stress: earthquakes occur near its edges but avoid the interior of intrusions, forming two individual arms (Hildenbrand and Hendricks, 1995). Correlations between stress accumulations and large igneous intrusions in the Eastern United States have been discussed by Kane *et al.*, (1981).

Why do earthquakes occur in the northern Mississippi Embayment region? Why do the patterns of earthquakes form 4 arms? There are two possible explanations: first, the existence of the interpreted weak zone at the intersection of the Missouri batholith and the Reelfoot graben may be a contributing factor to the occurrence of earthquakes (Hildenbrand and Hendricks, 1995). Increased pore

Fig. 1.5. Complete Bouguer gravity map of the New Madrid seismic zone with earthquake epicenters and boundaries of major geophysical features. Open triangles denote earthquake epicenters detected by the Missouri Valley regional seismic network from 1975 to 1991. Letters B, I to S, and V represent anomalies discussed in text. MTC, DNM, and NMC denote seismic zones. PGL represents the Paducah gravity lineament. Dashed lines are the approximate boundaries of the igneous complexes within the graben, expressed as anomalies O and N. M: Bloomfield pluton (Hildenbrand and Hendricks, 1995).

pressure may also be a contributing factor (Hildenbrand and Hendricks, 1995; Mitchell *et al*. 1991). Mitchell *et al*. (1991) suggested that the most active portions of the New Madrid fault zone are characterized by low seismic velocities, which can be explained by the presence of interstitial fluids in cracks in the crust. The presence of such fluids may explain why some faults in intraplate regions are active while others are not. Second, seismicity occurs where far-field stress (Zoback and Zoback, 1989) is concentrated. In the intersection of the MGL with Reelfoot graben, the preexisting rift fractures and high pore fluid pressure (McKeown and Diehl, 1994), and different rock types make the intersection zone weak compared to surrounding rocks. The crust weakness permitted larger volumes of magma to intrude and form the local magnetic and gravity highs (Hildenbrand and Hendricks, 1995).

Because the seismicity widens over intrusive complexes O and N (Dashed lines, Figure 1.5), the individual intrusions in these complexes may represent inhomogeneities in a relatively homogeneous granitic crust. Stress may concentrate around the periphery of these individual intrusions (Hildenbrand and Hendricks, 1995). The boundary of the DNM seismic zone (Figure 1.5) closely coincides with the edge of the intrusive complex. Its northeast terminus correlates both with the edge of the intrusions and a corner of the intersection zone. Do stress accumulations at the northeast margin of the Missouri batholith contribute to the abrupt change in trend in seismicity from northeast to northwest (Hildenbrand and Hendricks, 1995)? To the west of New Madrid, the seismic trend changes direction and forms

two arms, and these changes may be controlled by the presence of the Bloomfield pluton, which represents a dense, 35 km-wide homogeneous mass in the upper crust. The resulting preferred directions of strain release parallel the southern and eastern edges of the pluton. Thus, the linear seismic zones change trends to follow paths of less resistance or avoid more competent structures.

1.2.4 Seismic refraction and reflection surveys

The velocity structure of the NMSZ has been the subject of intense study for many years (Figure 1.6). The earliest refraction profiles were described by Steinhart and Meyer (1966), McCamy and Meyer (1966). These SW-NE trending lines were along the NW edge of the Mississippi embayment. A number of seismic reflection lines have been performed by the industry (Howe and Thompson, 1984; McKeown *et al*., 1990; Hamilton and Zoback, 1982) and the Consortium for Continental Reflection Profiling (COCORP) (Nelson and Zhang, 1991). Axial and transverse wide-angle refraction/reflection profiles have been acquired by the USGS (Ginzburg *et al*., 1983; Hamilton and Mooney, 1990). Two orthogonal wide-aperture refraction lines were acquired in the New Madrid Seismic Zone by the U. S. Geological Survey in 1991 (Liao and McMechan, 1996).

The most important contribution of the refraction study by McCamy and Meyer (1966) was that they found the seismic crustal structure of the embayment has the following three anomalous

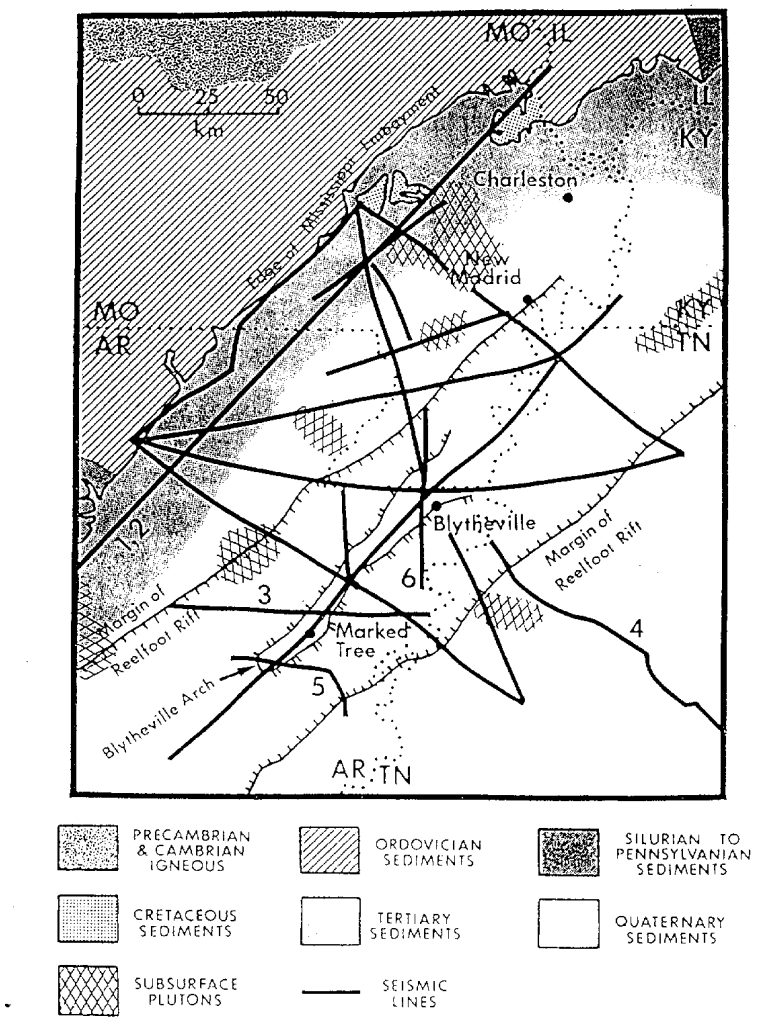

Fig. 1.6. Regional geology and previous seismic experiments. Lines 1 and 2 are refraction lines [Steinhard and Meyer, 1961; McCamy and Meyer, 1966]. Lines 3 and 4 are Consortium for Continental Reflection Profiling (COCORP) reflection lines (Nelson and Zhang, 1991). Lines 5 and 6 are reflection lines [McKeown *et al*, 1990]. All the other lines are from the U. S. Geological Survey (USGS) 1990 refraction project (Ginzburg *et al*., 1983; Mooney *et al*.; 1983; Hamilton and Mooney, 1990). The locations of a number of additional shorter reflection lines are given by Nelson and Zhang (1991) (Liao and McMechan, 1996).

characteristics: 1) the presence of an anomalous velocity layer (7.4 km/sec) at the crust-mantle, 2) the great depth of the mantle (8.1 km/sec, >47 km), 3) the shallowness of the 6.5 km/sec crustal layer. Ervin and McGinnis (1975) synthesized the seismic refraction data, gravity, stratigraphic, and petrologic data and defined a rift evolution model, which they called the Reelfoot rift.

Industry seismic reflection profiles originally defined and mapped the Blytheville Arch (Howe and Thompson, 1984; McKeown *et al*., 1990). Its characteristic signature in these data is a strong upwarp of Paleozoic strata within a ~ 10-15 km wide zone that widens to the northeast and is roughly centered on the axis of the Reelfoot rift. The reflection data suggest that the Reelfoot rift is defined by a series of normal faults that step downward into the center of the embayment. The major fault zone in Paleozoic rocks, with approximately 1-km vertical offset that is associated with the axial seismicity trend.

Other results of refraction and reflection surveys will also be discussed in the "Tectonic setting" section.

1.2.5 Tectonic setting

While we discuss the tectonic setting in the NMSZ area, we only emphasize those that played a prominent role in influencing the 1811-1812 fault ruptures and current seismicity. The fault zones have no surface expressions and were determined based on geophysics and seismic refraction and reflection data.

1) Reelfoot rift: A failed rift

As mentioned above the Reelfoot rift (Figure 1.2a, 1.5), host structure to the New Madrid Seismic Zone, was formed in the period of Late Paleozoic to Early Cambrian times as a failed rift of the opening Iapetus Ocean, predecessor of the present-day Atlantic and Gulf of Mexico. A triple junction was involved (Burke and Dewey, 1973). There are many models for the evolution of the southern North America margin (Mitchell *et al*. 1991; Burke and Dewey, 1973; Thomas, 1991; Hendricks, 1988). The Reelfoot rift is a failed rift arm in all them (Johnston and Schweig, 1996). Establishing the rifted character of the NMSZ crust is of fundamental importance to understanding the earthquake potential of the region, because, worldwide, all large (M ~ 7) stable continental earthquakes occur in crust that experienced such extensional tectonics (Johnston, 1996; Johnston and Schweig, 1996).

2) The Blytheville Arch

The Blytheville Arch was defined by the industry seismic reflection as mentioned above. The cause of the upwarp of the Paleozoic reflectors remains a matters of debate (Johnston and Schweig, 1996), but an axial fault zone at seismogenic depths within the crystalline crust is common (Johnston and Schweig, 1996). The axial fault zone is a first-order feature in the Reelfoot rift evolution. The first event of December 16, 1811 of the 1811-1812 sequence was probably on the axial fault zone (Nuttli, 1973; Johnston and Schweig, 1996). The Blytheville Arch can be divided into two fault segments at Missouri

Bootheel (N36^o). South of this point, called the Blytheville Arch (BA), the arch's upwarped reflectors are present and continuous on seismic reflection profiles; to the north they are absent, but the basement fault zone remains clear, called the Blytheville Fault Zone (BFZ) (Figure 1.7). Johnston and Schweig (1996) believe that this fundamental change in the structure of the Blytheville arch had a major influence on the rupture history of the 1811-1812 earthquakes.

3) The Blytheville Fault Zone (BFZ)

The BFZ (Figure 1.7) is an on-trend continuation of the Blytheville arch to the northeast for ~ 55 km. It is an unintruded extension of the axial fault zone and is coincided with the concentrated zone of seismicity trending northeast across the river. It is important to the fault rupture of 1811-1812 earthquakes because a series of strong aftershocks of 16 Dec 1811 mainshock occurred in Little Prairie, which was close to the BFZ. Johnston and Schweig (1996) suggested the BFZ could continue and intersect the Reelfoot fault at the south-west end of Reelfoot Lake, extending its length to ~ 65 km.

4) Reelfoot scarp, Lake County Uplift and Reelfoot Fault (RF)

The Lake County uplift is a broad, low-amplitude anticline that lies within a left-stepping restraining bend in the NMSZ (Figure 1.8). Most of the current microseismicity in the central NMSZ underlies the Lake County uplift. This seismicity is attributed to strain release along a southwest-dipping reverse fault (RF). The only surface

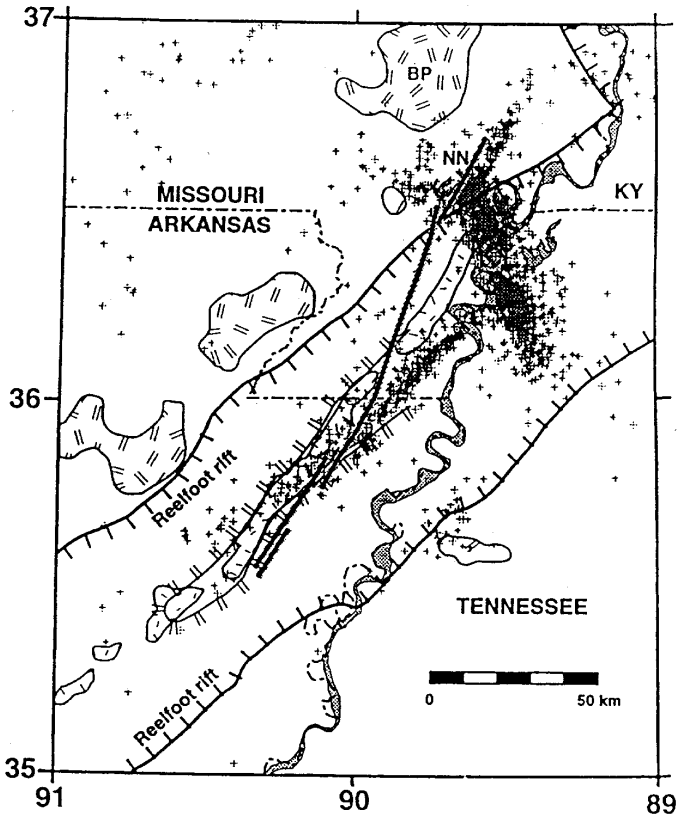

Fig. 1.7. Structural setting of the New Madrid seismic zone (Johnston and Schweig, 1996).

expression of seismic fault, called Reelfoot scarp, was mapped at surface for ~ 32 km (Van Arsdale *et al.*, 1995), and segments of it have been imaged in shallow sediments and in Paleozoic rocks to ~ 3 km depth with a 60 - 70° dip (Sexton and Jones, 1986) using high-resolution seismic reflection profiling. A P- and SH-wave seismic reflection investigation of the Kentucky Bend Scarp (KBS) in the New Madrid

Seismic Zone shows a high-angle reverse fault striking approximately N30° W (Figure 1.8). The Reelfoot scarp is locally 8 m high and has recently been mapped across the Mississippi River into Kentucky and Missouri (Van Arsdale *et al*., 1995). The RF is the deep, seismogenic fault that is expressed at the surface as Reelfoot scarp. It is the only seismogenic fault in the NMSZ with clear surface expression. Chiu *et al*. (1992) suggested a zone of hypocenters dipping ~30° southwest to a depth of 12 to 14 km that may be the seismogenic expression of the RF in the crystalline basement. The surface projection of this zone would reach the surface approximately at the Reelfoot scarp if the $60-70^{o}$ dip (Sexton and Jones, 1986) is used at depths of ≤5 km. (This listric oblique-reverse fault with 70° SW dip near surface and 35° SW dip at depth > 10 km has been found in the northwest extension of the RF in the dissertation). Johnston and Schweig (1996) compared Reelfoot fault and scarp with deformation from the great M 9.2 Alaska earthquake of 1964 (Figure 1.9). They suggested the Reelfoot scarp will grow vertically in response to the regional approximately east-west compressional stress field at the expense of further elevating the eastern portion of the Lake County Uplift. The first upstream waterfall on the Mississippi in the early morning of 7 February, 1812 (F1) indicates a very strong evidence that the Reelfoot scarp through the Kentucky bend area is a surface expression of the historic earthquake of Feb. 7, 1812.

Previous seismic work did not provide the evidence about the movement style of the RF and its northern extension in the

seismogenic depths. These will be major works in the dissertation.

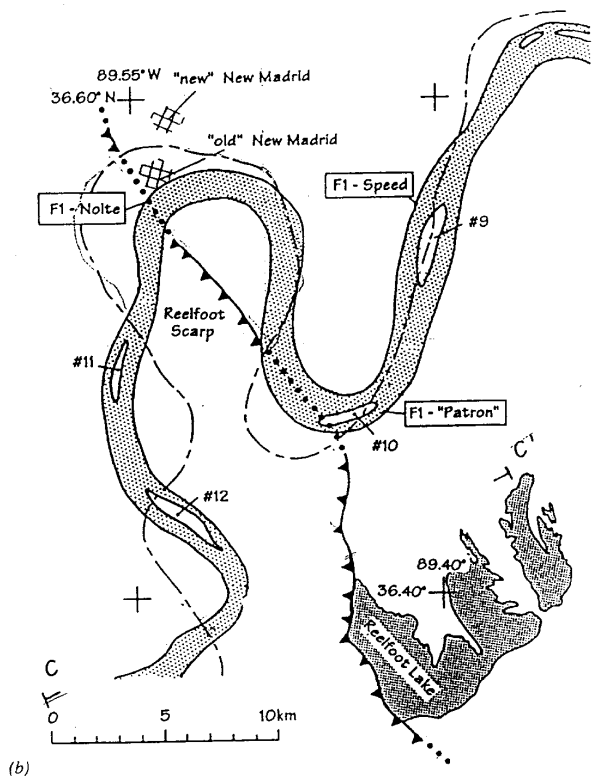

Fig. 1.8. The Kentucky (or New Madrid) bend of the Mississippi River in 1812, showing river locations of the principal eyewitnesses to the F1 earthquake (all were in the Kentucky bend area). Dash-dot line shows the 1995 river course (approximate centerline). The Reelfoot scarp has barbs on the hanging wall block and is dotted where inferred. Note that present-day New Madrid is ~ 2 km north of its 1812 location. Locations C-C' are profile endpoints for Figure 1.9 (Johnston and Schweig, 1996).

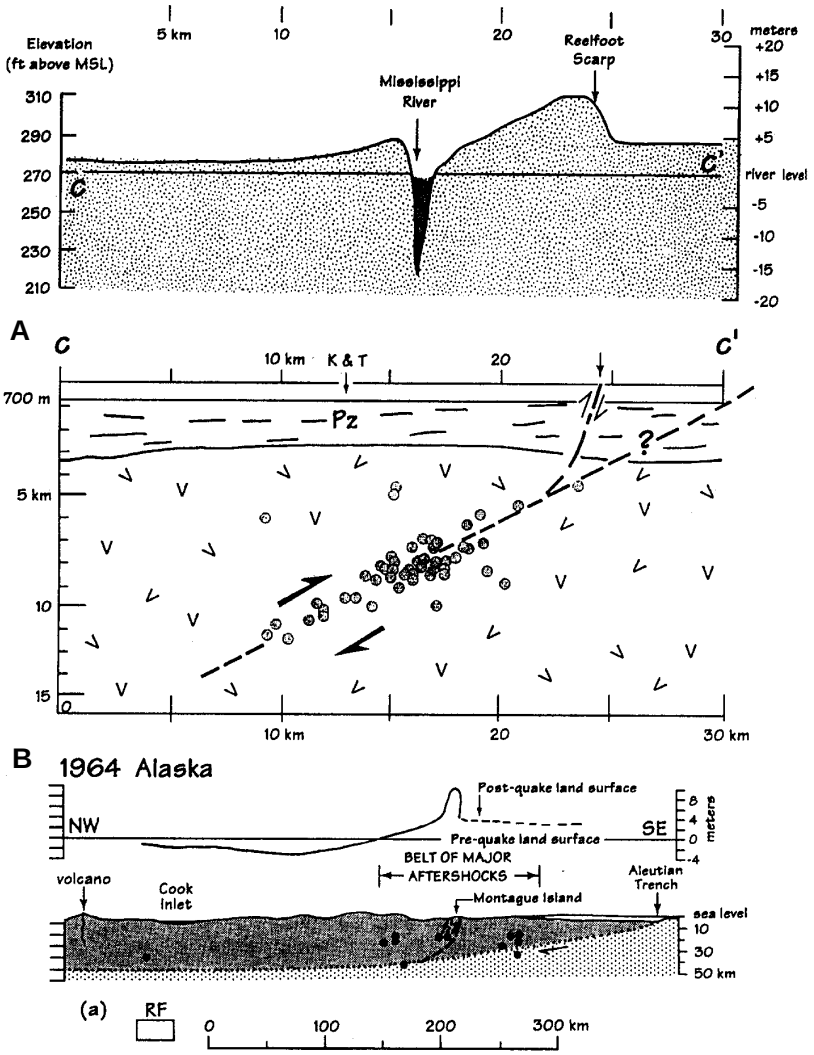

Fig. 1.9. (a) Topography of Reelfoot scarp from locations C to C' (Figure 1.8). The elevation profile is shown relative to the inferred master thrust fault for event F1, but this crustal profile has no vertical exaggeration. There are no data that show Reelfoot fault through the P_z section; also no hypocenters are located there. (b) A similar geometry and relationship between elevation change and a shallow-dipping thrust rupture plane for the 1964 M 9.2 Alaska earthquake. The box RF shows the size of the Reelfoot fault profile in (a) at this scale. (Johnston and Schweig, 1996).

5) The New Madrid North Fault (NN)

The New Madrid north fault (Figure 1.7) was identified in seismic-reflection profiles (Zoback *et al*, 1980; Hamilton and Zoback, 1982). A 35-m offset of the Late Cretaceous reflection coincides with the seismicity trend and passes west of New Madrid, Missouri (Hamilton and Zoback, 1982, Andrews *et al*., 1985). It parallels but is slightly offset from the north-northeast NMSZ seismicity segment that extends nearly to Illinois. It (~30 km length) has a Paleocene age for most of the dip-slip component. The event of 23 January, 1812 might occur on it (Johnston and Schweig, 1996).

6) The Bootheel linement (BL)

The detailed surface trace of the northern Bootheel linement forms a series of profiles across the lineament suggest that the fissures are the surface traces of a subsurface fault system. But the BL is not a new fault, formed in 1811, and does not exhibit nearly the level of current seismicity observed on other discussed fault segment such as the Blytheville arch, the Blytheville fault zone, the Reelfoot fault, and the New Madrid north fault (Johnston and Schweig, 1996).

1.3 The Mississippi Valley Embayment seismicity

The earliest systematical seismological study was performed by Nuttli and his colleagues at Saint Louis University. They made a great contribution to understanding the earthquakes of 1811-1812, the

recent-day seismicity, earthquake hazard and seismotectonics of the NMSZ.

1.3.1 The New Madrid earthquakes of 1811-1812

Between 1811 and 1812, three catastrophic earthquakes, with magnitude estimates greater than 8.0, occurred during a 3-month period. Hundreds of aftershocks followed over a period of several years. The largest earthquakes that have occurred since then were on January 4, 1843 and October 31, 1895 with magnitude estimates of 6.0 and 6.2, respectively. In addition to these events, seven events of magnitudes ≥5.0 have occurred in the area. At that time, St.Louis and other major cities in the central U.S. were sparsely settled (Mitchell *et al.*, 1991).

Information on the timing, location and size of the New Madrid earthquakes of 1811-1812 can be found in Table 1 of Johnston and Schweig (1996).

Nuttli (1973a) constructed a generalized isoseismal map of the first of three principal shocks of the sequence, that of December 16, 1811 by using contemporary accounts of the 1811-1812 Mississippi Valley earthquake sequence. This map is a major base for determining the size of the sequence of the 1811-1812. The map is characterized by an unusually large felt area, with MM intensities of V as far away as the southeast Atlantic coastal area. The anomalously large areas of damage of the principal shocks resulted from both the surficial

geological condition of the Mississippi Valley and the relatively low attenuation of surface-wave energy in eastern North America (Nuttli, 1973b, Mitchell, 1973). Johnston (1996) developed a set of regressions of instrumental M_0 on isoseismal area (felt through VIII) determined for continental region earthquakes. According to these basic relations, he made correlations for North America's extremely low anelastic attenuation to the northeast of New Madrid and for the considerably higher attenuation to the west. The moment magnitudes of earthquakes of 1811 - 1812 were estimated (Table 1, Johnston and Schweig, 1996).

According to eyewitnesses, the locations of the 3 major earthquakes of 1811-1812 were determined by Nuttli (1973a). Johnston and Schweig (1996) synthesized the accounts of eyewitnesses and studied the relationship between the major seismic structures and timing, setting and size of major events of 1811-1812. They inferred models of process of 1811-1812 earthquakes sequence, called the Possible Fault Rupture Scenarios. They suggested that the earthquakes of December 16, 1811 and February. 7, 1812 occurred in Blytheville Arch and the Reelfoot fault, respectively. The event of January 23, 1812 occurred either in the New Madrid west seismic trend or New Madrid north fault (NN).

Evidences of waterfalls or rapids were found for Feb. 7, 1812 event. Johnston and Schweig (1996) believe that only this event involved thrust faulting that resulted in static offset and disruption of the riverbed. Their result is consistent with the seismic observations

of this study.

1.3.2 Paleoseismology, neotectonics and recurrence intervals for large earthquakes

Was the New Madrid earthquake sequence of 1811-1812 a one-time event or have large earthquakes occurred repeatedly in the NMSZ in the recent geological past? The data from local deformation, liquefaction and dendrochronology were used to study the paleoseismological recurrence intervals. The studies provide the evidence that the 1811-1812 earthquakes were not the first in the Holocene. Johnston (1996) summarized the results of paleoearthquake investigations in the NMSZ. The data are consistent with as few as two and as many as four earthquakes in the 2000 years prior to 1811. Schweig and Ellis (1994) investigated the data of liquefaction and estimated that a M ~ 8 earthquake was possible for causing liquefaction separated by about 100 km from northern and eastern New Madrid to the southern Blytheville sites in AD 900. It may have been a multiple event scenario similar to the 1811-1812 sequence.

Johnston and Nava (1985) extrapolated the historical and instrumental record and determined that if a periodic seismic cycle is valid for the NMSZ, earthquakes of 1811-1812 magnitude should recure there every 550-1100 years on average. The probability for an earthquake of magnitude 6.0 or greater is significant in the near future, with a 50% chance by the year 2000 and a 90% chance by the year

2040. This repeat time was frequently used in probabilistic seismic hazard analyses.

A high rate strain rates was found by Liu *et al*. (1992), who reoccupied a 1950s triangulation network in the southern New Madrid Seismic Zone using the Global Positioning System. Their data indicate rapid crustal shear strain accumulation , which results in 5-7 mm/year of right-lateral slip across the width of the network. At this rate of deformation, sufficient strain energy to produce an 1811-1812 type event could accumulate in 400-1100 years (Schweig and Ellis, 1994).

1.3.3 Present day seismicity

Present day seismicity in the Mississippi Embayment has been monitored and located through the installation of the St. Louis University network in 1974 and the Memphis State University network in 1980. The results from earthquake locations for the New Madrid area show four major segments (Stauder *et al*., 1976; Mitchell *et al*, 1991) within the Reelfoot Rift. Herrmann and Canas (1978) defined the faulting nature of the major segments (Figure 1.2b). The longest seismic zone extends for approximately 100 km from near Marked Tree, Arkansas, northeastward to Caruthersville, Missouri and lies along the axis of the Reelfoot rift. Herrmann and Canas (1978) proposed that this is a right-lateral strike-slip fault striking NE. This result is supported by the remeasurement of a triangulation network in the southern part of the NMSZ as mentioned above (Liu *et al*., 1992). The

second zone extends northeastward to Charleston, Missouri and also shows a right-lateral strike-slip movement. A third linear seismic zone between the two northeast trending right-lateral strike-slip faults is a left-step area and extends north-northwest from Dyersburg, Tennessee to near New Madrid, Missouri, it is called "the central New Madrid Seismic Zone". The nature of this fault movement is not clear. This zone is a major focus of the dissertation. A fourth zone is a west-northwest extension from New Madrid. Herrmann (1978, 1979) suggested this is a major left-lateral strike-slip fault zone. This zone is currently more active than the inferred northernmost northeast striking right-lateral fault.

1.3.4 Seismicity surveys

Several seismic surveys have been undertaken to study the seismicity of the central NMSZ in detail. The U.S. Geological Survey operated a dense network of twenty short-period seismic stations in the New Madrid seismicity region from March 20 to May 7, 1978. They found that the most of the epicenters lie to the west of Reelfoot Lake in an 8-km wide, north-northwest trending strip extending from Ridgely, Tenn., to New Madrid, MO, with focal depths ranging from 3-18 km. Composite focal mechanisms are varied, with the compressional axis shifting from east-west near Ridgely to northeast-southwest near New Madrid. O'Connell *et al*. (1982) suggested that the northeasterly compression may result from the left-stepping offset of the northeast-

striking, right-lateral fault system near New Madrid.

Nicholson *et al*. (1984) operated a dense network of portable vertical-component seismographs in the Ridgely area of western Tennessee in May of 1978. During 32 days of operation, 122 earthquakes were detected, of which 90 were located. The data were analyzed for the arrival times of P-waves, and subsequently inverted for velocity structure, hypocenter locations and focal mechanisms. The earthquakes near Ridgely occur on a northwest striking reverse fault that dips to the southwest.

Andrews *et al*.(1985) used a small array of three component digital instruments in the northern Mississippi Embayment. They successfully identified an S-P conversion phase, which is produced because of the low velocity of the unconsolidated sediments. Upgoing waves reach the free surface at near-vertical incidence, resulting in nearly vertical P-wave polarizations and nearly horizontal S-wave polarizations. This S-P converted phase is a strong phase on vertical seismograms.

From mid-October 1989 to August 1992, forty three-component PANDA (Chiu *et al*. 1991) stations were deployed by CERI in the central NMSZ (Chiu *et al*., 1992). This data set is a significant improvement over regional seismic network data and previous surveys because of three component, high and low gain recoding. The PANDA database has permitted a series of studies. The three-dimensional configuration of the sedimentary basin in the Mississippi embayment was determined using S-to-P conversion waves to estimate the thickness of the

sedimentary layer beneath each PANDA station (Chen *et al*. 1993). Chiu *et al*. (1992) proposed two active faults in the central NMSZ and inferred the relationship between the active faults and the Lake County Uplift, but they did not determine the nature of the active faulting. A series of 'en-echelon' faults near the Ridgely area were found by using master event relocation and the focal mechanisms obtained in this study (Xie *et al*., 1996). The attenuation structure of body waves in the shallow sediment of the NMSZ was defined by Liu *et al*. (1994). In the present study, we analyze the high-quality, three-component digital data set to study the focal mechanisms of the microearthquakes by using waveform modeling techniques in an attempt to better understand the seismotectonics of the NMSZ.

1.3.5 The velocity and attenuation model

The earliest velocity model for this region (CMVEB, 1974-1991) was obtained by Nuttli *et al*., (1969), and consists of a simple layered crust. All velocities increase with depth and V_p/V_s =1.71. Herrmann (1979) used the central U.S. velocity model given in Herrmann (1978) to estimate source parameters from the surface waves. Mooney *et al*. (1983) and Ginzburg *et al*. (1983) determined compressional wave velocity model of the northern Mississippi embayment from an extensive set of seismic refraction profiles. They suggested three separated models: rift, eastern flank of the rift and the western flank of the rift. The rift low velocity model was supported by the other refraction

experiment (Liao and McMeChan, 1996).

Two N-S and E-W oriented lines crossed the Blytheville Arch and adjacent portions of the Reelfoot Rift. The main features in the data can be explained by the existence of a strong 15-km-wide low-velocity cap lying beneath the center of the Blytheville Arch between 1.5 and 2.5 km depth; it is at least 30 km long and appears to become less prominent toward the southwest. The arch itself has a low-velocity background that extends to at least 5 km depth. An additional low-velocity layer lies generally between 3 and 4 km deep, which is upwarped at the Reelfoot Rift (Liao and McMeChan, 1996).

Al-Shukri and Mitchell (1988) applied a three dimension inverted P-travel times for a three dimension model, and found a clear relationship between reduced seismic velocities and the source zone of New Madrid earthquake.

Chiu *et al*. (1992) employed a crustal velocity inversion for independent P- and S-wave velocity inversion of travel times from 455 PANDA hypocentral solutions. The Andrews *et al*. (1985) model served as the starting model for inversion. Initially, inversion convergence was hindered by extreme velocity contrasts between the soft, low-velocity rocks and basement rocks. However, constraints from extensive well log data for the embayment, secondary phases (SP and PS), and abundant, high-quality shear-wave data yielded a relatively robust inversion. The main characteristics of Chiu's model are smaller ratios of Vp/Vs than those in Andrew's (Vp/Vs = 3.00, 1.69, 1.51 for first, second and third layer in Chiu's model compared to Vp/Vs = 3.21,

1.74, 1.75 in Andrews's model). Chiu's model was used in our study with variable thickness of sediment at each station.

A number of attenuation studies have been performed in the central and eastern United States. Nuttli (1973b, 1978), Mitchell (1980 and 1981) and Singh and Herrmann (1983) found that the attenuation of Lg and Lg coda is very low in Eastern North America. Mitchell (1973, 1975, 1980, 1981) observed, using fundamental model surface waves, that the difference between the high attenuation observed in the western United states and that observed in the eastern United States is due to differences in anelastic properties of the upper crust. Al-Shukri and Mitchell (1990) applied the decay method (Anderson and Hough, 1984; Hough *et al*., 1988) to study the attenuation of P-waves in the NMSZ. They found that regions with low Q_p values coincide with regions of low seismic velocity delineated by Al-Shukri and Mitchell (1988). Hamilton and Mooney (1990) reported that the strongest attenuation of seismic waves occurs when the refraction profiles pass through the northeast trend of seismicity in the southern NMSZ. Liao and McMechan (1996) suggested that there is no evidence for anomalously low intrinsic Q in Blytheville Arch area, only local scattering is observed. Chen *et al*. (1993) studied the Q_p - Q_s relations in the sedimentary basin in the upper Mississippi Embayment using S-to-P conversion waves.

The attenuation characteristics of body waves in sediments in the NMSZ was studied by Liu *et al*. (1994). Data from the PANDA deployment in the central part of the NMSZ have been used to study the

attenuation of body waves. The spectral decay technique is used to analyze acceleration spectra of both P- and S-waves in a frequency range of 5-25 Hz in order to obtain the high frequency attenuation parameter κ. A multiple, weighted least squares method is applied to obtain the site attenuation factor of κ_0 at each station and to get $d\kappa/dr$, which were interpreted in terms of a two-layer Q structure consisting of a sedimentary layer overlying the upper crust. Q_S (36) and Q_P (56) are found for the sediment layer. The S-wave κ_0 obtained are stable and show a positive correlation with sediment thickness. The κ_0 values for P waves in the sediments show significant scatter, which may be due to greater sensitivity of P-wave attenuation to water content of the soils than that of S waves.

Consistency checks on the assumptions made in obtaining the κ_p and κ_s values were made by studying the source spectrum of several events and the differential κ from the spectral ratio of the converted Sp to S phases. The data set was found to be internally consistent, but the results are limited to deep sediment sites, since the vertical distribution of Q is not known (Liu *et al.*,1994).

1.3.6 Focal mechanisms and stress field

The near east-west regional stress field was determined by Zoback and Zoback (1991), possibly due to lithospheric drag related to plate interactions (Zoback and Zoback, 1991) or ridge push force (Zoback and Zoback, 1989). Russ (1982) identified the Lake County Uplift which is

indicative of northeast-southwest compression. It appears that motion on the two right-lateral strike-slip faults generates a localized change in the orientation of the stress field along the left stepping offset, as suggested by O'Connell *et al*. (1982) and Russ (1982). Recently, Herrmann and Ammon (1997) illustrate a combined modeling approach using observations from three earthquakes that occurred within the environs of the New Madrid Seismic Zone and also reexamine the faulting geometry for two events from the 1960's. They found that tension-axes are generally aligned in a N-S to NW-SE direction, while the compression-axes trend in a NE to E direction in the NMSZ area. Similar results are found by Liu and Herrmann (1996) and Liu *et al*. (1996).

Herrmann and Canas (1978) and Herrmann (1979) studied the focal mechanisms of the NMSZ. They used surface-wave inversions together with data from the Saint Louis University regional network data, to demonstrate predominant right-lateral strike-slip on both northeast trending segments and left-lateral strike-slip on the west-northwest trending segment. This is a basic conclusion for defining the faulting nature of the NMSZ. This result was supported by other focal mechanism studies (Nicholson *et al*. 1984; Andrews *et al*. 1985; Young *et al*. 1995). Previous results of focal mechanisms of the central segment are complex, with a wide range of fault-plane solutions.

The focal mechanism study around the southern junction (Ridgely) and southern portion of the central NMSZ have indicated reverse motion on some southwest dipping planes (Herrmann and

Canas, 1978; Herrmann, 1979; Nicholson *et al*., 1984; Andrews *et al*., 1985, Yang *et al*., 1995). In the northern portion of the central NMSZ between Ridgely and New Madrid, these authors found some very complex focal mechanism patterns. Himes and Herrmann (1981) demonstrate that the earthquakes located near the northern junction occur on a well-defined dipping plane oriented north-west and dipping 40° to the southwest. This agrees quite well with Nicholson's (1984) composite focal mechanisms in this area, showing left-lateral motion on a northwest plane dipping to the southwest. Andrews *et al*. (1985) suggested that the choice of fault plane is equivocal because of the intersection of two or three seismicity trends. They defined a right-lateral strike-slip motion on northeast striking fault. O'Connell *et al*. (1982) observed that the composite focal mechanisms are varied, with the compressional axis shifting from east-west near Ridgely to northeast-southwest near New Madrid. Yang *et al*. (1995) indicated that normal faulting is the dominant focal mechanism in the northern portion of the central NMSZ. They used the PANDA data and individual event P-wave first motion. All of these focal mechanism studies in the central NMSZ used only the P-wave first motions for the individual or composite events. The currently conflicting solutions do not show a simple relationship with respect to the regional stress field.

1.3 Summary

The basic conclusions of the geophysical and seismological observation suggested: 1) the governing tectonic structure of the NMSZ area is an ancient continental rift. All large (M>7) intraplate earthquakes throughout the world occur in such Paleo-extensional tectonics. 2) Historical earthquakes and present day seismicity shows that the New Madrid Seismic Zone is the most seismically active area of the central and eastern United States. Paleoseismology studies for pre 1811-1812 earthquakes confirm that the 1811-1812 earthquakes were not a one-time only event. The possibility of recurrence of such large earthquakes and the greatly increased population of the area provided an impetus for geological investigation. However, the NMSZ is covered by a thick sediment layer. Direct observation of fault behavior is not possible. Therefore, a microearthquake faulting geometry and style can provide direct information on regional seismotectonics. 3) Current seismicity delineates four major fault segments. The geometry and nature of the active faulting of the central NMSZ as well as the relationship to geologic features is not well understood. Previous focal mechanism studies obtained conflicting results using limited information in the central NMSZ. Recently, the high-quality 3-component PANDA data were made available. Good velocity (Chiu *et al*. 1993) and attenuation models (Liu *et al.*, 1994) have been determined. We have had successful experience of application of the waveform modeling techniques (Liu *et al*. 1991) to infer source parameters. Therefore,

this study is necessary and feasible.

In the following chapters, the theory and applications of the waveform modeling techniques will be discussed in detail.

CHAPTER 2

SYNTHETIC SEISMOGRAMS

2.1 Introduction

In this chapter I review several techniques for calculating ground motion. The first of the theoretical methods is the Cagniard de-Hoop technique used for a medium composed of homogeneous plane layers (Helmberger, 1968; Helmberger and Harkrider, 1978; Helmberger, 1983). The key here is a numerical approach for obtaining the Cagniard path in the complex ray-parameter plane. The second theoretical approach uses the matrix propagator methods introduced in seismology by Haskell (1964). This method requires evaluating doubly transformed solutions as a function of (k, z, ω), where k is the wavenumber, z is the depth, and ω is the angular frequency. An integral over real k is performed for each frequency and followed by an inverse Fourier transform over frequency to obtain a "synthetic" seismogram (Wang and Herrmann, 1980; Herrmann and Wang, 1985).

These two seismogram computation methods are based on two important assumptions. 1) For a medium in which ρ, α and β depend only on depth (z), it is therefore permissible to model a continuous

profile with a large number of homogeneous plane layers; 2) since a full consideration of the Earth's spherical geometry is quite involved at high frequency, a cylindrical system with vertical axis of symmetry is used.

In this study the Cagniard de-Hoop technique is initially used for local velocity model and preliminary focal mechanisms, and the waveform number integration is used for final synthetics.

2.2 Cagniard de-Hoop technique

Generalized ray theory (Cagniard de-Hoop technique) is a mathematical simplification of Lamb's (1904) problem, proposed by de-Hoop (1960) and Cagniard (1962). We assume that earthquakes can be simulated by distributed shear dislocations and that the Earth can be replaced by a layered elastic medium. The layered structure complication is effectively removed by a generalized ray expansion of the P-, SV, and SH displacement potentials and the Cagniard de-Hoop technique used to obtained the transient response. As a first step we will consider a shear dislocation in a whole space expressed in cylindrical coordinates because of its compatibility with the layered problem (Helmberger and Harkrider, 1978; Saikia and Herrmann, 1985, 1986, 1987).

2.2.1 Response of shear dislocation sources in a homogeneous half-space

Maruyama (1964) and Haskell (1964) introduced that a shear fault where a discontinuity in displacement across a fault plane was allowed, resulting in a double-couple radiation pattern. Harkrider (1976) obtained convenient forms of displacements and displacement potentials for a number of different coordinate systems. The solution in cylindrical coordinates, suitable for application of Cagniard's method is given by Helmberger and Harkrider (1978) and Langston and Helmberger (1975). In the Cagniard de-Hoop approach the double integral over k (wavenumber) and ω (angular frequency) is transformed to a double integral over p (ray parameter) and s (Laplace transform variable) by using a change of variable, defined as

$$k = -jsp$$

$$\eta_v = (\frac{1}{v^2} - p^2)^{\frac{1}{2}}$$

and using recurrence relations for the Bessel's and modified Bessel's functions (j is $(-1)^{1/2}$. The Laplace transformed displacements in the vertical, tangential, and radial directions are (Helmberger and Harkrider, 1978):

$$\bar{W} = \frac{\partial \bar{\phi}}{\partial z} + sp\bar{\omega} \tag{2.2.1}$$

$$\bar{V} = \frac{1}{r}\frac{\partial \bar{\phi}}{\partial \theta} - \frac{1}{spr}\frac{\partial^2 \bar{\omega}}{\partial z \partial \theta} - \frac{\partial \bar{\chi}}{\partial r}$$

$$\bar{Q} = \frac{\partial \bar{\phi}}{\partial r} - \frac{1}{sp}\frac{\partial^2 \bar{\omega}}{\partial r \partial z} + \frac{1}{r}\frac{\partial \bar{\chi}}{\partial \theta}$$

where z, r, and θ are the vertical, radial and polar angle coordinates, respectively. The P-wave potential ($\bar{\phi}$), the SV-wave potential ($\bar{\omega}$), and the SH-wave potential ($\bar{\chi}$) at an observation point (r, θ,z) are expressed by: P-waves (2.2.2):

$$\bar{\phi} = \frac{M_0}{4\pi\rho}\frac{2}{\pi}\,\mathrm{Im}\int_c^{+i\infty+c} C_1(p)\frac{p}{\eta_\alpha}\,exp(-s\eta_\alpha\,|\,z-h\,|\,)K_2(spr)dp.\,A_1(\theta,\lambda,\delta)$$

$$+\frac{M_0}{4\pi\rho}\frac{2}{\pi}\,\mathrm{Im}\int_c^{+i\infty+c} C_2(p)\frac{p}{\eta_\alpha}\,exp(-s\eta_\alpha\,|\,z-h\,|\,)K_1(spr)dp.\,A_2(\theta,\lambda,\delta)$$

$$+\frac{M_0}{4\pi\rho}\frac{2}{\pi}\,\mathrm{Im}\int_c^{+i\infty+c} C_3(p)\frac{p}{\eta_\alpha}\,exp(-s\eta_\alpha\,|\,z-h\,|\,)K_0(spr)dp.\,A_3(\theta,\lambda,\delta)$$

SV-waves (2.2.3):

$$\bar{\omega} = \frac{M_0}{4\pi\rho}\frac{2}{\pi}\,\mathrm{Im}\int_c^{+i\infty+c} SV_1(p)\frac{p}{\eta_\beta}\,exp(-s\eta_\beta\,|\,z-h\,|\,)K_2(spr)dp.\,A_1(\theta,\lambda,\delta)$$

$$+\frac{M_0}{4\pi\rho}\frac{2}{\pi}\,\mathrm{Im}\int_c^{+i\infty+c} SV_2(p)\frac{p}{\eta_\beta}\,exp(-s\eta_\beta\,|\,z-h\,|\,)K_1(spr)dp.\,A_2(\theta,\lambda,\delta)$$

$$+\frac{M_0}{4\pi\rho}\frac{2}{\pi}\,\mathrm{Im}\int_c^{+i\infty+c} SV_3(p)\frac{p}{\eta_\beta}\,exp(-s\eta_\beta\,|\,z-h\,|\,)K_0(spr)dp.\,A_3(\theta,\lambda,\delta)$$

SH-waves (2.2.4):

$$\bar{\chi} = \frac{M_0}{4\pi\rho}\frac{2}{\pi}\,\mathrm{Im}\int_c^{+i\infty+c} SH_1(p)\frac{p}{\eta_\beta}\,exp(-s\eta_\beta\,|\,z-h\,|\,)K_2(spr)dp.\,A_4(\theta,\lambda,\delta)$$

$$+\frac{M_0}{4\pi\rho}\frac{2}{\pi}\,\mathrm{Im}\int_{c}^{+i\infty+c} SH_2(p)\frac{p}{\eta_\beta}\,exp(-s\eta_\beta\,|\,z-h\,|\,)K_1(spr)dp.\,A_5(\theta,\lambda,\delta)$$

The more important parameters are as follows:

s = Laplace transform variable

p = ray parameter

$\eta_v = (\frac{1}{v^2} - p^2)^{\frac{1}{2}}$

h = depth of source

α= compressional velocity

β = shear velocity

ρ= density

M_0 = seismic moment

K_n = modified Bessel's function of order n and second kind.

with the orientation constants given (Helmberger and Harkrider, 1978) by:

$$A_1(\theta,\lambda,\delta) = \sin 2\theta\cos\lambda\sin\delta + \tfrac{1}{2}\cos 2\theta\sin\lambda\sin 2\delta \qquad (2.2.5)$$

$$A_2(\theta, \lambda, \delta) = \cos\theta \cos\lambda \cos\delta - \sin\theta \sin\lambda \cos 2\delta$$

$$A_3(\theta, \lambda, \delta) = \tfrac{1}{2} \sin\lambda \sin 2\delta$$

$$A_4(\theta, \lambda, \delta) = \cos 2\theta \cos\lambda \sin\delta - \tfrac{1}{2} \sin 2\theta \sin\lambda \sin 2\delta$$

$$A_5(\theta, \lambda, \delta) = -sin\theta \cos\lambda \cos\delta - \cos\theta \sin\lambda \cos 2\delta$$

where

θ = strike from the end of the fault plane with respect to the observation point.

λ = rake angle

δ = dip angle

The vertical radiation patterns, as will become apparent shortly, are defined by

$$C_1 = -p^2$$

$$C_2 = 2\xi p \eta_\alpha$$

$$C_3 = p^2 - 2{\eta_\alpha}^2$$

$$SV_1 = -\xi p \eta_\beta$$

$$SH_1 = \frac{1}{\beta^2}$$

$$SV_2 = \eta_\beta{}^2 - p^2$$

$$SH_2 = -\frac{\xi}{\beta^2}\frac{\eta_\beta}{p}$$

$$SV_3 = 3\xi p \eta_\beta$$

where

$$\xi = \begin{cases} +1 & \text{if} \quad z > h \\ -1 & \text{if} \quad z < h \end{cases}$$

From (2.2.2) to (2.2.5) we can now immediately identify the expressions for the potential due to pure vertical strike-slip, pure vertical dip-slip, and 45^o dipping dip-slip at 45^o azimuth types of sources. If the relations of (2.2.3) are carefully examined, we can also notice that A_2, A_3, and A_5 are all zero for the vertical strike-slip case (δ = 90^0, λ = 0^o) and so the first terms in (2.2.2), (2.2.3) and (2.2.4) correspond to P-, SV-, and SH-wave potentials, respectively for this source. Similarly, for the vertical dip-slip (δ = 90^o, λ = 90^o) orientation A_1, A_3, and A_4 are zero and so the second terms in these expressions correspond to P-, SV-, and SH- wave potentials, respectively, for this orientation. There exists another term in $\bar{\phi}$ and $\bar{\psi}$. For the case δ= 45^o, λ = 90^o, and θ = 45^o, only A_3 of (2.2.5) is non-zero. This fault orientation is known as 45^o dip-slip at azimuth 45^o from the end of the fault. Hence for SH waves there will be a contributions from vertical strike-slip and vertical dip-slip source types and for P and SV waves there will be contributions from all three types of sources. These are known as three fundamental shear dislocations. Any displacement field

induced by an arbitrary shear dislocation can be expressed in terms of the displacement fields induced by these three fundamental shear dislocations.

In the integrals (2.2.2) to (2.2.4), the modified Bessel's function K_n approach infinite values as p approaches zero. Therefore, p = 0 is a singularity of K_n. To evaluate the integrals at p = 0 one must use the residue theorem of complex variables. At other points, the integrals must be evaluated as $\int_c^{j=i\infty+c}$ rather than as $\int_0^{j=i\infty}$. However, this residue contribution is important only in evaluating the time-domain potential, but not in the time domain displacements (Harkrider, 1976). Because, even if the standard integral forms of the cylindrical shear potential for point quadrupole seismic sources in the frequency domain k-integral and Cagniard de-Hoop path p-integral are not the Fourier transform pair, they both yield the same displacement field (Helmberger and Harkrider, 1978). Therefore, while evaluating the displacement fields $\bar{W}$, $\bar{Q}$ and $\bar{V}$ from these integrals are not considered in the residue contribution. Evaluation of the integrals of (2.2.2) to (2.2.4) is equivalent to evaluating the field function defined (Harkrider and Helmberger, 1978) by

$$\bar{\zeta}_n(r,z,s) = \frac{2}{\pi} s \,\mathrm{Im} \int_c^{i\infty+c} \frac{p}{\eta_v} k_n(spr) e^{-s\eta_v \mid z-h \mid} dp \qquad (2.2.6a)$$

for each generalized ray. This integral can be evaluated either by using the exact values for k_n(spr) or by making the approximation that

for large arguments $k_n(\text{spr})$ may be expressed as

$$k_n(spr) = (\frac{\pi}{2spr})^{1/2} e^{-spr}[1 + \mu - \frac{1}{8spr} + \ldots .]$$

where $\mu = 4n^2$. We will first evaluate the exact solution and then approximate solution.

From (2.2.6a) the exact solution in time domain has the following form

$$\zeta_n(r,z,t) = \frac{2}{\pi}\frac{\partial}{\partial t}\,\mathrm{Im}\int_0^t \frac{c_n(t,\tau)}{(t-\tau)^{\frac{1}{2}}(t-\tau+2pr)^{\frac{1}{2}}}\frac{dp}{d\tau}\frac{p(\tau)}{\eta_v}\,d\tau \qquad (2.2.6b)$$

where (Helmberger and Harkrider. 1978)

$$c_n(t,\tau(p)) = \cosh[n\cosh^{-1}(\frac{t-\tau+pr}{pr})]$$

For the exact solution (2.2.6b) obtained from (2.2.6a) we must change the path of integration along the positive imaginary p-axis to the Cagniard contour C. The geometry is given in Figure (2.1) and the de-Hoop contour C defined by choosing those values of p which make τ (p) real and increasing, where

$$\tau(p) = pr + \eta_v\,|z-h| \qquad (2.2.7)$$

We obtain

$$p(\tau) = \frac{r}{R^2} + i(\tau^2 - \frac{R^2}{v^2})^{\frac{1}{2}}\,|z-h| \qquad (2.2.8)$$

$$\eta(\tau) = \frac{|z-h|\,\tau}{R^2} - i(\tau^2 - \frac{R^2}{v^2})^{\frac{1}{2}}\frac{r}{R^2} \qquad (2.2.9)$$

and

$$\frac{dp(\tau)}{d\tau} = i\,\frac{\eta_v(\tau)}{(\tau^2 - \frac{R^2}{v^2})^{\frac{1}{2}}} \tag{2.2.10}$$

where

$$R^2 = r^2 + |\,z - h\,|^2$$

Note that the integrand (2.2.6b) is real until

$$p = p_0 = \frac{r}{Rv} = \frac{\sin i}{v}$$

which is the ray parameter corresponding to Snell's law. We also notice that for τ(p) is always real and so from (2.2.8) and (2.2.9) it is very clear that at $p = p_0$ in the p-plane the Cagniard contour leaves the real p-axis to the complex p-plane and remained complex infinity as shown in Figure (2.1). There is no contribution to ζ_n(r,z,t) (2.2.6b) along the part of the contour between τ = 0 and τ = R / v, since p and the integrand are real. Further, there is no contribution to the integral when evaluated along the arc C_1 in the first quadrant as

$$\int_{C_1} \frac{e^{-s}(pr + \eta_v\,|\,z\,|)}{\eta_v}\,dp \to 0$$

Note that there is no singularity between C and the positive imaginary p- axis. Since $\frac{\partial f(t)}{\partial t}$ <=> sF(s)-F(0), we can do an inverse Laplace transform and ζ_n (2.2.6) can be identified.

In this simple case we have a closed form solution for various values of η since the equivalent form back in the (ω,k) domain has been

evaluated by Harkrider (1976). For example,

$$\zeta_2(r,z,t) = \frac{d}{dt}\left[\frac{1}{R} + \frac{2v}{r^2}(t-\frac{R}{v})H(t-\frac{R}{v})\right] \tag{2.2.11}$$

where the near-field contribution appears in terms of r. Another approach, where relatively fast evaluation of (2.2.6b) is carried out, is to determine the rate of change of the integrand by a non-uniform quadrature technique (Helmberger and Harkrider, 1978). Equation (2.2.6b) can be evaluated for various values of (t) after a change of variable as proposed by Helmberger (1978). They expanded the integrand of (2.2.6) in terms of $t - r^{1/2}$ and worked out the following approximation correct to the first order

$$\frac{c_n(t,\tau,p)}{t-\tau+2pr^{1/2}} = \frac{1}{2pr^{1/2}}$$

Thus, we can approximate (2.2.6) by

$$\zeta_n(v,z,t) = \frac{2}{\pi}\frac{\partial}{\partial t}\,\mathrm{Im}\int_0^t \frac{1}{(2pr)^{1/2}}\,\frac{1}{(t-\tau)^{1/2}}\,\frac{dp}{dt}\,\frac{p}{\eta_v}\,d\tau \tag{2.2.12}$$

$$= \frac{d}{dt}\left[\frac{1}{t^{1/2}} * \mathrm{Im}\left(\left(\frac{2}{r}\right)^{1/2}\frac{1}{\pi}\,\frac{p^{1/2}}{\eta_v}\,\frac{dp}{dt}\right)\right]$$

We have used the approximation t << 2pr which is a high frequency approximation. A further approximation can be used at very large range: since

$$\frac{dp}{dt} = \frac{i(t-t_R)^{-\frac{1}{2}}\eta_v}{(2t_R)^{1/2}}$$

where t_R = R / v, and (2.2.12) reduces to

$$\zeta_n(r,z,t) = \frac{\delta(t - t_R)}{R} \tag{2.2.13}$$

called the first-motion approximation. This approximation is valid at teleseismic distances where the ratio of travel time to duration is of the order of 100 or greater, and has proved quite useful in modeling shallow earthquakes recorded teleseismically (Langston and Helmberger, 1975; Helmberger and Harkrider, 1978).

2.2.2 High frequency solution for a multilayer problem

The mathematical formulation above can be used to give the displacements at the free surface of a layered half-space model. Once the Green's functions due to the three fundamental source types are calculated, the final displacement can be easily computed for an arbitrary dislocation (Helmberger and Harkrider 1978, Helmberger, 1983). For a layered half-space model, where the far-field term is retained, the tangential displacement at the surface is given (Helmberger, 1983; Helmberger and Harkrider, 1978)by

$$V(r,0,\theta,t) = \frac{M_0}{4\pi\rho_0}\frac{d}{dt}[\dot{D}(t) * \sum_{j=1}^{2} A_{j+3}(\theta,\lambda,\delta)V_j(t)] \tag{2.2.14}$$

where

$$V_j(t) = (\frac{2}{r})^{1/2}\frac{1}{\pi}\frac{1}{t^{1/2}} * \mathrm{Im}\left[(\sum_{i=1}^{n}\frac{p^{1/2}}{\eta_\beta} SH_j(p)\Pi_i(p)\frac{dp}{dt})_i\right]$$

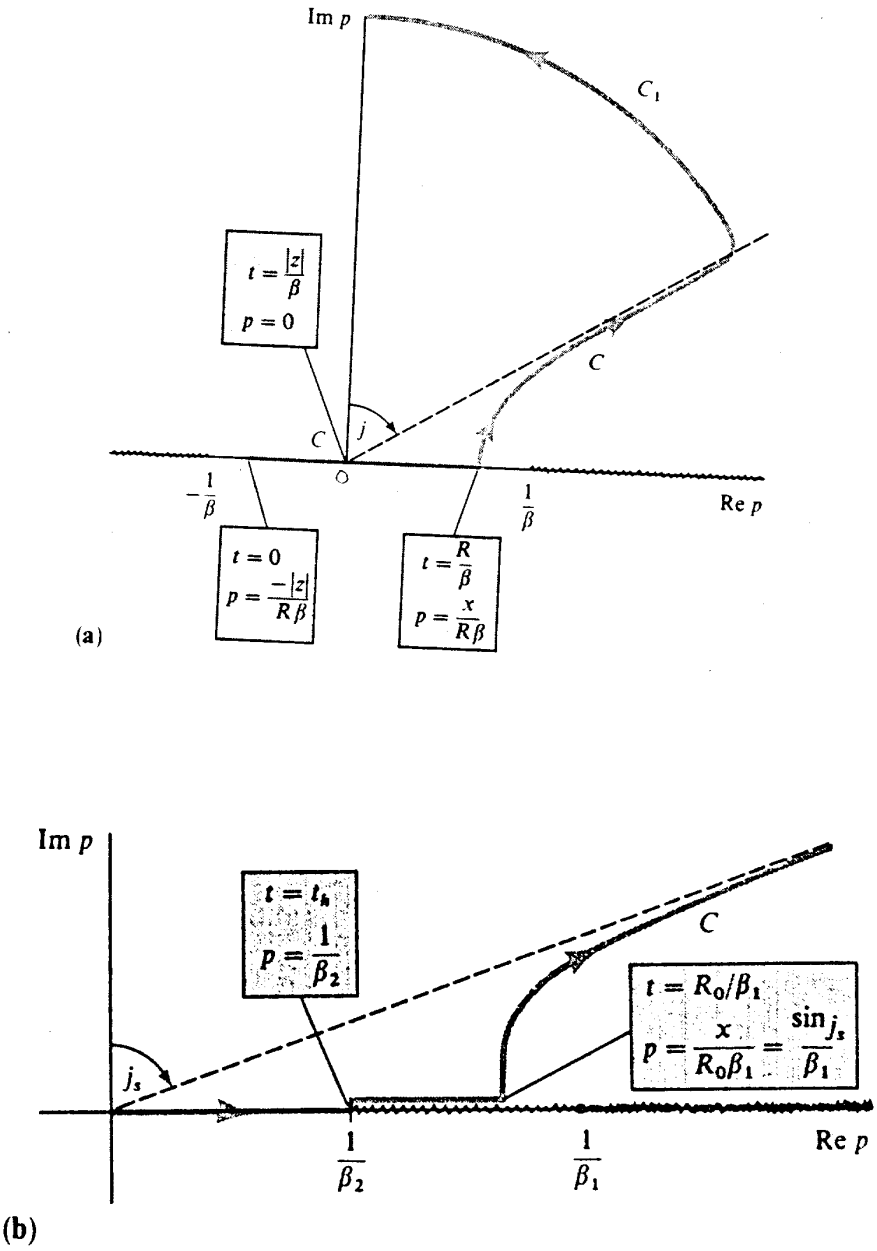

Fig. 2.1. Cagniard de-Hoop contour in the complex p-plane, (a) given by (2.2.8) is shown in the complex p-plane, beginning at t = 0 on the negative real p-axis, turning on to a branch of a hyperbola at t = R/β, and continuing into the first quadrant. (b) for a receiver at post-critical distance (From Aki and Richards, 1980).

$\dot{D}$ (t) = far-field time history

Π_i (p) = product of reflection and transmission coefficients

and the summation is over contributing rays. The high-frequency approximations for the other components of motion are more complicated with the vertical displacement on the free surface given by

$$M(r,0,\theta,t) = \frac{M_0}{4\pi\rho_0}\frac{d}{dt}[\dot{D}(t) * \sum_{j=1}^{3} A_j W_j] \tag{2.2.15}$$

where

$$W_j(t) = (\frac{2}{r})^{1/2}\frac{1}{\pi}\left[\frac{1}{t^{1/2}} * \sum_{i=1}^{n}(\mathrm{Im}\,\frac{p^{1/2}}{\eta_\alpha} C_j(p) R_{NZ}(p)\Pi_i(p)\frac{dp}{dt})_i\right]$$

$$+(\frac{2}{r})^{1/2}\frac{1}{\pi}\left[\frac{1}{t^{1/2}} * \sum_{i=1}^{n}(\mathrm{Im}\,\frac{p^{1/2}}{\eta_\beta} SV_j(p) R_{NZ}(p)\Pi_i(p)\frac{dp}{dt})_i\right]$$

The function Π_i (p) defines the product of all transmission and reflection coefficients along the path from the source to the receiver. The function R_{NZ} (p) is defined as R_{PZ}(p) or R_{SZ} (p), depending on the mode of propagation upon arrival at the receiver, with

$$R_{PZ} \equiv 2\eta_\alpha \frac{(\eta_\beta{}^2 - p^2)}{\beta^2 R(p)}$$

$$R_{SZ} \equiv \frac{4p\eta_\alpha\eta_\beta}{\beta^2 R(p)}$$

$$R(p) \equiv (\eta_\beta{}^2 - p^2)^2 + 4p^2\eta_\alpha\eta_\beta$$

R_{PZ} and R_{SZ} are called receiver functions and are derived by taking the limiting conditions as direct P, reflected PP, and SP converge in time at a free surface, see Knopoff *et al.*, (1957) , Helmberger (1968),

Helmberger and Harkrider (1978).

The radial displacement, Q, is obtained by replacing R_{PZ} and R_{SZ} by R_{PR} and R_{SR} defined by

$$R_{PR} \equiv \frac{-4\eta_\alpha \eta_\beta p}{\beta^2 R(p)}$$

$$R_{SR} \equiv \frac{2\eta_\beta (\eta_\beta{}^2 - p^2)}{\beta^2 R(p)} \tag{2.2.16}$$

In (2.2.15), D(t) is the source time function. If the time derivative from D(t) and differential operator $\frac{d}{dt}$ are brought to the right hand side of the convolution operator '*' in expression (2.2.14), then the response at the receiver is actually an impulse response of the medium (Helmberger and Harkrider, 1978, Saikia and Herrmann, 1985, 1986, 1987).

2.2.3 Full Cagniard solution

The high-frequency solution discussed in the last section has many advantages due to its simplicity. However, for small values of (spr), one must use the full solution by applying the transformations used in deriving expression (2.2.6)

The displacements given by (2.2.1) can be evaluated by substituting the potentials (2.2.2, 2.1.3, 2.1.4) and inverting the various terms back into the time domain by using reverse Laplace transform technique. The vertical displacement becomes

$$W(r,z,\theta,t) = \frac{M_o}{4\pi\rho_o}\frac{d}{dt}\dot{D}(t) * \sum A_j W_j \tag{2.2.17}$$

where W_1, W_2, and W_3 correspond to a pure strike-slip, dip-slip, and 45^o dip-slip, respectively. The strike-slip response can be written

$$W_1(r,z,\theta,t) = \frac{2}{\pi}\,\mathrm{Im}\int^t g_\alpha(2) C_1 R_{PZ}\, d\tau \tag{2.2.18}$$

$$+\frac{2}{\pi}\,\mathrm{Im}\int^t g_\beta(2) S V_1 R_{SZ}\, d\tau$$

where

$$g_v(n) = C_n(t,\tau,p)\frac{p}{\eta_v}\left(\frac{dp}{d\tau}\right)(t-\tau+2pr)^{\frac{-1}{2}}(t-\tau)^{\frac{-1}{2}} \tag{2.2.19}$$

and

$$R_{PZ} = \eta_\alpha \tag{2.2.20}$$

$$R_{SZ} = p$$

for a whole space.

They are given by expression (2.2.16) for a receiver on the free surface. Again, similar expressions are obtained for the dip-slip and 45^o dip-slip cases with n = 1 and n = 0, respectively.

The tangential displacement is slightly more complicated because of the explicit near-field terms

$$V(r,z,\theta,t) = \frac{M_o}{4\pi\rho_o}\frac{d}{dt}\left[\dot{D}(t) * \sum_{j=1}^{2} A_{j+3} V_j\right] \tag{2.2.21}$$

$$V_1(r,z,\theta,t) = \frac{2}{\pi}\,\mathrm{Im}\int^t g_\beta(2) S H_1 R_T\, d\tau \tag{2.2.22}$$

$$+\frac{2}{\pi}\,\mathrm{Im}\int\int^{t} g_{\beta}(2)SH_1R_T(\frac{2}{pr})d\tau dt$$

$$+\frac{2}{\pi}\,\mathrm{Im}\int\int^{t} g_{\alpha}(2)C_1R_{PT}(\frac{2}{r})d\tau dt$$

$$+\frac{2}{\pi}\,\mathrm{Im}\int\int^{t} g_{\beta}(2)SV_1R_{ST}(\frac{2}{r})d\tau dt$$

where

R_T = p, R_{PT} = 1, R_{ST} = - η_β/p, for whole space

and

$$R_T = 2p$$

$$R_{PT} = \frac{4\eta_\alpha\eta_\beta}{\beta^2 R(p)}$$

$$R_{ST} = -2\,\frac{\eta_\beta}{p}\,\frac{(\eta_\beta{}^2 - p^2)}{\beta^2 R(p)}$$

for a receiver on the free surface. The dip-slip expression is similar with n = 1 and where the distance factor in parentheses is reduced by two.

Finally, and most complicated, the radial component is expressed (Helmberger and Harkrider, 1978) by:

$$Q(r,z,\theta,t) = \frac{M_0}{4\pi\rho_o}\,\frac{d}{dt}\,\left[\dot{D}(t) * \sum_{j=1}^{3} A_j Q_j\right] \qquad (2.2.23)$$

where

$$Q_1(r,z,\theta,t) = \frac{2}{\pi}\int^{t} g_\alpha(1)C_1 R_{PR}\,d\tau \qquad (2.2.24)$$

$$+\frac{2}{\pi}\int^{t} g_\beta(1)SV_1 R_{SR}\,d\tau$$

$$+\frac{2}{\pi}\int\int^{t} g_\alpha(2)C_1 R_{PR}\left(\frac{2}{pr}\right)d\tau\,dt$$

$$+\frac{2}{\pi}\int\int^{t} g_\beta(2)SV_1 R_{SR}\left(\frac{2}{pr}\right)d\tau\,dt$$

$$+\frac{2}{\pi}\int\int^{t} g_\beta(2)SH_1\left(\frac{-2}{r}\right)d\tau\,dt$$

and

$$R_{PR} = \text{-P},\ R_{SR} = \eta_\beta$$

for whole space and given by expression (2.2.16) for a receiver on a free surface. Similar expressions for the dip-slip result are obtained by changing the n to 1 and distance factor in parentheses reduced by two.

The 45^o dip-slip result is simply

$$g_3(r,z,\theta,t) = \frac{2}{\pi}\int^{t} g_\alpha(1)C_3 R_{PR}\,dt \qquad (2.2.25)$$

$$= \frac{2}{\pi}\int^{t} G_\beta(1)SV_3 R_{PR}\,d\tau$$

Thus, to obtain the full solution requires 26 integrations for each time step. Furthermore, the expressions in cylindrical coordinates are

poorly behaved at small values of r.

This review of the theory of generalized rays is following Helmberger and Harkrider, 1978; Helmberger, 1983; Saikia, 1985; Langston and Helmberger, 1975; Heaton, 1978; Saikia and Herrmann, 1985, 1986. As mentioned above Cagniard de-Hoop solution depends upon the Laplace transform technique. In the next section we will discuss the wavenumber-frequency integration, which depends upon the Fourier transform.

2.3 Wavenumber-frequency integration

Wang and Herrmann (1980) gave expressions for the 10 Green's functions required for the wavefield due to an arbitrary point dislocation source and a point explosion buried in a multi-layer medium. Herrmann and Wang (1985) presented expressions for the k-ω domain response for the vertical displacement, U_z positive upward and in the tangential displacement, U_ϕ positive in a direction clockwise from north. These expressions contain the medium response due to the source contribution. Haskell (1964) propagator matrices are used to propagate the stress-displacement vector in a layered half-space. For each frequency, a suite of wave numbers is selected and the response is calculated. These expressions for the displacement can be represented by a double-couple without moment source model with the symbols **n** for the vector normal to the fault and **f** for the direction of force as used by Haskell (1963, 1964). Following Herrmann and Wang (1985)

the Fourier transformed displacements generated at free surface by such a dislocation source, for which n = 0, 1, 2 have the forms

$$u_z(r,0,\omega) = ZSS[(f_1n_1 - f_2n_2)\cos 2\phi + (f_1n_2 + f_2n_1)\sin 2\phi]$$
$$+ ZDS[(f_1n_3 + f_3n_1)\cos\phi + (f_2n_3 + f_3n_2)\sin\phi]$$
$$+ ZDD[f_3n_3] \qquad (2.3.1)$$

$$u_r(r,0,\omega) = RSS[(f_1n_1 - f_2n_2)\cos 2\phi + (f_1n_2 + f_2n_1)\sin 2\phi]$$
$$+ RDS[(f_1n_3 + f_3n_1)\cos\phi + (f_2n_3 + f_3n_2)\sin\phi]$$
$$+ RDD[f_3n_3] \qquad (2.3.2)$$

$$u_\phi(r,\phi,0,\omega) = TSS[(f_1n_1 - f_2n_2)\sin 2\phi - (f_1n_2 + f_2n_1)\cos 2\phi]$$
$$+ TDS[(f_1n_3 + f_3n_1)\sin\phi - (f_2n_3 + f_3n_2)\cos\phi] \qquad (2.3.3)$$

where, Following Herrmann and Wang (1985) the 10 Green's functions can be written as follows:

$$ZDD = \int_0^\infty F_1(k,\omega)J_0(kr)dk \qquad (2.3.4)$$

$$RDD = -\int_0^\infty F_2(k,\omega)J_1(kr)kdk \qquad (2.3.5)$$

$$ZDS = \int_0^\infty F_3(k,\omega)J_1(kr)dk \qquad (2.3.6)$$

$$RDS = \int_0^\infty F_4(k,\omega)J_0(kr)kdk \qquad (2.3.7)$$

$$-\frac{1}{r}\int_0^\infty [F_4(k,\omega)+F_9(k,\omega)]J_1(kr)dk$$

$$TDS=\int_0^\infty F_9(k,\omega)J_0(kr)kdk \tag{2.3.8}$$

$$-\frac{1}{r}\int_0^\infty [F_4(k,\omega)+F_9(k,\omega)]J_1(kr)dk$$

$$ZSS=\int_0^\infty F_5(k,\omega)J_2(kr)dk \tag{2.3.9}$$

$$RSS=\int_0^\infty F_6(k,\omega)J_1(kr)kdk \tag{2.3.10}$$

$$-\frac{2}{r}\int_0^\infty [F_6(k,\omega)+F_{10}(k,\omega)]J_2(kr)dk$$

$$TSS=\int_0^\infty F_{10}(k,\omega)J_1(kr)kdk \tag{2.3.11}$$

$$-\frac{2}{r}\int_0^\infty [F_6(k,\omega)+F_{10}(k,\omega)]J_2(kr)dk$$

$$ZEP=\int_0^\infty F_7(k,\omega)J_0(kr)dk \tag{2.3.12}$$

$$REP=-\int_0^\infty F_8(k,\omega)J_1(kr)kdk \tag{2.3.13}$$

In the above equations, ZSS is the Z-component displacement of a strike-slip type of source, ZDS is the Z-component displacement of a dip-slip type of source, and ZDD is the Z-component displacement of a 45° dip-slip type of source. The three components are all that are necessary to represent the P-SV motion for any shear-dislocation source (Harkrider, 1976). RSS and RDS include near-field terms. These terms decrease faster with distance than the others, thus, are important only at short distances. It should be pointed out that near-field terms have a higher order-Bessel function (J_n(kr)) than their far-field counterparts and the calculation of near-field terms demands special care. Following the same procedure, the tangential displacement also include the near-fields terms of TSS and TDS.

The vectors **n** and **f** are defined in a local coordinate system at the source in which the Cartesian axes are in the north, east, and downward directions. Following Herrmann (1978) and Herrmann and Wang (1985) the components of these vectors can be expressed in terms of the fault plane parameters of strike, dip, and slip. The strike, ϕ is measured clockwise from north, the dip, δ, is measured in a positive sense from the horizontal direction perpendicular to strike, and the rake, λ is measured on the fault plane in a counterclockwise sense from the horizontal direction of strike. With these conventions, all possible fault planes are encompassed by the ranges in the angles of $0° \leq \phi < 360°$, $0° \leq \delta \leq 90°$, and $-180° < \lambda < 180°$. It is noteworthy that with this notation, P-wave first motion at the center of the focal sphere is positive for positive values of λ and negative for negative value. The

expresses of **n** and **f** as functions of strike, dip and rake are

$$f_1 = \cos\lambda\cos\phi + \sin\lambda\cos\delta\sin\phi$$

$$f_2 = \cos\lambda\sin\phi - \sin\lambda\cos\delta\cos\phi$$

$$f_3 = -sin\lambda\sin\delta$$

$$n_1 = -sin\phi\sin\delta$$

$$n_2 = \cos\phi\sin\delta$$

$$n_3 = -cos\delta$$

2.4 Comparison of techniques

We have discussed two synthetic seismogram techniques. The Cagniard-de Hoop technique, usually referred to as the generalized ray method, constructs the solution by tracking the individual seismic ray arrivals from the source to receiver. This method is valid at high frequencies and works well for particular phases, but is poorly suited to models with many layers and at larger distances when a complete seismogram is desired. The other method involves expressing the solutions in terms of a double integral transformation over wavenumber and frequency. The complete solution, rather than individual rays, is obtained and intrinsic attenuation effects can be included. This method can handle a larger number of plane layers, but requires considerable computational effort, especially at high frequencies.

Herrmann and Wang (1985) compared several different approaches including a Cagniard de-Hoop technique using direct numerical integration (Johnson, 1974), a wavenumber-frequency integration along the real wavenumber axis using complex frequency (Bouchon, 1981). They found the wavenumber-frequency technique can yield a better solution for a given δt sampling interval than the Cagniard-de Hoop technique in the half space. They also compared the synthetic seismograms in the simple, single layer over a half-space model with different sample rates by using the generalized ray program (C.A. Langston), the contour integration technique of Wang and Herrmann (1980) and a locked-mode integration. The comparison suggests each numerical technique for synthesis has imperfections, however, peak amplitudes agree to within 10 percent, and waveform shapes are almost identical.

For our comparison of the two techniques, synthetic seismograms at short distance were obtained. The time function given by Herrmann (1979a, b) is used, which is proportional to the velocity of the dislocation, or equivalently the far-field displacement time history is used.

$$2\tau s(t) = \begin{cases} 0 & t \le 0 \\ 0.5(t/\tau)^2 & 0 < t \le \tau \\ -0.5(t/\tau)^2 + 2(t/\tau)^2 + 2(t/\tau) - 1 & \tau < t \le 3\tau \\ 0.5(t/\tau)^2 - 4(t/\tau) + 8 & 3\tau < t \le 4\tau \\ 0 & t \ge 4\tau \end{cases}$$

The velocity model used is shown in Table 1.3 of Chiu *et al*. (1993). For now, we ignore attenuation effects. The duration parameter τ is

set to 0.03 sec. and the depth and distance are fixed at 7.2 km and 9.7 km, respectively. These parameters are typical of our PANDA data set. The seismic moment is fixed at a value of 1.0E + 20 dyne-cm. The program genray85 (Langston, 1985, personal communication) using Cagniard de-Hoop method is used to compute the synthetic seismogram (Figure 2.2b) with 39 rays. Figure 2.2a shows the 10 Green's functions of (2.3.4) to (2.3.13) resulting from using the wavenumber integration program of hspec91 (Herrmann, 1991).

The comparison of Figures 2.2a and 2.2b shows that 1) The travel times, polarizations and wave-shapes of major phases included the direct P-, SV- and SH-waves, converted phases PS and SP of the shallow sediment are consistent. 2) The peak trace amplitudes in Figure 2.2a and Figure 2.2b agree to within 12% in ZDD and ZEP and within 5% for other Green's functions. When attenuation is considered, we can only use the wavenumber integration technique. As a result of this comparison we are satisfied that the number of rays are used in the Cagniard de-Hoop technique is adequate for modeling waveforms at these short epicentral distances.

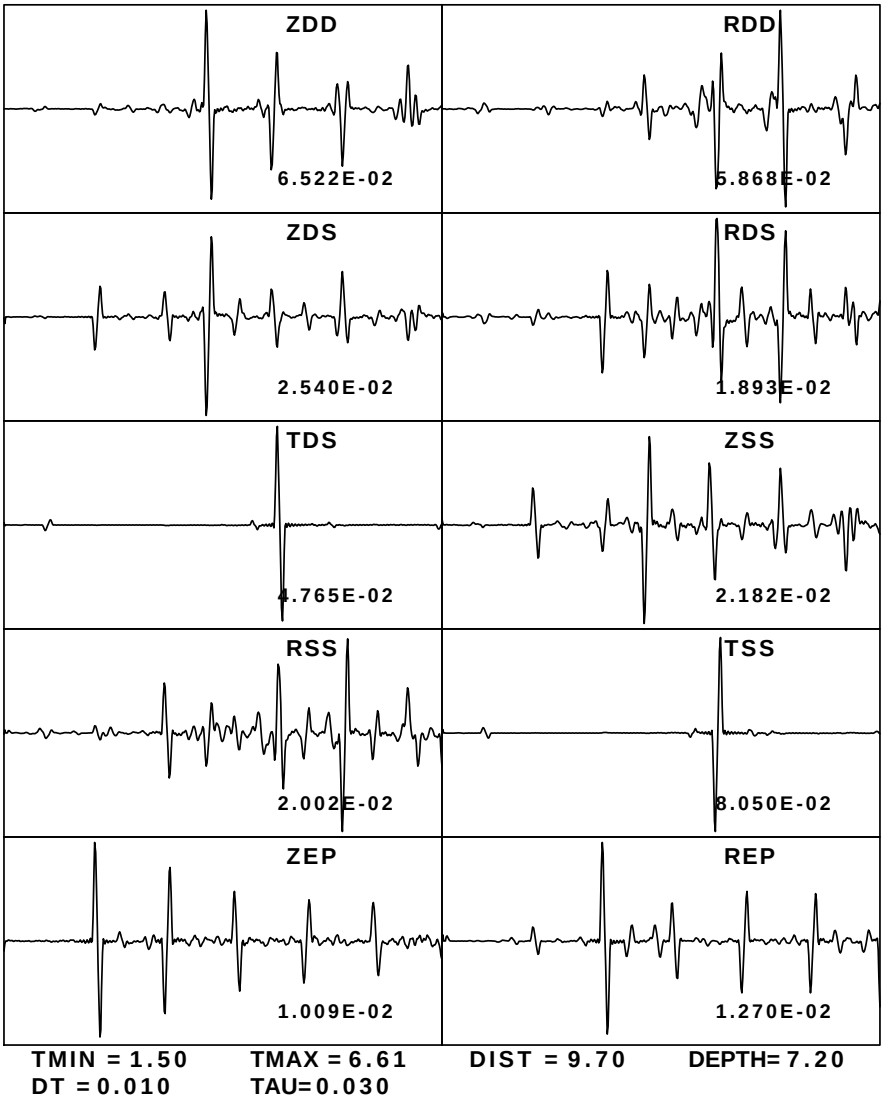

Fig. 2.2a. Synthetics at distance of 9.7 km using wave-number integration technique.

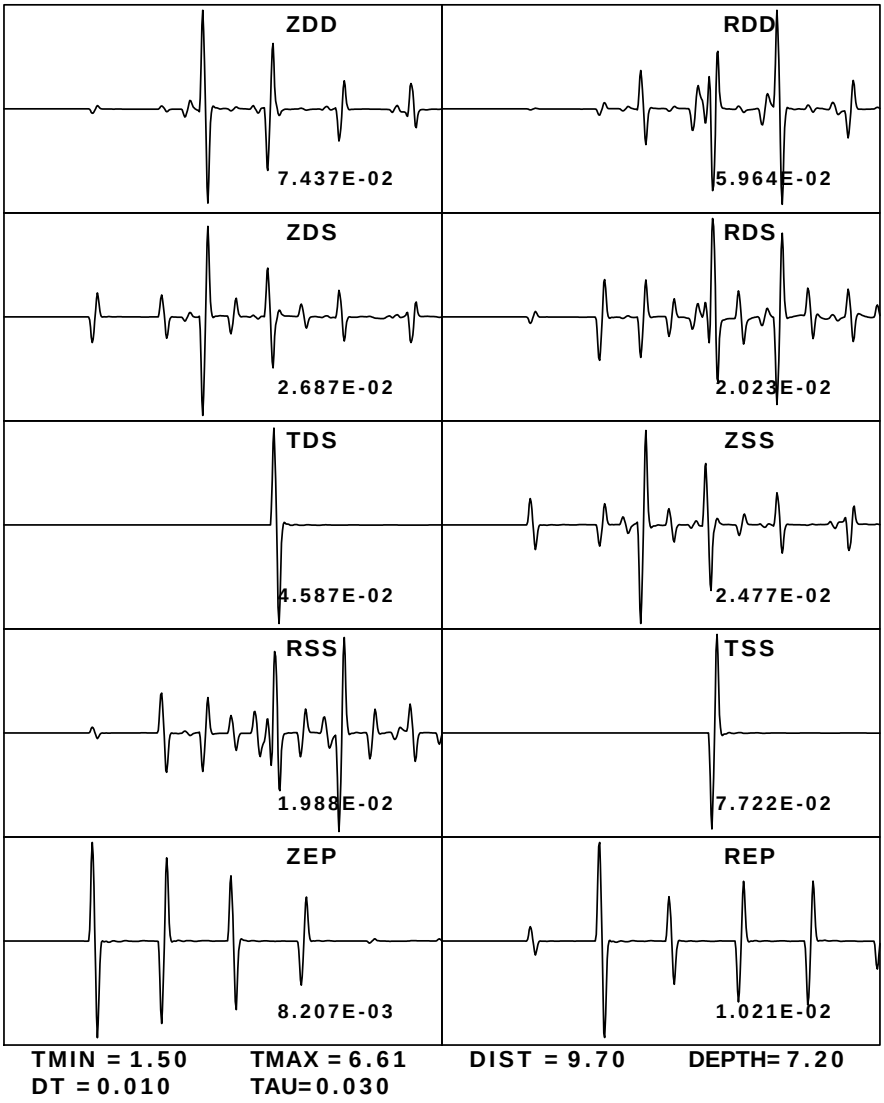

Fig. 2.2b. Synthetics at distance of 9.7 km using Cagniard de-Hoop technique.

CHAPTER 3

INVERSION FOR FAULTING PARAMETERS

3.1 Grid search inversion

The synthetic seismogram can be generated for any combination of dip, slip, and strike and equalized to have the same instrument response as the observations. The criteria to determine the best fault parameters is the one that yields the smallest misfit between observed and synthetic waveforms. This can be made by using a grid search inversion. Schwartz (1995) suggests a grid search procedure to obtain the double-couple mechanism and depth that best fits P, SV, and SH amplitude ratios observed at several stations. For each assumed source depth, amplitude ratios for incremental values of strike, dip, and rake at 10° intervals are constructed for each station and error function is defined as:

$$error = \left(\sum_{i=1}^{N} \left| \left(\frac{P}{SV} \right)_O - \left(\frac{P}{SV} \right)_t \right|_i^2 + \left| \left(\frac{P}{SH} \right)_O - \left(\frac{P}{SH} \right)_t \right|_i^2 + \left| \left(\frac{SV}{SH} \right)_O - \left(\frac{SV}{SH} \right)_t \right|_i^2 \right)^{1/2}$$

where o indicates the observed amplitude ratio and t the theoretical amplitude ratio for each assumed value of strike, dip and rake; N is the number of observations. Once the error function is computed for

all values of strike, dip and rake, an error threshold 50% higher than the lowest error is defined, and all source geometries yielding errors below this threshold are further examined (Schwartz, 1995)..

Saikia and Herrmann (1985, 1987) suggested a maximum normalized cross-correlation coefficient (or maximum unit vector dot product) between observed and predicted amplitude and amplitude ratio as criteria of the best fit.

The unit vector dot products are defined as:

$$\frac{P_{zs}\vec{e_1} + S_{vs}\vec{e_2}}{\left(P_{zs}{}^2 + S_{vs}{}^2\right)^{1/2}} \cdot \frac{P_{zo}\vec{e_1} + S_{vo}\vec{e_2}}{\left(P_{zo}{}^2 + S_{vo}{}^2\right)^{1/2}} \tag{3.1.1}$$

$$\frac{\frac{S_{rs}}{P_{zs}}\vec{e_1} + \frac{S_{rs}}{S_{hs}}\vec{e_2}}{\left((\frac{S_{rs}}{P_{zs}})^2 + (\frac{S_{rs}}{S_{hs}})^2\right)^{1/2}} \cdot \frac{\frac{S_{ro}}{P_{zo}}\vec{e_1} + \frac{S_{ro}}{S_{ho}}\vec{e_2}}{\left((\frac{S_{ro}}{P_{zo}})^2 + (\frac{S_{ro}}{S_{ho}})^2\right)^{1/2}} \tag{3.1.2}$$

Quantities with subscript z, r and h correspond to vertical, radial, and transverse components, respectively, s and o indicate the synthetic and observed amplitudes, respectively, and $\vec{e}_1$ and $\vec{e}_2$ are unit vectors. The optimal strike, dip and rake maximize this dot product.

Because of complex high-frequency waveforms observed at short distances, local whole-waveform modeling is more complicated than modeling teleseismic recording. The best way is to start with specific phases. Therefore, the direct P-, SV- and SH-amplitudes are used in this study. Following Saikia and Herrmann (1985), Liu *et al*. (1991) the grid-search procedure used is as follows:

1) Determine a velocity and attenuation model and relocate the earthquake hypocenter using this new earth model. It is very important to define the shallow structure near the receiver. The model must be able to predict the observed partition of P-wave ans S-wave amplitude on the vertical and radial components. For hard rock sites adequate shallow velocity structure is obtained by comparing the apparent incident angles of the observed and synthetic direct P-wave as Liu *et al*. (1991) did for the Goodnow earthquake aftershocks of New York. In an area covered by deep sediments some converted phases should also be predicted and the seismogram will exhibit strong Sp phases on the vertical component, and weak P-arrival and strong S-phase on the horizontal components. The NMSZ is predominantly soft-rock character. A sediment layer with very low P- and S-wave velocity results in seismic rays with near vertical incidence at the surface and S-waves converted to P-wave at the bottom of the sediment layer. The sediment depth under each station can be adjusted after comparing the S-arrival time between observed and synthetic seismograms. A high attenuation of seismic wave also occurs in the sediment layer. The correct Qp and Qs value are important for estimating the seismic moment and predicting the strong ground motion. We use Qp and Qs values obtained by Liu *et al*. 1994.

2) Calculate the Green's functions: Use the earth model to compute the Green's functions. Convolve the Green's functions with the appropriate instrument response and source-time function. If the attenuation is important, the wavenumber-frequency integration

method must be used. Otherwise the Cagniard-de Hoop technique can be used for the Green's function.

3) Both synthetic and observed seismograms are low-pass filtered to reduce the effect of the high-frequency noise and source corner frequency. For the small earthquakes, we use a two-pole Butterworth filter with corner frequency of 4.5 Hz.

4) Search to determine the optimal focal parameters. Search through all possible strike, dip and rake at a 3° increment, saving only those focal mechanisms which satisfy P-wave first-motion data. The criteria for judging the best focal mechanism is that the unit vector dot products between observed and predicted P-, SV- and SH- amplitudes and the amplitude ratios must both be maximized (3.1.2).

A best fit solution is also chosen on the minimization of the sum of square error, which measures the goodness of the fit to the observed seismic waveforms, and can be written as:

$$E_{RMS} = \left([\frac{1}{N} \sum_{1}^{N} (O_i - S_i)]^2 \right)^{1/2}$$

where O_i and S_i are observed and synthetic ground velocity, respectively; and N is the total number of samples of P-, SV-, and SH-waves.

5) Using the focal mechanisms satisfying step 3, synthetic seismograms are generated. If the waveforms do not agree with the observed waveforms, the earth model should be modified, events should be relocated, and each step should be repeated.

3.2 Moment tensor inversion

3.2.1 The moment tensor

The seismic moment tensor, M , is a second-order tensor containing the most information about the source (not the time function or corner frequency). The seismic moment tensor can be obtained from observing waves, whose wave lengths are much longer than the linear dimension of $\sum$, the fault surface. In this case, the source is effectively a point source. A seismic moment tensor is a general concept, describing a variety of seismic source models, with the shear dislocation (double couple source) being just one of them (Jost and Herrmann, 1989; Frohlich and Apperson, 1992). The moment tensor completely describes a linear combination of equivalent point forces, which can be used to model signals from displacement on a fault surface, rapidly propagating metastable phase transitions, sudden volume collapse due to phase transitions, or sudden volume increase due to explosions.

The specific combination of equivalent forces can be determined from an analysis of the eigenvalues and eigenvectors of the moment tensor. The sum of the eigenvalues of the moment tensor describes the volume change in the source. If the sum is greater than 0, the source has a volumetric explosion component. If the sum is less than 0, the source has an implosive component. If the sum is 0 and one eigenvalue = 0, the source only has deviatoric components, representing a

pure double couple. If none of the eigenvalues vanish and their sum still equals zero, the moment tensor can be decomposed into a major and minor double couple, or a double couple and a compensated linear vector dipole (CLVD) (Frohlich and Apperson, 1992). A CLVD is a dipole that is corrected for the effect of volume change. In general, a complete moment tensor can be the superposition of an isotropic component and three vector dipoles (or three CLVD's, or three double couples).

Following Aki and Richards (1980), the displacement function U_j at r due to general displacement discontinuity across Σ can be written ass

$$U_j(r,t) = \int_{\Sigma}\int m_{pq} * G_{jp,q}(r,t;r_{0,}0)d\Sigma \qquad (3.2.1)$$

where m_{pq} are the elements of the moment density tensor, and

$$m_{pq} = [u_i]V_j C_{ijpq}$$

where r is the location coordinate of the receiver, r_0 is a point on the fault surface, and dΣ is an element on the fault surface Σ. For the far-field approximation, the contributions from different surface elements dΣ are all approximately in phase and the entire surface may be considered as a system of couples. $G_{jp,q}$ describes nine generalized couples. The derivative of a Green's function component with respect to the source coordinate ξ_q is equivalent to a single couple with arm in the ξ_q direction. For p=q, i.e. force in the same direction as the arm, the generalized couples are vector dipoles (Figure 3.1). Thus, the moment tensor component M_{pq} gives the excitation of the generalized

(p,q) couple. If there is a common source time function to m_{pq}, and if Σ is small compared to the wave-length, we define a moment tensor as equal to the integral of the moment density over Σ, i.e.,

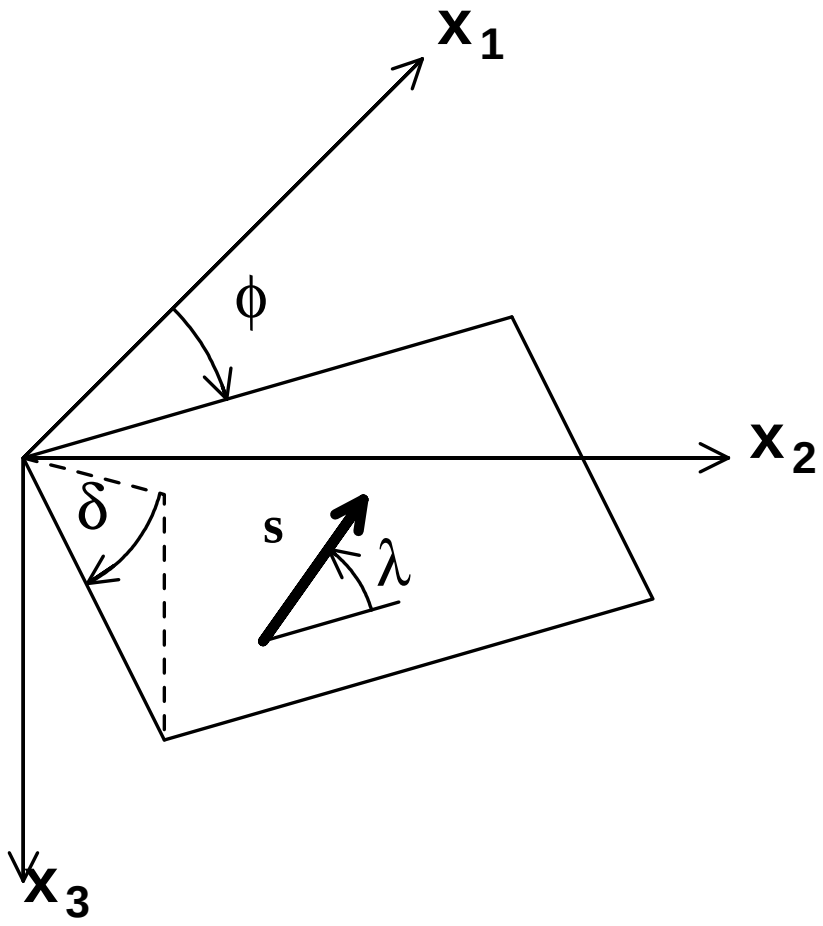

Fig. 3.1. Definition of the Cartesian coordinates (x1,x2,x3) and ($x = x_1$, $y = x_2$, $z = x_3$). The origin is at the epicenter. Strike is measured clockwise from north, dip from horizontal down, and slip counterclockwise from horizontal. u and μ are the slip vector and fault normal, respectively (modified after Aki and Richards, 1980)

$$M_{pq} = \int_{\Sigma}\int m_{pq}\, dSIGMAA$$

The expression (3.2.1) can be rewritten as

$$U_j(r,t) = M_{pq} * G_{jp,q} \tag{3.2.2}$$

The moment tensor components M_{pq} in (3.2.2) in an isotropic medium for a double couple of equivalent force are given

$$M_{pq} = \mu A(\gamma_p u_q + \gamma_q u_p) \tag{3.2.3}$$

where $\vec{u}$ denotes the slip vector on the fault surface, $\vec{\gamma}$ is the vector normal to the fault plane (Aki and Richards, 1980; Ben-Menahem and Singh, 1981, Jost and Herrmann, 1989), and μ is the shear modulus, and A is the area of the fault plane. Note that the contributions of the vector of the fault normal $\vec{\gamma}$ and the slip vector $\vec{u}$ are symmetric in (3.2.3). The term $u_p\ \gamma_q + u_q\ \gamma_p$ in (3.2.3) forms a tensor, D, describing a double couple. This tensor is real and symmetric, having real eigenvalues and orthogonal eigenvectors. Let $\vec{t}$, $\vec{b}$, and $\vec{p}$ designate the orthogonal eigenvectors to the above eigenvalues (Herrmann, 1975):

$$\vec{t} = \frac{1}{\sqrt{2}}\left(\vec{\gamma} + \vec{u}\right)$$

$$\vec{b} = \vec{\gamma} \times \vec{u}$$

$$\vec{p} = \frac{1}{\sqrt{2}}\left(\vec{\gamma} - \vec{u}\right)$$

where the eigenvectors give the directions of the principal axis (Herrmann, 1975). The eigenvector $\vec{b}$ corresponding to the eigenvalue zero gives the null-axis, the eigenvector $\vec{t}$ corresponding to the positive

eigenvalue gives the tension axis, T , and the eigenvector $\vec{p}$ corresponding to the negative eigenvalue gives the pressure axis, P. The P-axis is in the direction of maximum compressive motion on the fault surface; the T-axis is the direction of maximum tensional motion.

If strike ϕ, dip δ, and rake λ, of the faulting (Figure 3.2, Aki and Richards, 1980) are known, the slip vector u and the fault normal $\vec{\gamma}$ are given by (Aki and Richards, 1980)

$$\vec{u} = u_0(\cos\lambda\cos\phi + \cos\delta\sin\lambda\sin\phi)\vec{e}_x \tag{3.2.4}$$

$$+u_0(\cos\lambda\sin\phi - \cos\delta\sin\lambda\cos\phi)\vec{e}_y$$

where u_0 is the mean displacement on the fault plane. The fault normal $\vec{\gamma}$ is

$$\vec{\gamma} = -sin\delta\sin\phi\vec{e}_x + \sin\delta\cos\phi\vec{e}_y - \cos\delta\vec{e}_z \tag{3.2.5}$$

The strike of the fault plane, ϕ, is measured from north, with the fault plane dipping to the right when looking along the strike direction. The dip, δ is measured down from the horizontal. The rake, λ is the angle between the strike direction and the direction the hanging wall moved relative to the foot wall. The rake is positive when measured counterclockwise as viewed from the hanging wall side (Figure 3.2).

The scalar seismic moment is defined as

$$M_0 = \mu A u_0 \tag{3.2.6}$$

Now (3.2.3), (3.2.4), (3.2.5) and (3.2.6) lead to the expressions for different element M_{pq} (Mendiguren, 1977)

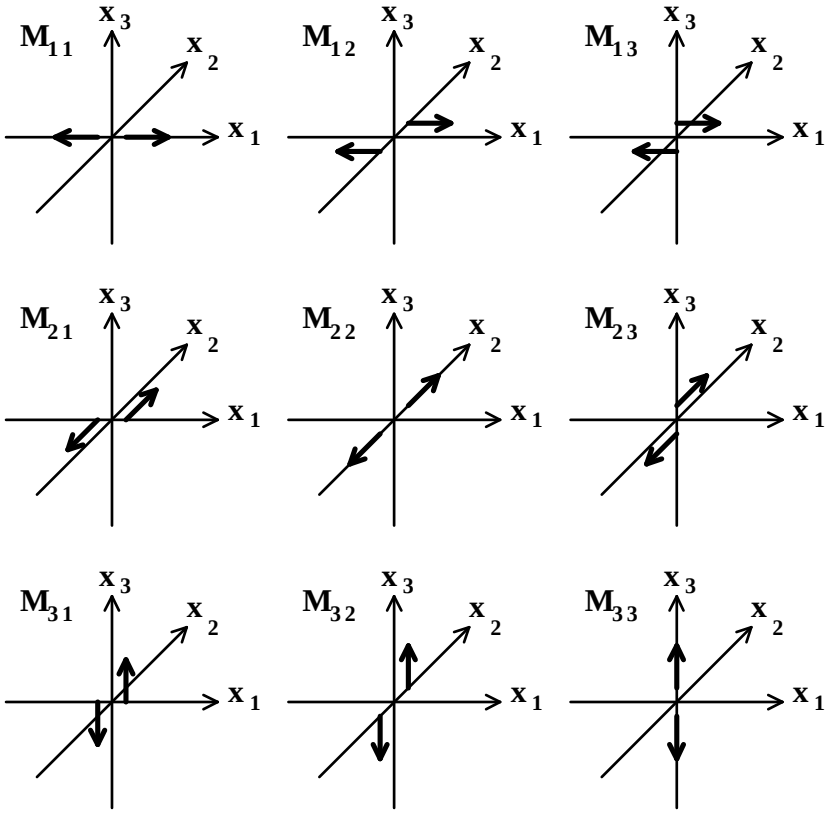

Fig. 3.2. Nine generalized couples representing M_{pq} in (3.2.2) (modified after Aki and Richards, 1980).

$$M_{11} = -M_0(sin\delta \cos\lambda \sin 2\phi + sin2\delta \sin\lambda \sin^2\phi) \tag{3.2.7}$$

$$M_{22} = M_0(\sin\delta \cos\lambda \sin 2\phi - \sin 2\delta \sin\lambda \cos^2\phi)$$

$$M_{12} = M_0(\sin\delta \cos\lambda \cos 2\phi + \frac{1}{2}\sin 2\delta \sin\lambda \sin 2\phi)$$

$$M_{13} = -M_0(\cos\delta \cos\lambda \cos 2\phi + \cos 2\delta \sin\lambda \sin\phi)$$

$$M_{23} = -M_0(\cos\delta \cos\lambda \sin\phi - \cos 2\delta \sin\lambda \cos\phi)$$

$$M_{33} = -(m_{11} + m_{22})$$

The scalar seismic moment can be determined from a given moment tensor by

$$M_0 = \frac{1}{2}(|m_1| + |m_2|)$$

where m_1 and m_2 are the largest eigenvalues (in the absolute sense). The seismic moment can equivalently be estimated by the relations

$$M_0 = [\sum \frac{M_{kj}^2}{2}]^{\frac{1}{2}} = [\sum \frac{m_i^2}{2}]^{\frac{1}{2}}$$

Using (3.2.7) with (3.2.4) and (3.2.5) (Langston, 1981), we can obtain

$$A_1 = \frac{1}{2}(M_{11} - M_{22})cos(2az) + M_{12}sin(2az) \qquad (3.2.8)$$

$$A_2 = M_{13}cos(az) + M_{23}\sin(az)$$

$$A_3 = -\frac{1}{2}(M_{11} + M_{22})$$

$$A_4 = \frac{1}{2}(M_{11} - M_{22})\sin(2az) - M_{12}\cos(2az)$$

$$A_5 = -M_{23}cos(az) + M_{13}\sin(az)$$

The definition of A_i can be found in (2.1.5). The focal mechanism can determined from the moment tensor components.

3.2.2 Moment tensor inversion

The vertical, radial and transverse displacements can be written in the following formats (Longston and Helmberger, 1975; Longston, 1981):

$$W(r,z,t) = s(t) * \sum_{i=1}^{5} H_{w1}(r,z,t) M_i \tag{3.2.9}$$

$$Q(r,z,t) = s(t) * \sum_{i=1}^{5} H_{q1}(r,z,t) M_i$$

$$V(r,z,t) = s(t) * \sum_{i=1}^{5} H_{v1}(r,z,t) M_i$$

where $M_1 = M_{11}$, $M_2 = M_{22}$, $M_3 = M_{12}$, $M_4 = M_{13}$, $M_5 = M_{23}$, and (Jost and Herrmann, 1989):

$$H_{w1} = 0.5(ZDD - ZSScos(2AZ))$$

$$H_{w2} = 0.5(ZDD + ZSScos(2AZ))$$

$$H_{w3} = -ZSSsin(2AZ)$$

$$H_{w4} = -ZDScos(AZ)$$

$$H_{w5} = -ZDSsin(AZ)$$

To get H_{qi} (i = 1, 2, 3, 4, 5), replace the ZDD, ZDS, ZSS by RDD, RDS, RSS, respectively.

$$H_{v1} = -0.5TSSsin(2AZ)$$

$$H_{v2} = 0.5TSSsin(2AZ)$$

$$H_{v3} = TSScos(2AZ)$$

$$H_{v4} = -TDSsin(AZ)$$

$$H_{v5} = TDScos(AZ)$$

where DD, DS, and SS correspond to 45° dip-slip, pure vertical dip-slip, and pure vertical strike-slip fault for either vertical or radial motion and similarly TDD, TDS, and TSS for transverse motion (see (2.2.6) to (2.2.15). The ground motion predicted by equation (3.2.9) is now linearly dependent on the elements M_{ij} if the source-time function is assumed known. Equation (3.2.9) can be written as

$$W = AM \tag{3.2.10}$$

$$W = [w_{1,}w_{2,}w_{3,}w_{4,\ldots,}w_m]^T \tag{3.2.11}$$

$$M = [M_{1,}M_{2,}M_{3,}M_{4,}M_5]^T \tag{3.2.12}$$

For P vertical and radial ground motion,

$$[a_{ij}] = [\frac{\partial(w_j)}{\partial M_j}]_i \tag{3.2.13a}$$

or for SV vertical and radial ground motion,

$$[a_{ij}] = [\frac{\partial(q_j)}{\partial M_j}]_i$$

and for SH ground motion,

$$[a_{ij}] = [\frac{\partial v_j}{\partial M_j}]_i \tag{3.2.13b}$$

where j = 1, 2, 3, 4, 5 and i = 1, 2,...n, observed data. From (3.2.10), a

least-squares inversion for the moment tensor elements can be performed. By singular value decomposition of A ($n \times 5$) in the form of $U\Lambda V^T$, where Λ is an $n \times 5$ diagonal matrix and U and V are $n \times n$ and 5×5 orthogonal matrices, respectively, n being the total number of observations, the solution vector can be written as

$$M = V\Lambda^{-1}U^T W$$

After vectorial expansion this can be written as

$$M = \frac{1}{\lambda_1} v_1 u_1^T W + \frac{1}{\lambda_2} v_2 u_2^T W + \cdots + \frac{1}{\lambda_p} v_p u_p^T W$$

Let $\alpha_i = u_i^T$W (i = 1, ..., n) be the magnitude of the projection of the vector W onto the i' th observation eigenvector, u_j. Then

$$M = \frac{\alpha_1}{\lambda_1} v_1 + \frac{\alpha_2}{\lambda_2} v_2 + \cdots + \frac{\alpha_n}{\lambda_n} v_n$$

Hence, the moment tensor elements are the weighted sum of the p eigenvectors, each with weight $\frac{\alpha_i}{\lambda_i}$. Evidently, if $\frac{\alpha_i}{\lambda_i}$ is small, the term $(\alpha_i/\lambda_i)v_i$ has less influence on the solution M. But, if λ_i is very small, the ratio α_i/λ_i tends to grow large for which the term α_i/λ_i contributes significantly to the solution M. There are two ways to avoid this problem: one is by ignoring this noisy term completely in further calculations, and the other is by damping the eigenvalue appropriately. Either approach produces a non-unique solution. The degree of non-uniqueness in the solution can be tested by inspecting the nature of the resolution matrix, R, defined by

$$R = VV^T$$

For a true and unique solution, R must be equal to I, the identity matrix, which makes the parameters linearly independent. By damping, i.e., weighting the diagonal elements of the matrix A, the R-matrix is changed and the linear independence among the parameters is destroyed. Therefore, it is desirable to keep R close to I.

In this work, the inversion was performed on the amplitudes of the following phases: direct P, direct SV, using both the vertical and radial components; and direct SH from the tangential component, rather than on the entire waveform. Since the inversion is linear, the appropriateness of the solution was tested by directly comparing the amplitudes of the observed and predicted phases. The eigenvalues were sometimes damped, but in such as way as keep the resolution matrix VV^T close to an identity matrix, and to achieve a better one-to-one correlation between the observed and calculated amplitudes.

Table 3.1 is an example of moment tensor inversion results..

3.3 Confidence limits and data importance

3.3.1 Introduction

The error in the focal mechanism is difficult to quantify in an absolute sense, because of the interdependence of the structure, source-time function, source depth and focal mechanism on the final waveforms. In this study, the application of an F-test permits

Table 3.1. Results of moment tensor inversion of event 1103.

Correlation Coefficient of observed and synthetic seismogram:
P-waves: 0.95
S-waves: 0.91

Element of moment tensor ($\times 10^{20}$dyn-cm):

MXX	:	-0.1768E-02 ±	0.1359E-07
MYY	:	0.8893E-02 ±	0.1377E-07
MXY	:	-0.2693E-02 ±	0.2030E-07
MXZ	:	0.2313E-02 ±	0.2447E-07
MYZ	:	0.4958E-02 ±	0.3986E-07

Scalar seismic moment ($\times 10^{20}$dyne-cm) : 0.1018E-01
Eigenvalues of M-matrix ($\times 10^{20}$dyne-cm):

0.1063E-01 -0.9542E-03 -0.9673E-02

CLVD = 0.9%

Major double couple :

P axis	: azimuth	-0.8117E+02	plunge	-0.1455E+02	
T axis	: azimuth	0.2189E+03	plunge	0.6260E+02	
	dip = 38	slip = 131	strike = 217		
		or			
	dip = 63	slip = 64	strike = 350		

Minor double couple :

P axis	: azimuth	0.5393E+02	plunge	-0.5831E+02	
T axis	: azimuth	0.2926E+02	plunge	0.2929E+02	
	dip = 22	slip = -119	strike = 81		
		or			
	dip = 71	slip = -79	strike = 292		

---

confidence bounds to be placed on the P and T-axis of the double-couple focal mechanisms. Confidence contours will give the range of focal parameters. We will discuss the mathematical model for application of the F-test to the nonlinear case.

Suppose the postulated model of the relationship between observed, synthetic and unknown parameters is of the form (Draper and Smith, 1966))

$$Y = f(\xi_1, \xi_2, \cdots, \xi_k; \theta_1, \theta_{2,} \cdots, \theta_p) + \varepsilon \tag{3.3.1}$$

where θ_i are the unknown parameters and ξ_i are modeling parameters. If we write

$$\xi = (\xi_1, \xi_2, \cdots, \xi_k)^T$$

$$\theta = (\theta_1, \theta_2, \cdots, \theta_p)^T$$

we can simplify Equation (3.3.1) to

$$Y = f(\xi, \theta) + \varepsilon \tag{3.3.2}$$

or

$$E(Y) = f(\xi, \theta)$$

We assume that E (ε) = 0, that the errors are uncorrelated, that V (ε) = σ^2 and, usually, that $\varepsilon \approx$ N (0, σ^2).

When there are n observations available of the form

$$Y_u, \xi_{1u}, \xi_{2u}, \cdots, \xi_{ku}$$

for u = 1, 2, ... , n, we can write the model in an alternative form

$$Y_u = f(\xi_{1u}, \xi_{2u}, \ldots, \xi_{ku}; \theta_{1,}\theta_{2,\ldots,}\theta_p) + \varepsilon_u \tag{3.3.3}$$

where ξ_u =$(\xi_{1u}, \xi_{2u}, \cdots, \xi_{ku})^T$. The assumption of normality and independence of the errors can now be written as ε = (ε_1, ε_2, ... , ε_n)^T. We define the error sum of squares for the nonlinear model and given data as

$$s(\theta) = \sum_{u=1}^{n} [Y_u - f(\xi_u, \theta)]^2 \tag{3.3.4}$$

Note that since Y_u and ξ_u are fixed observations, the sum of squares is a function of θ. We will denote by $\theta_{\min}$, a least squares estimate of θ, that is a value of θ which minimizes S(θ).

To find the least squares estimate $\theta_{\min}$ we need to differentiate Eq. (3.3.4) with respect to θ. This provides the p normal equations, which must be solved for $\theta_{\min}$. The normal equations take the form

$$\sum_{u=1}^{n}[Y_u - f(\xi_u, \theta)][\frac{\partial f(\xi_u, \theta)}{\partial \theta_i}]_{\theta=\theta_{\min}} = 0 \tag{3.3.5}$$

for i = 1, 2, ..., p, where the quantity denoted by brackets is the derivative of f (ξ_u , θ) with respect to θ_i with all θ's replaced by the corresponding $\theta_{\min}$ which have the same subscript.

An exact confidence contour is defined by taking S(θ) = constant, but since we do not know the correct distribution properties in the general nonlinear case, we are unable to obtain a specified probability level (Draper and Smith, 1966). However, we can, for example, choose the contour such that

$$S(\theta) = S(\theta)_{\min}[1 + \frac{p}{n-p} F(p, n-p, 1-\alpha)] \tag{3.3.6}$$

where n shows the number of observed data and p is the unknown parameters, α is reliability. If the model is linear, provides an exact, ellipsoidal 100(1- α)% boundary and label it as an approximate 100(1 - α)% confidence contour in the nonlinear case. Note that the contour so determined will be a proper correct confidence contour in this case (and will not be elliptical in general), and it is only the probability level which is approximate. In the linear model case, continuity of constant S(θ) in the parameter space, or θ- space, consist of concentric

ellipses. When the model is nonlinear the contours are sometimes banana-shaped, often elongated. We can call such regions approximate 100(1- α)% confidence regions for θ (Draper and Smith, 1966). The banana-shaped regions of parameters of θ were obtained. The minimum value of S(θ) is attained at the point ($\theta = \theta_1, \theta_2, \ldots, \theta_p$) which lies in the center of the banana-shaped parameter's region.

In general, when a linear form of a nonlinear model is used, all the usual formula and analyses of linear regression theory can be applied. Any results obtained are, however, only valid to the extent that the linearized form provides a good approximation to the true model.

3.3.2 Application of confidence limit to the study

Our model is of the form

$$Y = f(\xi, \theta) + \varepsilon \tag{3.3.7}$$

where Y are the observed amplitudes of P-, SV- and SH-waves:

$$(Y_i) = (A_{P_i}, A_{SV_i}, A_{SH_i}) \tag{3.3.8}$$

and the synthetic amplitudes of P- and S-waves of Eight Green's functions are

$$\xi_i = (\xi_{P1i}, \xi_{P2i}, \xi_{P3i}, \xi_{P4i}, \xi_{P5i}, \xi_{P6i,}\xi_{P7i}, \xi_{P8i}, \tag{3.3.9}$$

$$\xi_{S1i}, \xi_{S2i}, \xi_{s3i}, \xi_{S4i}, \xi_{S5i}, \xi_{S6i}, \xi_{S7i}, \xi_{S8i})$$

where, ξ are functions of the focal parameters of the event:

$$\theta = (\theta_1, \theta_2, \theta_3) \tag{3.3.10}$$

where θ_1 = strike , θ_2 = dip, and θ_3 = rake, respectively. When there are n stations where the observed amplitudes and Green's function are obtained for an earthquake

$$Y_i, \xi_i$$

we can write the model in the alternative form

$$Y_i = f(\xi_{P1i,}\xi_{P2i,}\ldots,\xi_{P8i,}\xi_{S1i,}\xi_{S2i,}\ldots,\xi_{S8i,}\theta_1,\theta_2,\theta_3) + \varepsilon_i$$

and simply write:

$$Y_i = M_0\xi_i + \varepsilon_i \tag{3.3.11}$$

and compatible

$$S(\theta) = \sum_{i=1}^{n}[Y_i - M_0\xi_i(\theta)]^2 \tag{3.3.12}$$

Note that since Y_i and ξ_i are fixed observations and synthetics, the sum of squares is a function of the focal parameters, θ. A least squares sum of θ (λ, θ, δ), that is a value of θ which minimizes S(θ).

$$\frac{\partial S(\theta)}{\partial M_0} = 0 \tag{3.3.13}$$

which could also be located using a grid search. The seismic moment is estimated

$$M_0 = \frac{\sum_{i=1}^{n}\xi_i Y_i}{\sum_{i=1}^{n}\xi_i^{\,2}} \tag{3.3.14}$$

and

$$S(\theta) = \sum_{i=1}^{n}(Y_i - M_0\xi_i)^2 = \sum_{i=1}^{n} Y_i^2 - \frac{(\sum_{i=1}^{n} Y_i\xi_i)^2}{\sum_{i=1}^{n} \xi_i^2} \qquad (3.3.15)$$

A grid search method is used in the space of the focal parameters. The S(θ) is calculated at every point of grid in the range of dip from 0° to 90°, rake from -180° to 180°, strike from 0° to 360°. The smallest $S_{\min}$ (θ) is found. The 100(1-α)% confidence contour can be drawn in any particular region of the parameter space. Figures 3.3 (a, b, c, d) and 3.4 (a, b, c, d) show the confidence contours of 90%, 95%, 99% of the focal parameters of events 1103 and 0647. Table 3.2 gives the range of focal parameters in 90% confidence of the two events. The confidence contours show the banana shape and the "best" results lie in the center of the contour.

3.4 Maximum normalized cross-correlation coefficient and the smallest sum of squares between observed and predicted waveforms

Table 3.2. Range of focal mechanisms with 90% confidence.

EVENTS	$S_{\min}$	STRIKE		DIP		RAKE	
		λ°	ε°	d°	ε°	δ°	ε°
1103	1.28000E-08	350 - 10	≤ 20	55 - 70	≤ 15	50 - 70	≤ 20
0647	7.33900E-07	125 - 145	≤ 20	45 - 65	≤ 20	0 - 25	≤ 25

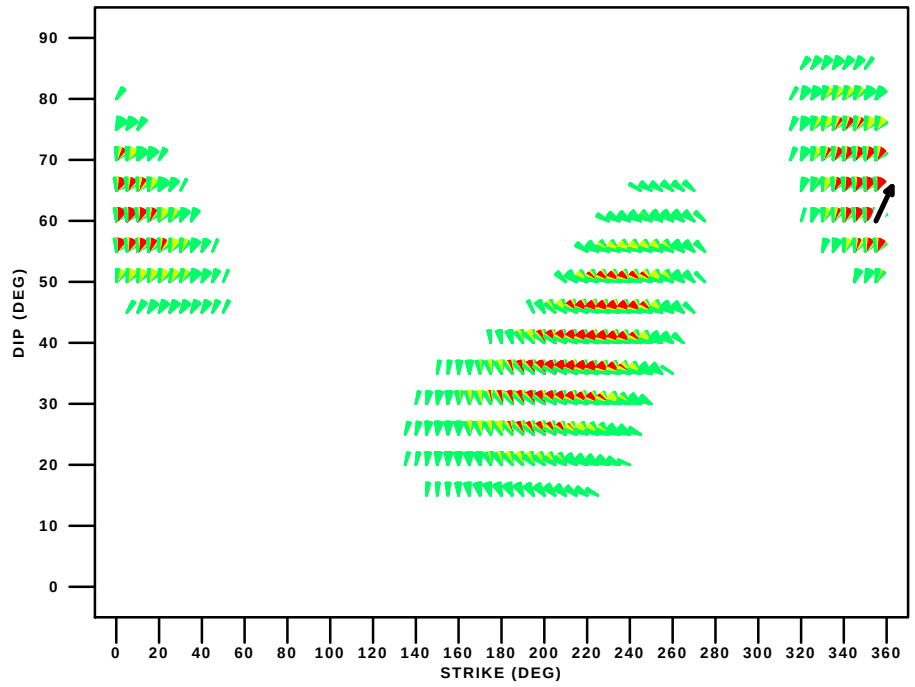

Fig. 3.3a. The result of grid search for event 1103. The arrow shows the focal mechanism (strike=355°, dip=60°, and rake=65°) of the smallest misfit between synthetic and observed P-, SV-, and SH-amplitudes. The angle between arrow and horizontal line (anticlockwise) is rake. The shading area suggests the focal parameters with a 90%, 95% and 99% confidence of F-test, respectively.

Saikia and Herrmann (1985, 1986) suggested the maximum normalized cross-correlation coefficient as a criterion of best fit between synthetic and observed waveforms:

$$cos(\theta) = \frac{X.Y}{|X| * |Y|} = \frac{\sum_{i=1}^{n}(x_i y_i)^2}{\sum_{i=1}^{n} x_i^2 \sum_{i=1}^{n} y_i^2} \qquad (3.3.16)$$

Where X and Y are vector of synthetic and observed amplitudes, θ is the focal parameters. If the synthetic and observed waves are identical, cos(θ) must be unit. In a grid search procedure we chose the focal

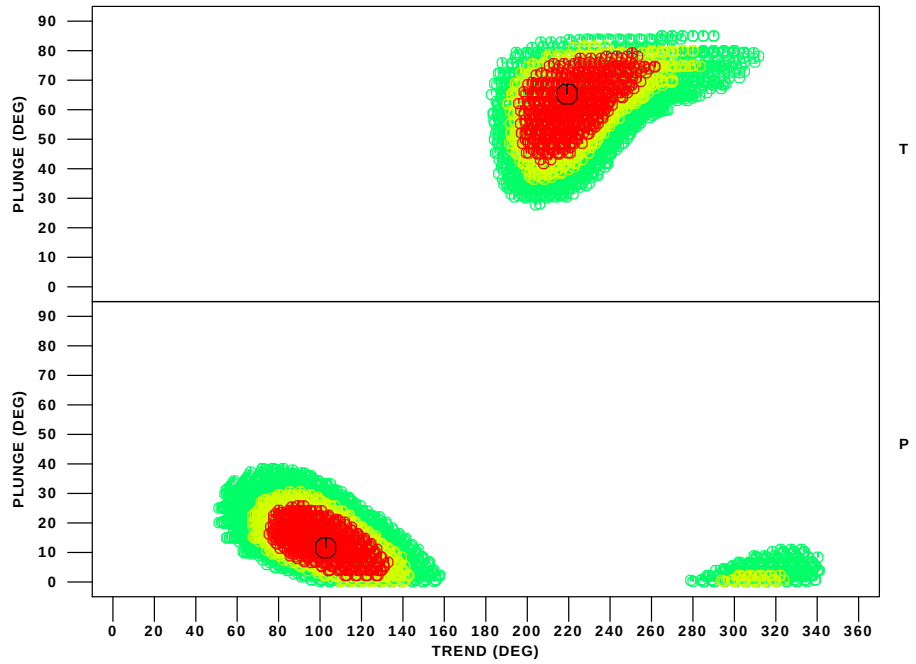

Fig. 3.3b. P- and T- axes of the event 1103 using grid search. The circle shows the best source parameter. The dark, light gray and gray area correspond to the 90%, 95%, and 99% confidence bounds of the F-test, respectively.

mechanisms as the best solution as that which maximizes of cos(θ) is found. Both the maximum normalized cross-correlation coefficient and the minimum sum of square error can be used and obtained similar results. If we assume the model (3.3.11), then (3.3.15) can be written as

$$S(\theta) = (\sum_{i=0}^{n} {y_i}^2)(1 - \frac{\sum_{i=1}^{n}(x_i y_i)^2}{\sum_{i=1}^{n} {x_i}^2 \sum_{i=1}^{n} {y_i}^2}) \qquad (3.3.17)$$

after comparing (3.3.16) and (3.3.17), we find the relation between S(θ) cos(θ) is:

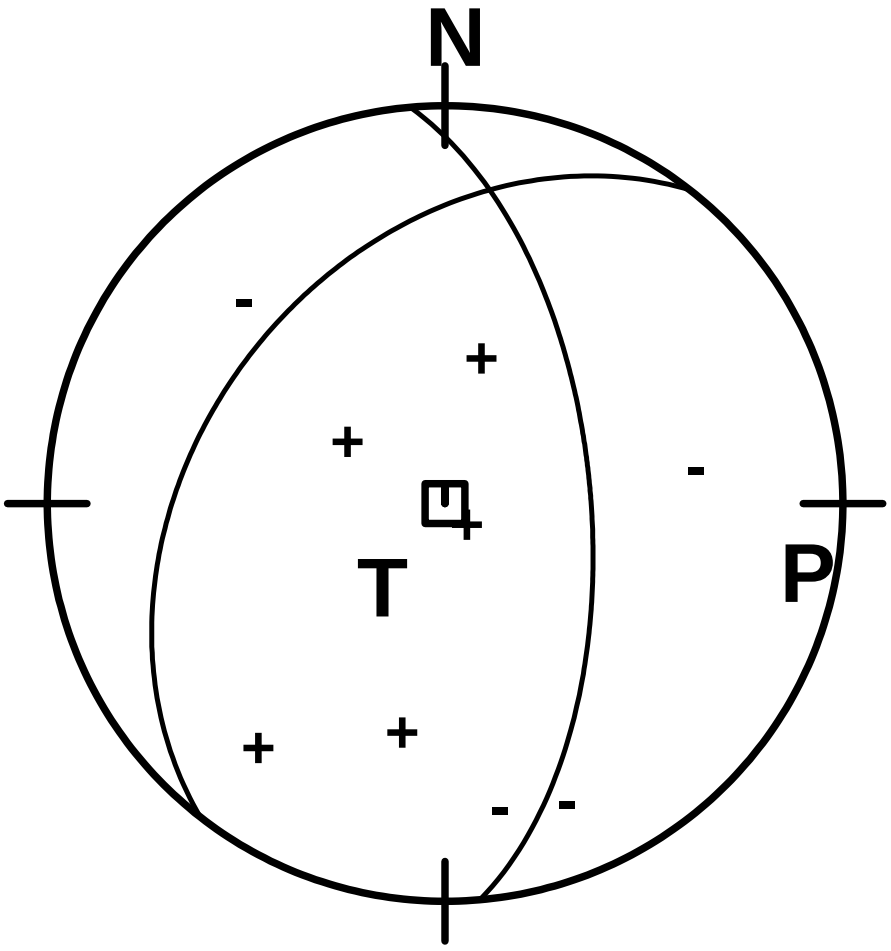

Fig. 3.3c. The smallest misfit focal mechanism of event 1103. The compressional P-wave observations are shown by +. The projection is lower hemisphere.

$$S(\theta) = \sum_{i=1}^{n} {y_i}^2 (1 - \cos^2(\theta)) \qquad (3.3.18))$$

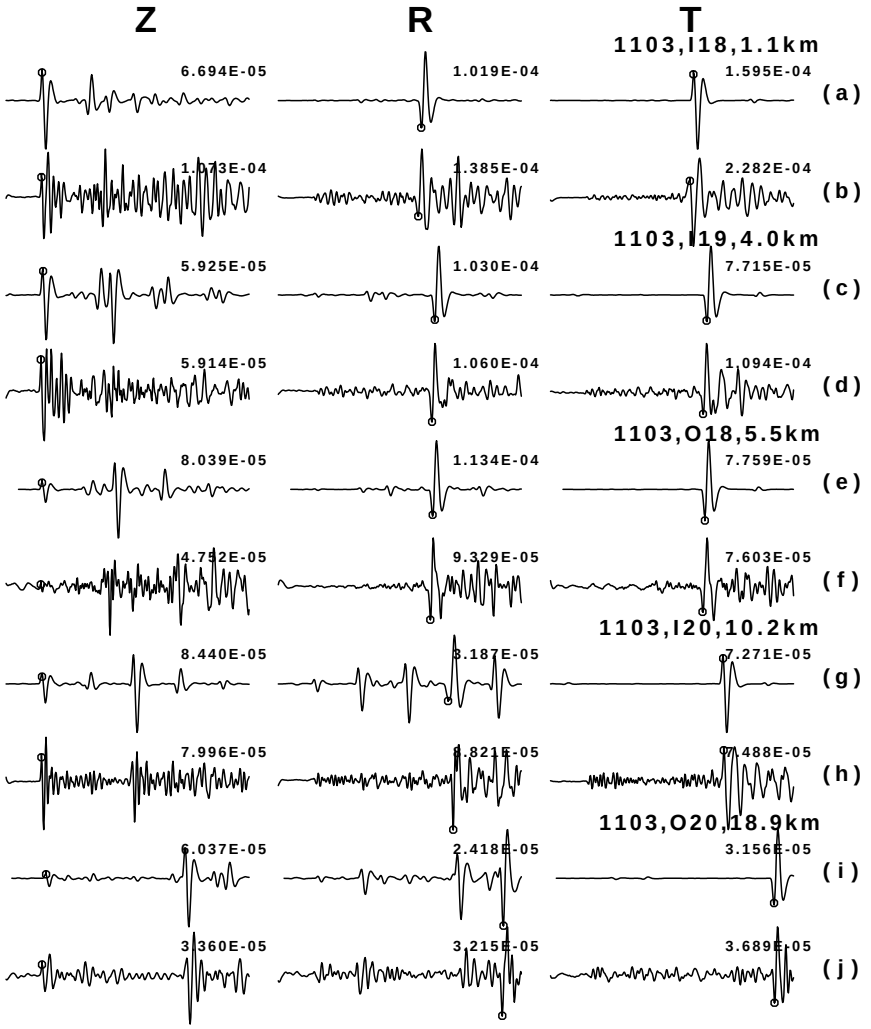

Fig. 3.3d. Comparison between 3-component observed and synthetic velocity seismograms of event 1103 at 5 stations. The length of each time history is 4.25 sec. P-, SV- and SH- amplitudes used in the inversion are indicated by circles. Synthetic seismograms were obtained by using the corresponding focal parameters in Figure 3.3c, which were obtained from 9 stations' data. The number by each trace is the maximum velocity (cm/s). The direct P-, SV- and SH-wave amplitudes, even some converted phases (PS, SP which were not used in the inversion) of synthetic seismograms are consistent with those of observed seismograms.

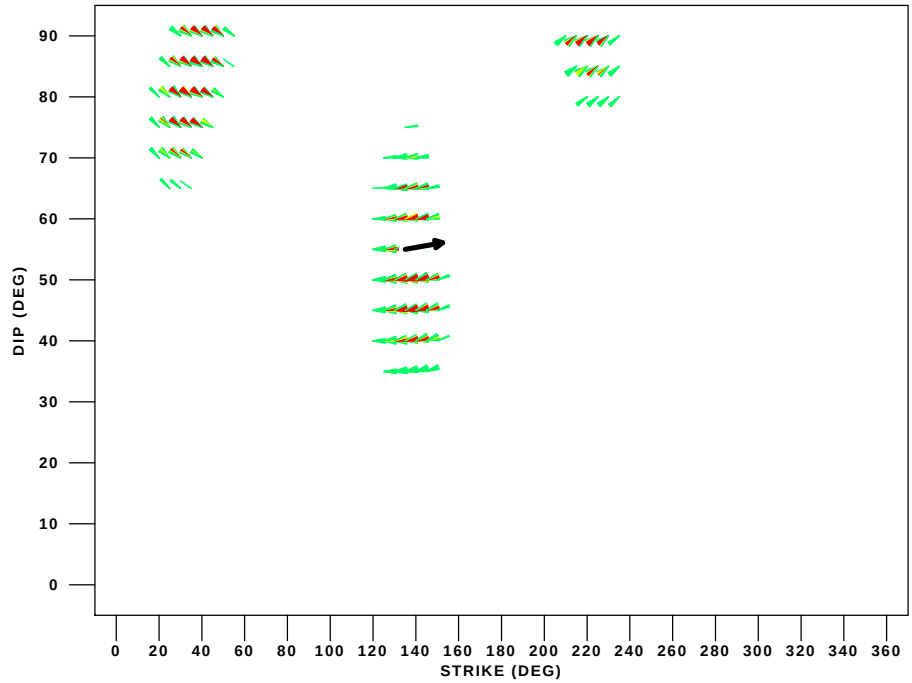

Fig. 3.4a. The result of grid search of event 0647. The arrow shows the focal mechanism (strike=135°, dip=55°, and rake=10°) of the smallest misfit between synthetic and observed P-, SV-, and SH-amplitudes. The angle between arrow and horizontal line (anticlockwise) is rake. The dark, light gray and gray suggests the focal parameters with a 90%, 95% and 99% confidence of F-test, respectively.

3.5 Data processing

The effect of the instrument on the seismogram depends on the instrument transfer function. In a digital system the sensor is either a velocity transducer or a force-balance accelerometer. If a velocity transducer is used, the velocity sensitivity of a seismograph is constant at high frequency. The velocity sensitivity of PANDA system is flat at frequences about 4.5 Hz until 15 Hz where anti-aliasing filters take

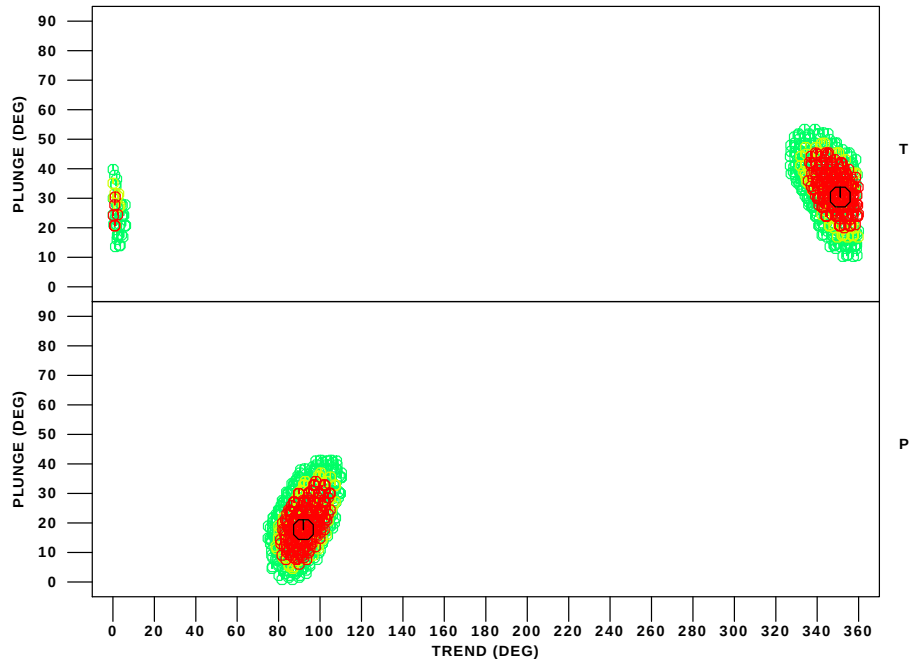

Fig. 3.4b. P- and T- axes of the event 0647 using grid search. The circus shows the best focal parameter. The dark, light gray and gray area are corresponding the 90%, 95%, and 99% confidence of F-test, respectively.

effect. The general transfer function in the Laplace domain of such an instrument is given by

$$H(s) = \frac{s^2}{s^2 + 2\zeta\omega_n s + \omega_n^2} \tag{3.4.1}$$

where ω_n is the natural frequency of the seismometer. ζ show the damping values.

The equivalent recursive expression for this response using the bilinear Z-transform of s can be written as (Saikia and Herrmann, 1985)

$$Y_n = [X_n - 2X_{n-1} + X_{n-2} - b_1 Y_{n-1} - b_2 Y_{n-2}]/b_0 \tag{3.4.2}$$

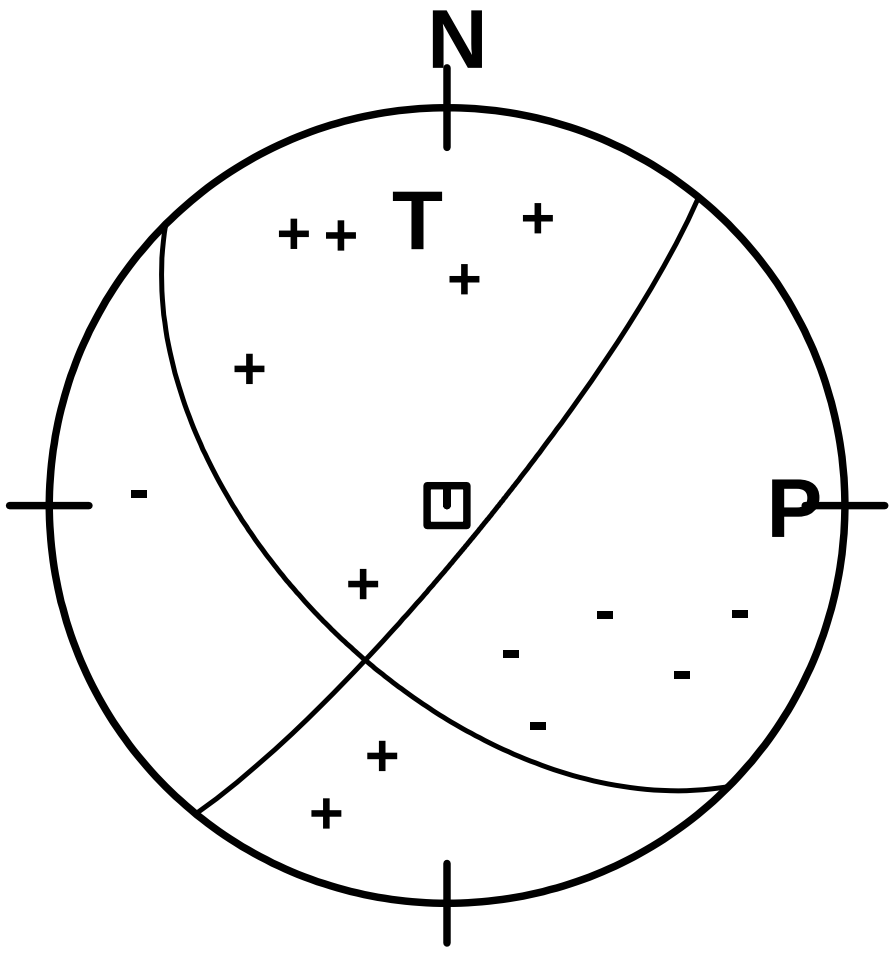

Fig. 3.4c. The smallest misfit focal mechanism of event 0647. Compression qudrad rants was shown by +. The projection is lower hemisphere.

where

$$b_2 = 1 - 2\zeta k_2 + k_2^2$$

$$b_1 = 2k_2^2 - 2$$

$$b_0 = 1 + 2\zeta k_2 + k_2^2$$

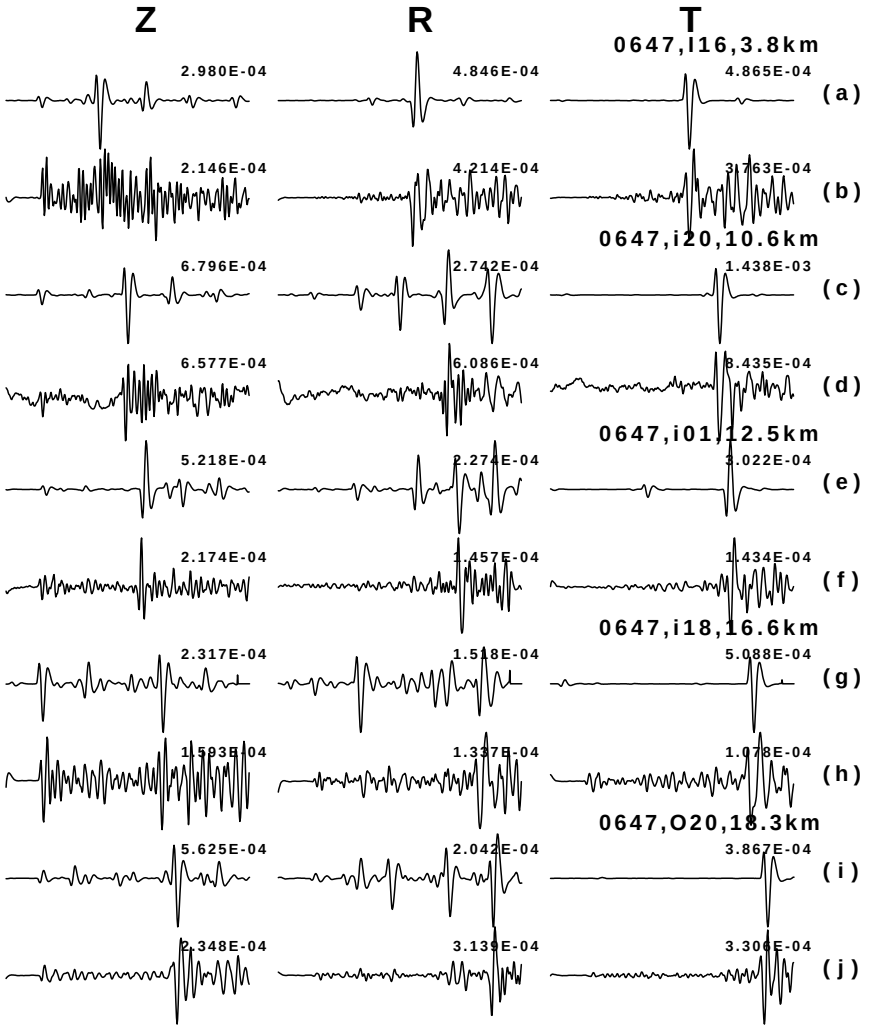

Fig. 3.4d. Comparison between 3-component observed and synthetic velocity seismograms of event 0647 at 5 stations. The length of each time history is 4.25 sec. Synthetic seismograms were obtained by using the corresponding focal parameters in Fig.3.4c, which were obtained from 9 station data. The number by each trace is the maximum velocity value (cm/s). The P-, SV- and SH-, even some converted phases (PS, SP which were not used in the inversion) of synthetic seismograms are consistent with those of observed seismograms.

$$k_2 = \tan(\frac{\omega_n \Delta t}{2})$$

X_i and Y_i are the ground velocities and the recorded voltages, respectively. To avoid problems inherent in removing the instrument response, synthetic seismograms are generated by passing the synthetic ground motion through the instruments. If the instrument is of the FBA type, the recursive filter can be designed by removing the s^2 term from the numerator and replacing it by ω^2.

Three criteria were used for the selections of the events and phases in this study: (1) high signal-to-noise ratio; (2) good station azimuthal coverage; and (3) clear direct P-, SV- and SH- phases recorded by at least 8 stations.

The velocity model (Chiu, *et al*. 1993) and attenuation model (Liu *et al*. 1994) used in this study are shown in Table 3.3. The sediment thickness was adjusted for each station by waveform modeling. Observed data and synthesis were low-pass filtered at 4.5 Hz. Instrument response was added on synthetic seismograms. Parabolic pulses (Herrmann, 1979) with time duration of 0.12 sec. were used as the source time functions. Because of the low-pass filtering this duration is acceptable. In addition it is near to the expected duration of small earthquakes. Cagniard de-Hoop and wavenumber-frequency integration were used for Green's functions. Cagniard de-Hoop technique (Helmberger and Harkrider, 1978) (with assume Q = infinity) was used initially to verify arrival time timing and get preliminaries results. Final inversion used wavenumber-frequency integration (Wang and Herrmann,1980; Herrmann and Wang, 1985) to add the effect of attenuation on waveform and amplitudes. Grid search of P-, SV-, and SH-

amplitudes for all possible values of strike, dip, and rake in 3° increments was used. The smallest misfit and also highest correlation coefficients between observed and synthetic seismograms determine the best focal parameters (3.3.16, 3.3.17).

Table 3.3 Velocity and attenuation model in New Madrid Seismic Zone

V_P (km/s)	V_S (km/s)	Q_P	Q_S	H (km)
1.80	0.60	56	36	0.65
6.02	3.56	1000	1000	1.85
4.83	3.20	675	1000	2.5
6.17	3.57	1000	1000	12.0
6.6	3.8	1000	1000	10.0
7.3	4.2	1000	1000	13.0

The sediment thickness of first layer was adjusted for each station.
Velocity model is from Chiu *et al.* (1992).
Q model is from Liu *et al.* (1994).

Moment tensor inversion (Langston 1981; Saikia and Herrmann, 1986; Jost and Herrmann, 1989) was also used and produced similar results (Table 3.4).

A synthetic test of the method's reliability were generated. For given focal parameters (strike = 120° , dip = 90° and slip = 0° and M_o = 5.667×10^{18}). and Green's functions at nine stations, the synthetic seismograms were produced. Both moment tensor inversion and grid search method were applied to the synthetic data set. The similar results to the given focal mechanism parameters (Table 3.4) indicate the reliability of both techniques for perfect observations.

Table 3.4. Reliability test of method.

Parameter	Input	M	G
strike(°)	120	120	120
dip(°)	90	90	87
slip(°)	0	-0.80	0
$M_0 \times 10^{18}$	5.667	5.659	
CLVD%		0.00016	
P-Corr. Coef.		0.999	0.997
S-Corr. Coef.		0.999	0.998

M - moment tensor inversion.
G - grid search, the search interval is 3° .

CHAPTER 4

EARTHQUAKE SOURCE PARAMETERS AND SEISMOTECTONICS

4.1 Introduction

Current seismicity delineates four major fault segments of the New Madrid Seismic Zone (NMSZ). Seismicity, cross faulting, morphologic and geologic features make the 70 km long central part of the NMSZ a importment segment for study (Figure 4.1). Source parameters are estimated using a grid search inversion. The inversion procedure includes computing Green's function based on well defined velocity (Chiu *et al*. 1993) and attenuation models (Liu *et al*. 1994), a grid search of P-, SV- and SH- amplitudes for all possible values of strike, dip, and rake, at 3° increments. The best fit between observed and synthetic seismograms is used to identify optimal estimates of strike, dip, rake and moment. Application of an F-test permits confidence bounds on the P , T and B axes of the focal mechanisms.

We divided the central NMSZ into three segments of Southeast (SE), central, Northwest (NW) and into southern and northern intersections according to the orientation of seismic pattern and seismicity

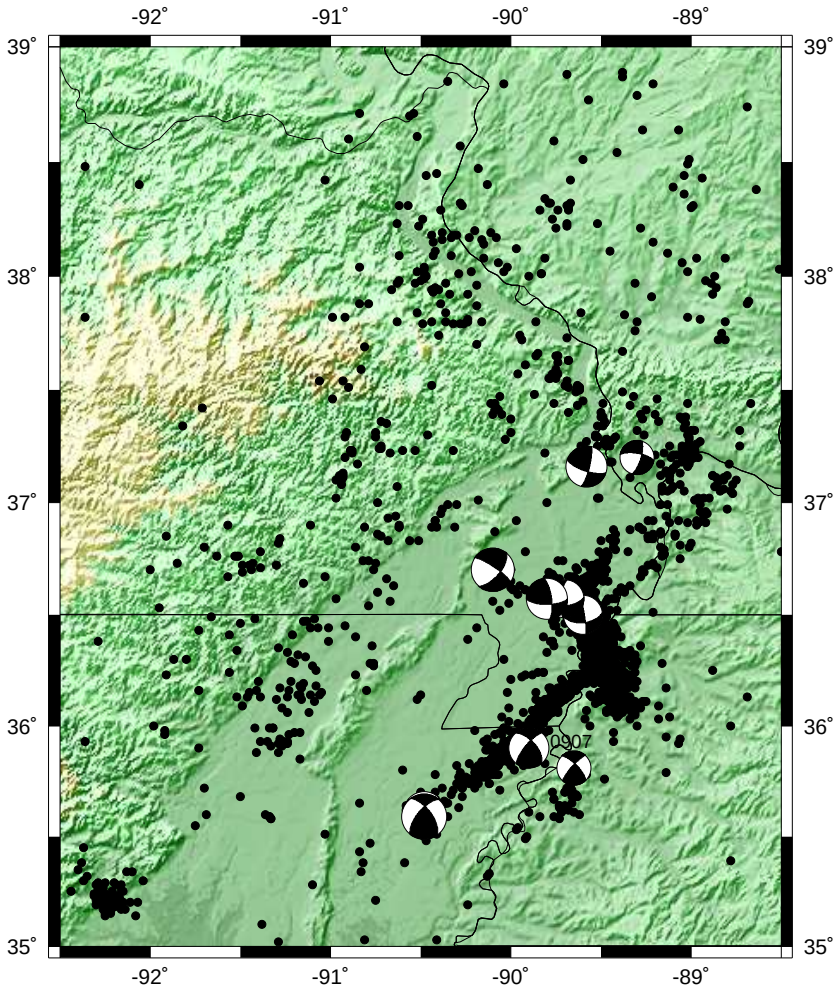

Fig. 4.1. Seismicity (1974-1995) and focal mechanisms of larger earthquakes of the New Madrid Seismic Zone (Herrmann and Canas, 1978; Hermann and Ammon, 1997). 0907 was determined in this study. The four major seismicity patterns and the nature of three of them were defined (Stauder *et al*. 1976; Herrmann *et al*. 1978).

characteristics (Figures 4.2 and 4.3). The focal mechanisms in different segments will be combined with the spatial distribution of the seismicity to obtain a 3-dimensional picture of faulting. Focal mechanisms

Table 4.1. Locations and source parameters of microearthquakes in the central NMSZ

Event ID	Date m/d/y	Origin time hhmmss.	Latitude (° N)	Longitude (° W)	Depth (km)	m_{Lg}	Strike (°)	Dip (°)	Slip (°)	$M_0 \times 10^{18}$ (dyne-cm)
0114	11/05/89	061605.13	36.31	89.51	6.2	2.1	220	65	150	19.89
0139	12/01/89	092651.25	36.21	89.42	9.9	2.7	6	54	75	85.11
0213	12/27/89	152915.96	36.46	89.54	9.1	2.1	189	24	69	6.88
0235	01/05/90	174048.79	36.46	89.54	8.5	2.2	6	42	135	16.94
0308	01/15/90	060335.50	36.24	89.60	4.9	2.2	219	78	-174	24.48
0429	02/03/90	152251.50	36.52	89.54	5.4	2.6	54	39	-174	35.81
0431	02/03/90	174239.22	36.52	89.54	5.3	2.4	51	30	-171	36.51
0435	02/03/90	193747.11	36.52	89.54	5.3	1.8	51	31	-180	8.32
0441	02/05/90	164423.97	36.52	89.52	5.6	2.7	27	33	163	34.03
0521	02/26/90	042135.06	36.27	89.46	5.9	1.9	165	45	102	13.03
0627	04/04/90	164528.85	36.26	89.44	5.8	-	180	57	108	3.40
0647	04/15/90	235734.59	36.27	89.49	8.9	2.7	40	85	140	67.97
0733	05/24/90	110738.23	36.58	89.61	5.0	2.6	186	33	147	64.42
0823	08/15/90	044509.42	36.47	89.54	9.0	2.6	21	51	168	50.10
0826	08/15/90	052752.67	36.47	89.55	9.4	-	210	57	-168	3.74
0830	08/15/90	154812.81	36.47	89.54	9.2	-	21	60	159	8.52
0835	08/19/90	011146.96	36.44	89.53	8.8	2.2	57	36	174	31.38
0907	08/29/90	193459.39	35.81	89.65	12.0	3.8	222	79	-162	
0911	08/29/90	211949.55	36.56	89.65	12.6	2.9	340	45	70	532
0928	09/13/90	083020.94	36.41	89.53	8.3	1.9	210	30	130	7.20
0930	09/13/90	231809.50	36.35	89.52	8.3	2.4	126	69	-18	32.38
1043	10/27/90	063857.90	36.40	89.52	8.0	2.6	120	60	0	35.46
1057	11/09/90	033915.93	36.54	89.62	6.3	3.2	310	80	0	462.17
1101	11/10/90	003825.87	36.27	89.47	6.1	1.9	192	30	120	8.5
1103	11/10/90	031816.23	36.13	89.41	10.5	1.5	355	60	65	11.18
1109	11/15/90	115358.12	36.27	89.47	6.0	-	162	33	105	4.43
1121	11/20/90	055438.60	36.27	89.47	6.1	-	207	27	144	8.23
1122	11/21/90	160717.76	36.27	89.47	7.2	2.7	168	42	111	61.97
1130	11/24/90	112407.27	36.26	89.49	8.2	-	231	60	177	1.45
1142	11/30/90	000104.78	36.30	89.48	5.1	1.9	333	12	-126	33.35
1212	12/15/90	154340.14	36.21	89.46	9.0	2.1	6	66	108	38.59
1309	02/26/91	201424.86	36.19	89.51	5.8	2.3	138	39	39	35.62
1311	02/26/91	203701.58	36.19	89.51	5.9	2.1	135	39	39	43.77
1327	03/14/91	131710.32	36.27	89.47	6.2	1.8	360	45	90	22.20
1335	03/19/91	192148.66	36.44	89.53	8.8	3.5	204	69	108	97.21
1408	05/04/91	011854.97	36.56	89.80	6.89	4.6	90	68	20	12900
1446	05/24/91	041444.84	36.34	89.51	9.1	-	181	41	106	8.50
1452	05/28/91	085829.81	36.27	89.48	7.3	1.9	12	30	144	0.85
1507	06/01/91	220141.21	36.52	89.59	11.4	2.7	111	54	3	51.70
1518	06/09/91	092459.22	36.27	89.46	6.1	-	181	39	100	7.54
1529	06/20/91	120611.40	36.31	89.46	5.0	2.4	10	75	-120	66.50
1548	06/26/91	105238.78	36.57	89.59	10.21	2.6	99	63	-3	33.00
1617	07/08/91	234907.31	36.15	89.45	11.8	3.1	330	40	100	13.17
1633	07/23/91	050647.04	36.21	89.45	9.4	2.1	129	81	9	19.78
1639	07/26/91	163622.12	36.24	89.51	8.2	1.7	210	36	156	7.57
1839	09/25/91	021354.49	36.48	89.55	8.0	2.2	51	48	144	11.52
1844	09/27/91	214229.26	36.45	89.62	11.9	2.1	303	72	32	10.41
1911	10/24/91	064710.91	36.39	89.54	9.0	2.5	207	51	-117	33.35
1939	10/29/91	222524.83	36.41	89.50	7.4	2.0	256	53	-154	13.60
2217	12/02/91	041455.62	36.43	89.52	7.9	1.5	93	39	6	25.49
2220	12/04/91	002147.49	36.49	89.50	4.9	2.0	93	81	-9	17.66
2225	12/06/91	233127.32	36.55	89.68	4.8	-	231	84	-117	3.75
2235	12/11/91	081534.18	36.42	89.50	7.1	-	250	70	-150	2.90
2250	12/16/91	004225.87	36.47	89.52	9.0	-	321	75	69	6.61
0001	06/13/75	2240	36.54	89.68	9	4.5	85	60	-20	4600
0002	03/03/63	1730	36.64	90.05	15	4.2	304	78	-28	110000
0003	11/17/70	0213	35.86	89.95	16	5.0	220	65	150	16000
0004	03/25/76	0041	35.59	90.48	12	4.4	220	74	149	98000

0001-0004 from Herrmann and Ammon (1997);
1101,1452 obtained using genray85;
0907 obtained from 45 P-first motion data.

of 54 microearthquakes (m_{Lg} = 1.5 - 4.6) located in the central NMSZ

were obtained using three-component PANDA data and waveform modeling and are listed in Table 4.1. The spatial distribution of hypocenters was obtained using a Joint Hypocentral Determination (JHD) method (Pujol, 1996).

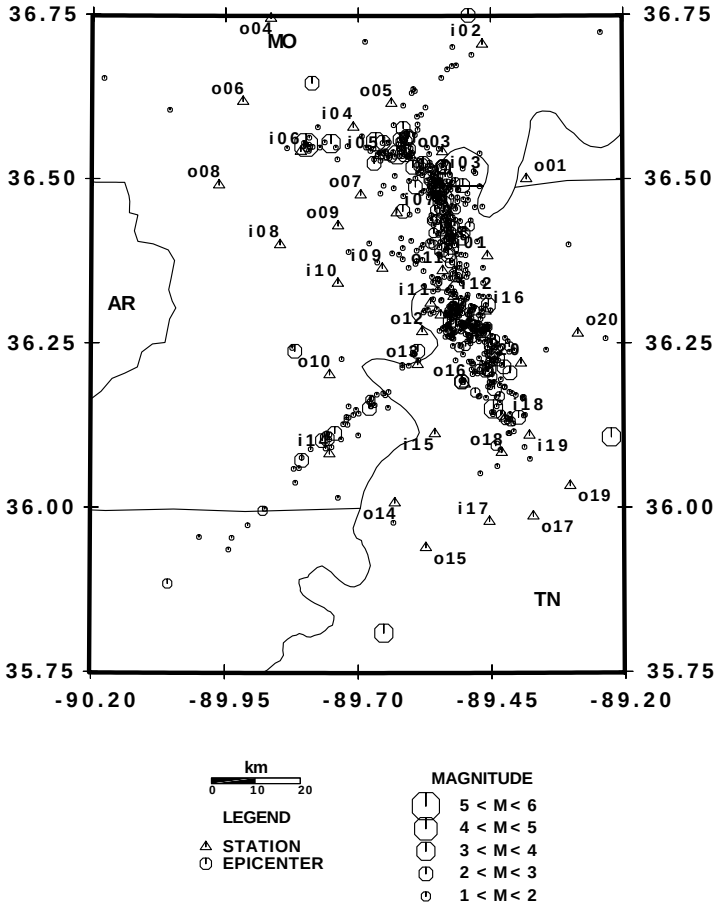

Fig. 4.2. PANDA locations and seismicity of the NMSZ during the period of Oct. 1989 - Dec. 1992 determined by CERI.

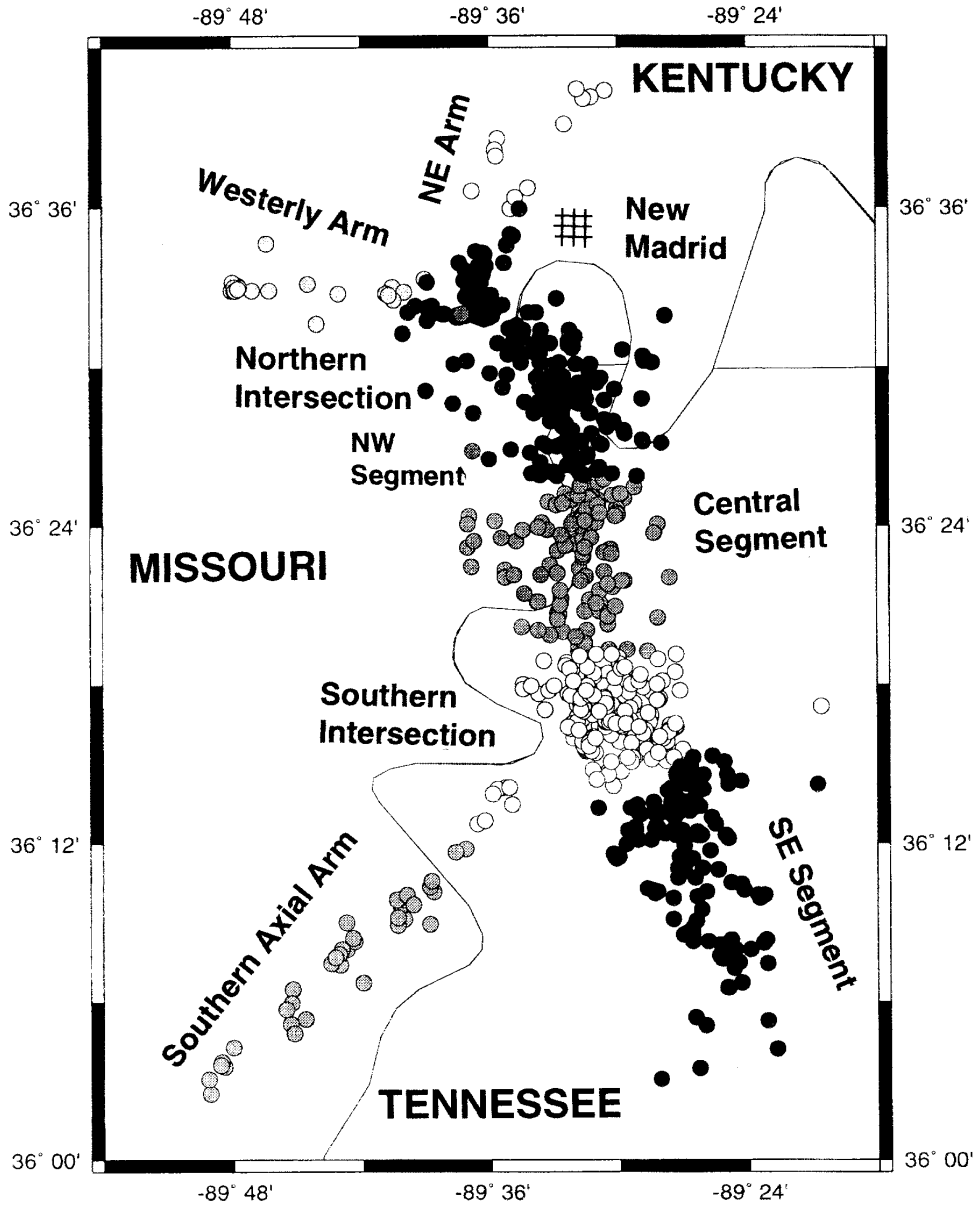

Fig. 4.3. JHD hypocenters of the central NMSZ. The relationship between focal mechanisms and JHD hypocenters will be studied in the 7 parts: SE segment, southern intersection, central segment, NW segment, westerly arm, N-E arm, and southern axial arm.

4.2 Focal mechanisms of the central NMSZ

4.2.1 Microearthquake distribution with depth

Event relocation using PANDA data and the JHD method by Pujol (1995) suggested that most seismic foci are concentrated between 4 and 12 km depth. In Figure 4.4 we show the seismicity distribution with depth. It indicates a seismic surface that dips to W or SW. The gradient of the change of focal depth implies steeper structure plane in the SE and NW segments of the central seismicity segment. The shallowest (4-5 Km depth) hypocenters are located on the east edge of the central NMSZ and are parallel to the Reelfoot scarp and its northwestern extension (Kentucky Bend). Figure 4.4 shows shallow seismicity in linear zones striking NE and parallel to the southern axial arm. A clear gap (Ridgely Gap) of earthquakes can be found just in the southern side of Ridgely. Figure 4.4 also suggests that the southern axial arm, westernly arm and NE arm (Figure 4.2) are the narrow and vertical seismic zones.

4.2.2 Focal mechanisms and active faulting

(1) SE segment

This segment extents from Ridgely to the southern end of the central NMSZ. In Figure 4.5a we show the seven focal mechanisms

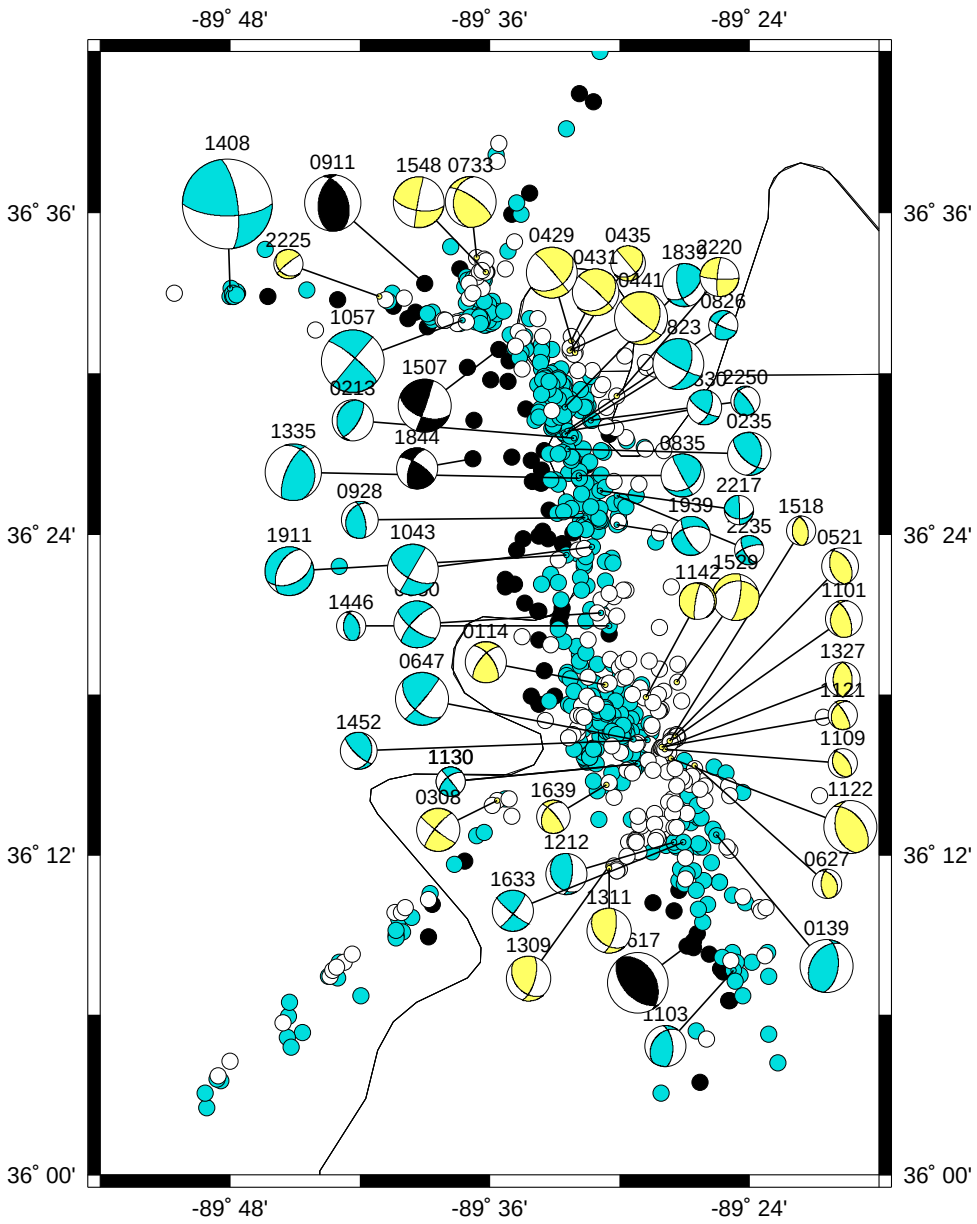

Fig. 4.4. The depth distribution of hypocenters: white : 4-7 km, gray: 7-10 km, black: 10-12 km and 54 focal mechanisms. The distribution of the shallow earthquakes is along the east boundary of the NMSZ, also the shallow events show some NE striking zone parallel to the SW axial seismic arm. Focal mechanism color and size indicate the focal depth and magnitude (m_{Lg} = 1.5-4.6). Dilatation quadrants are shown by white; the projection is lower hemisphere. Note the different styles of faulting in different segments of the central NMSZ.

determined in the SE segment. Figure 4.5b shows the map view of the microearthquake locations and focal mechanisms in the NMSZ. The cross section of the hypocenters of the SE segment onto a vertical plane perpendicular to the N30°W and also the focal mechanism projected onto this plane are shown in Figure 4.5c. The cross section indicates two conjugate fault zones, one striking N30°W and dipping 45°SW is clearly the principal fault zone. The focal mechanism of larger event 1617 (m_{Lg}=3.1) suggests a pure thrust motion on strike 330° and dipping 40°SW nodal plane. The consistency of orientation between the principal fault and the NW striking and SW dipping nodal plane suggests that the principle fault is a pure reverse fault striking N30°W and dipping 45°SW. The conjugate zone is a boundary fault of the SE segment and also the Ridgely gap. This zone is underlain the southern end of Ridgely Ridge (Figure 1, Russ, 1982; Nicholson and Simpson, 1984). It strikes NE, steeply dips SE, and parallels to the southern axial seismicity arm (Figure 4.5b). Figure 4.4 clearly identify the shallow NE-striking boundary fault steeply dipping SE. A series of earthquakes with magnitudes m_{Lg} >2 occurred on the zone (0139, 1309, 1311, 1212, 1633). The mechanism of 1633 indicates a right-lateral strike-slip motion occurred on a vertical nodal plane striking NE and parallel to the conjugate zone. The focal mechanisms of the other four events are well constrained. It may be interpreted either as a right-lateral oblique reverse motion on a striking NNE-NE and high-angle dipping ~60-70°SE or a thrust faulting on a NW striking and ~40°SW dipping nodal plane. The first nodal plane is parallel to the NE conjugate structure. It is the most likely fault plane.

Therefore the NE striking and dipping ~60-70°SE conjugate fault is a right-lateral oblique reverse fault.

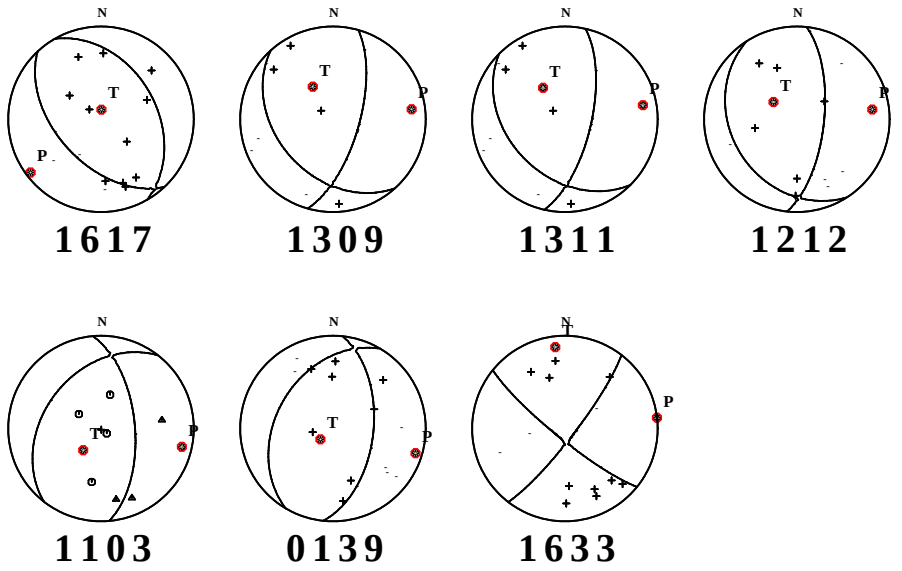

Fig. 4.5a. Focal mechanisms of 7 events at SE segment of the central NMSZ determined using waveform modeling.

(2) Southern intersection

The southern intersection of the central NMSZ with the southern arm is located in the Ridgely area. The seismicity pattern strikes NW. Most events are shallower than 10 km. Small swarms concentrated here (Xie *et al*. 1997). There were no earthquakes with $m_{Lg} \geq 3$ in the last 30 years. The focal mechanisms of 17 microearthquakes were estimated in this region. The focal mechanisms predominantly show strike-slip or thrust motions with horizontal east-west trending P-axis (Figure 4.6a,b). The cross section and vertical projection of the focal mechanisms are shown in Figure 4.6c. This cross section indicates a

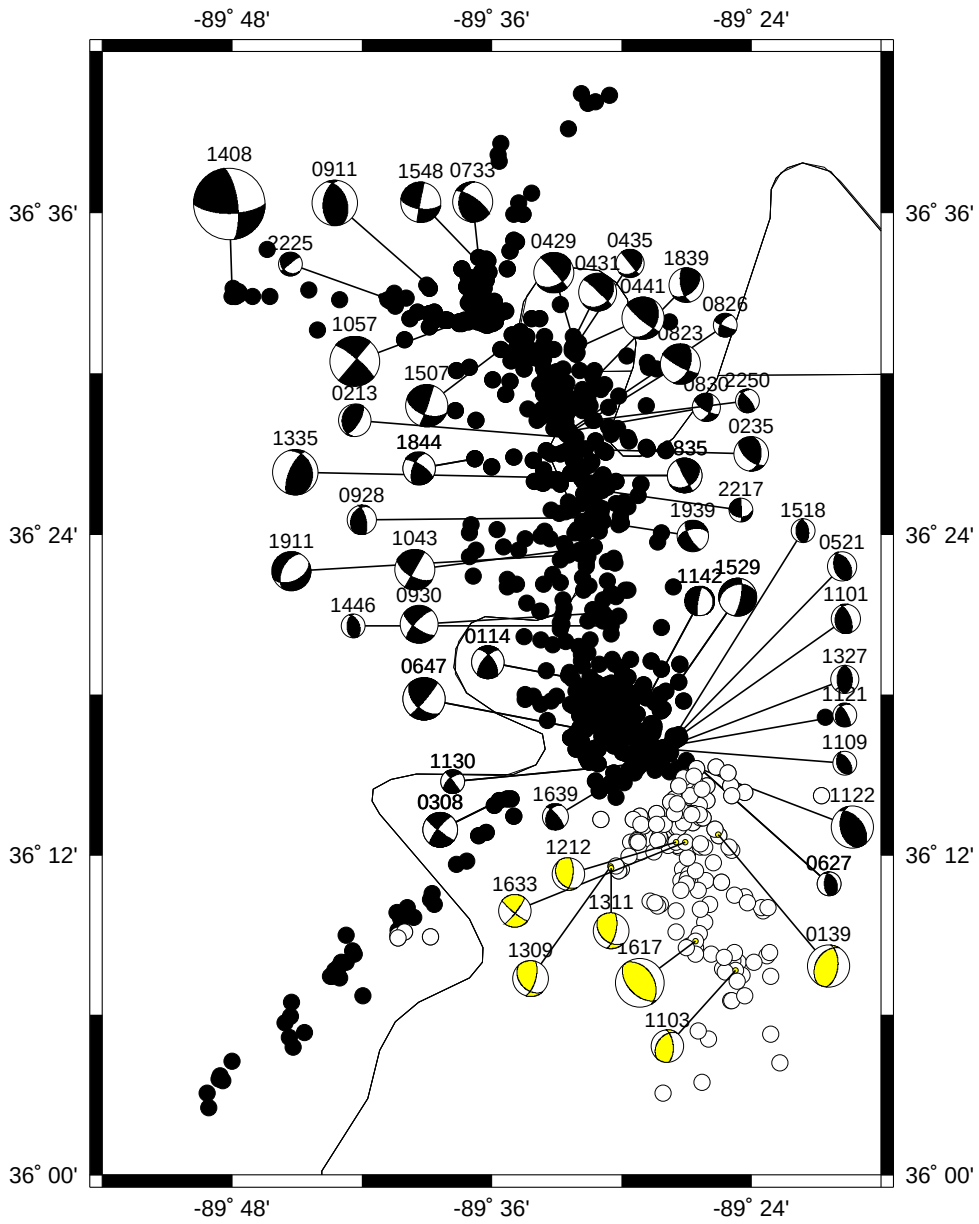

Fig. 4.5b. Focal mechanisms and hypocenters of the central NMSZ, the SE segment (white), will be discussed in detail in Figure 4.5c.

structural plane striking NNW and dipping ~40° SW, which is consistent with the nodal planes striking N-NNW and dipping ~40° SW of the reverse focal mechanisms of clusters 1122, 1101, 1109, 1518, 0521, and events 1639, 1327 and 0627. Therefore the definition of the

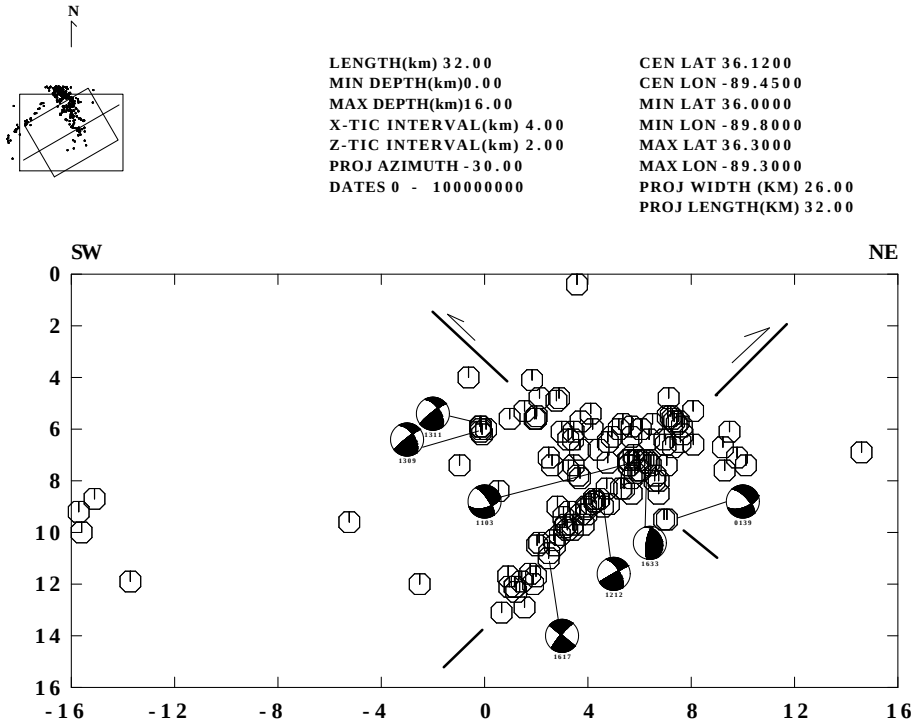

Fig. 4.5c. Cross section of earthquake hypocenters with strike N30°W and projection of the focal mechanisms onto a vertical plane. This picture clearly defines two conjugate faults. One striking N30°W and dipping 45°SW is a principal structure, which is a reverse fault. The other strikes NE and dips SE, which is a right-lateral oblique reverse fault. Upper left corner shows a surface view of projected area and all events which will be projected to the central line. All projection information is on the upper caption.

central NMSZ in the Ridgely area as a thrust fault striking NW and dipping 40°SW is reasonable. The azimuthal variations in source duration, which were obtained from empirical Green's function analysis, also suggest that the rupture directions are toward the NNW (Xie *et al*. 1997) (Figure 4.6d). Figure 4.6c suggests that the most activity occurred on the hanging wall of the reverse fault.

The map view of the earthquake locations (Figure 4.6b) shows three shallow earthquake zones striking NE and parallel to the southern rift axial arm. The events of 0930, 0114, and 0647, 1639, 1130 are located on the small zones. The focal mechanisms of these events indicate similar right-lateral strike-slip faulting on a vertical plane NE striking in responsible with the east-west compression. These right-lateral strike-slip movement on striking NE vertical fault plane are similar to that of event 0308, which is on the southern axial seismicity arm. These NE trending zones with right-lateral strike-slip motions may be as either a NE extensions of the axial arm or its secondary faults (Gomberg, 1993).

In Figure 4.7a we show the events in the southern intersection of southwest arm with central NMSZ and in Figure 4.7b we show a cross section which is perpendicular to the NE striking arm and indicates that the axial arm is vertical with width of about 8 km, located between 4 and 12 km depth. Figure 4.7b clearly delineates a cross faulting system: the longer, narrow and vertical right-lateral strike-slip southern axial arm terminates in the hanging wall of the central NMSZ dipping SW thrust fault. All earthquakes with right-lateral strike-slip located on the hanging wall and other earthquakes with thrust focal mechanism located on the dipping SW fault plane.

Some shallow events occurred on the east boundary of the central NMSZ in the Ridgely area. The mechanism of 1142 (Figure 4.6b) exhibits a high-angle, NNE striking nodal plane and a nearly horizontal nodal plane which may dip either east or west. Since there is no

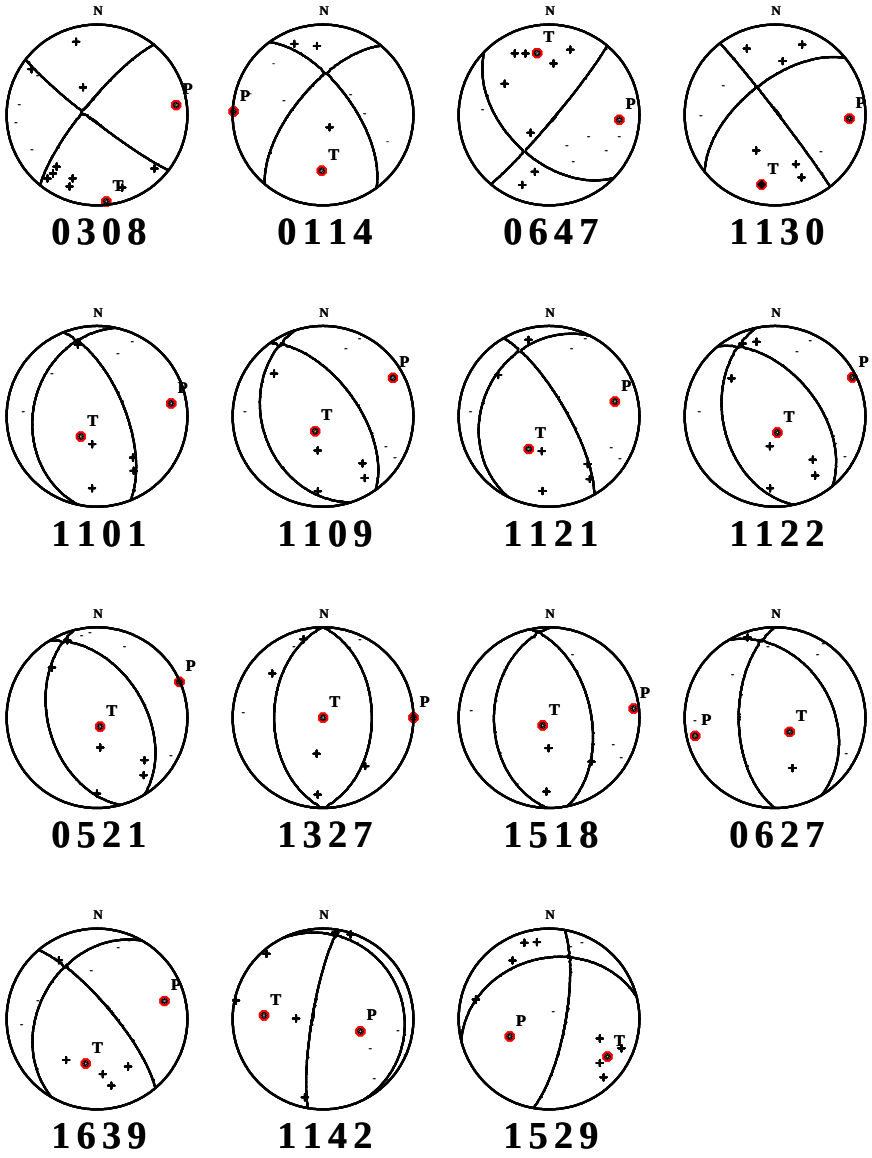

Fig. 4.6a. Focal mechanisms of 15 events at the southern intersection. Two major styles of strike-slip and reverse faulting are shown. The mechanism of 0308 indicates a typical right-lateral strike-slip faulting at SW axial arm. See caption of Figure 4.5a.

evidence for horizontal faulting in this area, we assumed that this mechanism represents a north trending, nearly vertical, dip-slip fault.

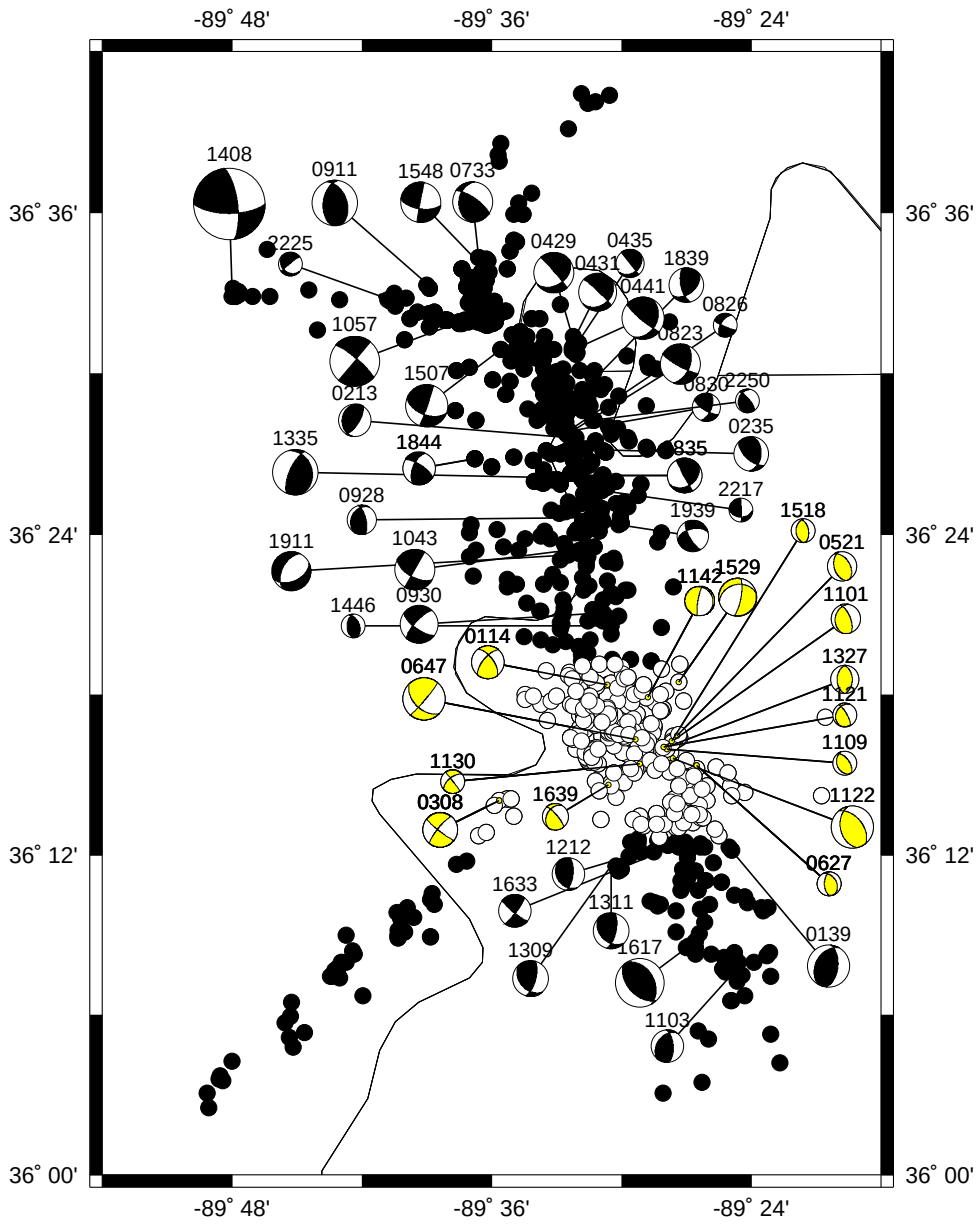

Fig. 4.6b. The focal mechanisms and hypocenters of the central NMSZ, southern intersection (white), will be discussed in detail in Figure 4.6(c).

Another event with a normal faulting component, 1529, shows a near vertical, NNE striking nodal plane and another striking NEE and NNW dipping nodal plane. If we select the vertical nodal plane of

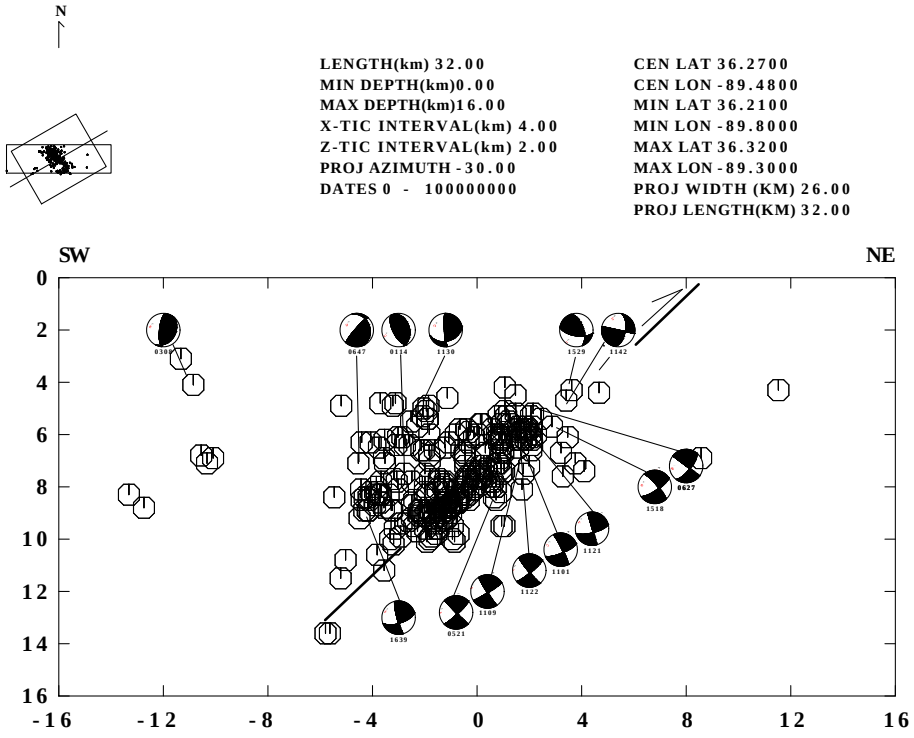

Fig. 4.6c. Cross section of earthquake hypocenters with strike N30°W and the vertical plane focal mechanism projections of 15 events at southern intersection. Most of the activity occurred on or above a plane striking NNW and dipping ~40°SW, which defines a thrust faulting, most strike-slip motion occurred on the hanging wall of the thrust fault.

mechanism of 1529 as a fault plane, it indicates east side down and that of 1142 indicates west side down (Figure. 4.6b). The two events occurred just beneath the Ridgely Ridge (Russ, 1982) and may define the SE and NW boundary of the Ridgely Ridge. Zoback *et al.*, (1980) found a series of subparallel normal faults oriented to the northeast at depth < 1.5 km under the Ridgely Ridge by seismic reflection. Nicholson *et al*. (1984) also observed some shallow normal faulting occurred on hanging wall of a thrust fault striking NE and dipping SW. These

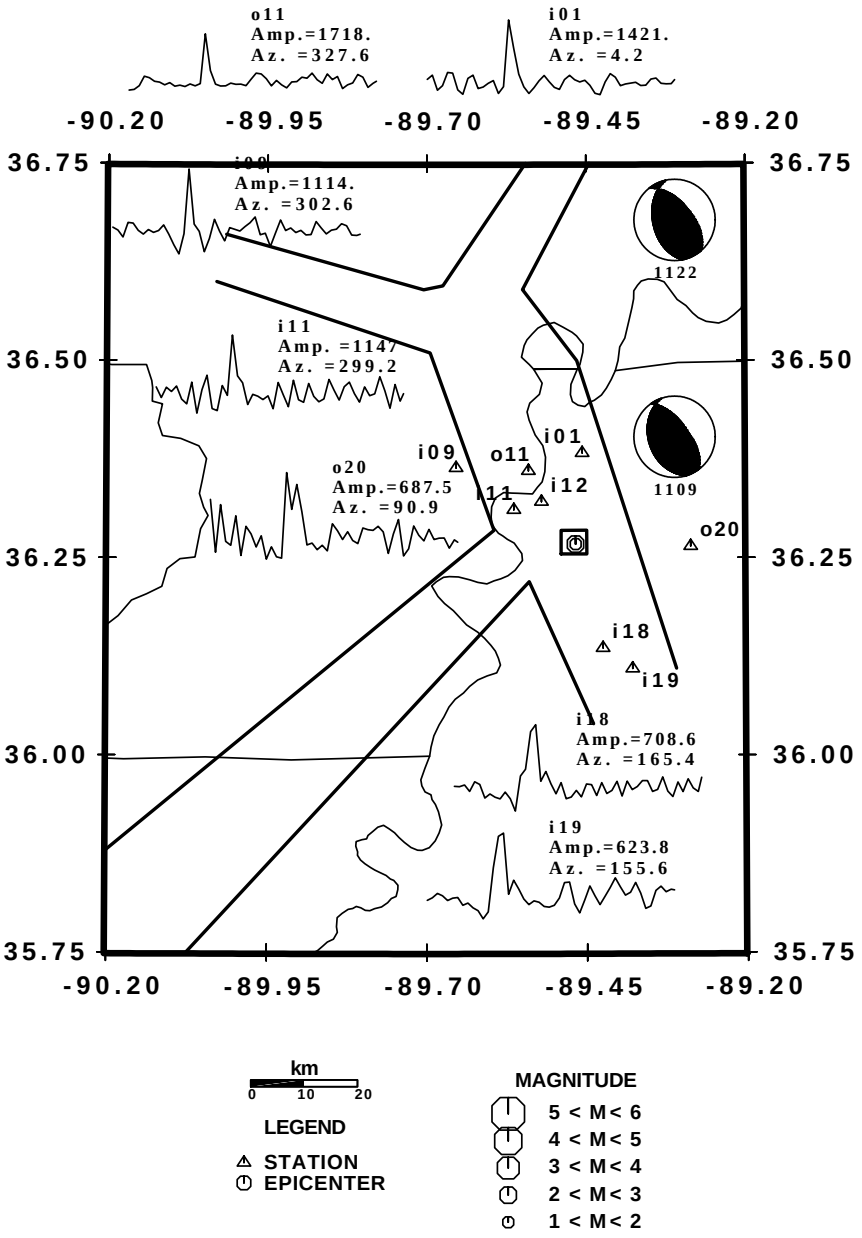

Fig. 4.6d. Azimuthal variations in source duration from empirical Green's function method (data from Xie *et al*, 1997). Note the narrow source duration (i01, o11, i09) and the higher amplitudes in N-NNW direction and wider width (i18, i19) in South. This indicates the direction of the rupture is toward the northwest.

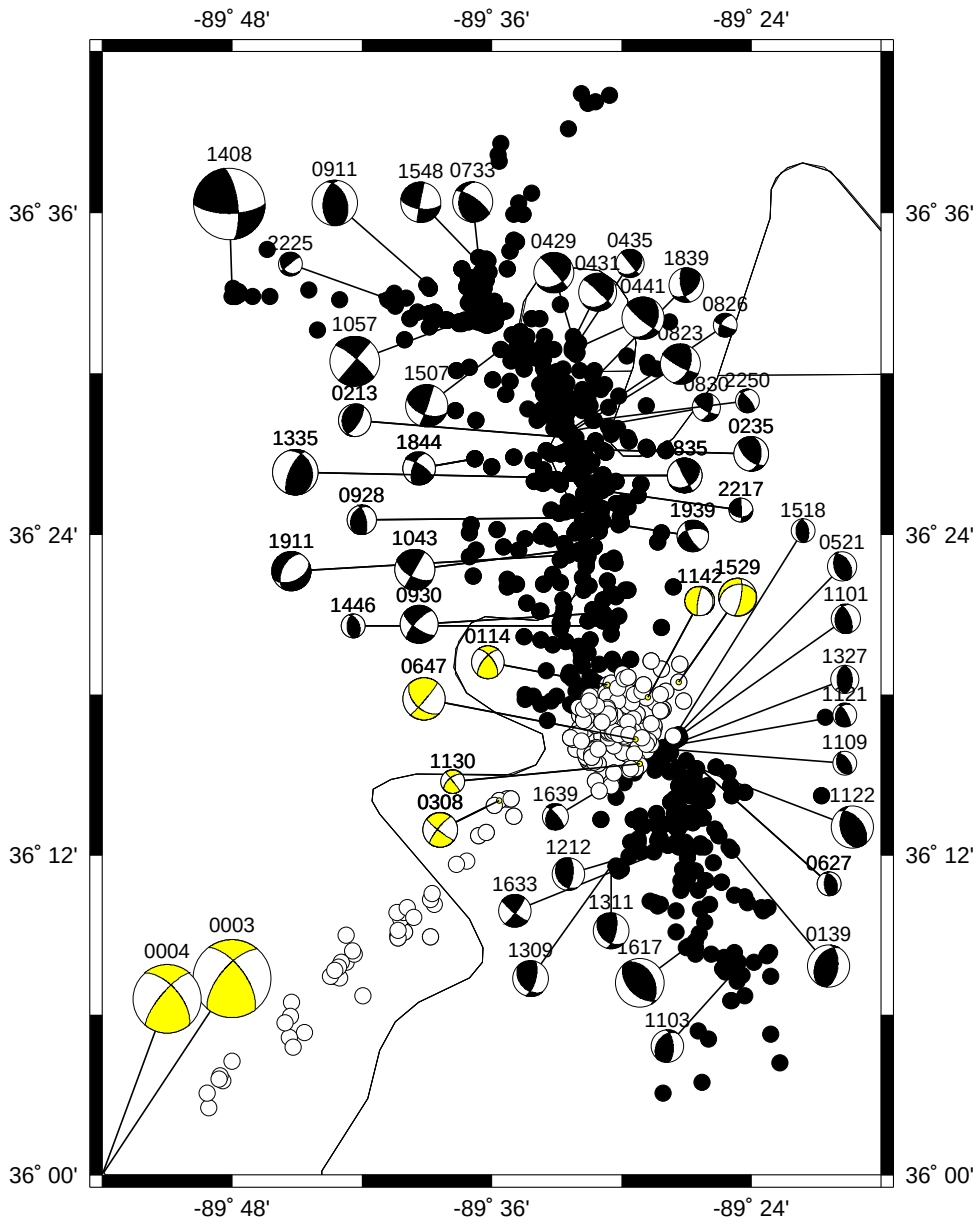

Fig. 4.7a. The focal mechanisms and hypocenters of the central NMSZ, SW axial arm (white), will be discussed in detail in Figure 4.7(b).

observations support the idea that Ridgely Ridge is related the two cross faulting systems of the southern axial arm and the central segment.

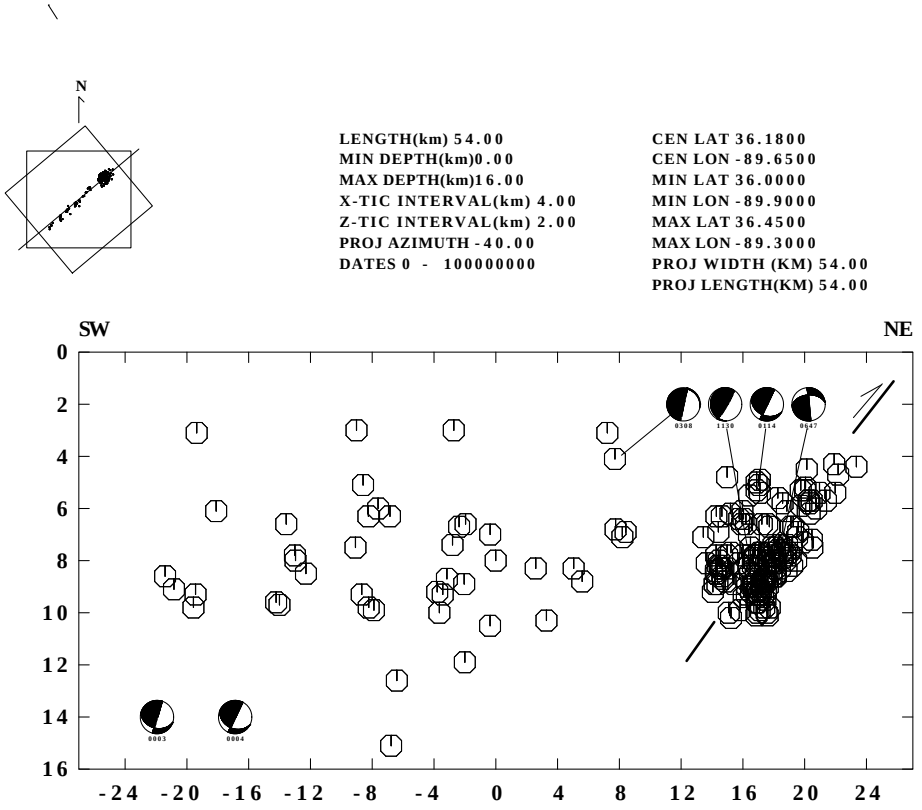

Fig. 4.7b. Cross projection along central line of SW axial arm (N30°W) indicates a vertical fault with width ~ 8 km and depth 2-10 km. Focal mechanisms for 0308, 1130, 0114, 0647, 0003, and 0004 show the vertical nodal planes, which supports concluding that the axial arm is a right-lateral strike-slip fault.

(3) The Central Segment

Microearthquakes occur beneath Mississippi River in the central segment and the pattern strikes NS (Figures 4.8a, 4.8b). Figure 4.4 indicates that the seismicity planes in the central segment dips to W less steeply than the SE and NW segments. An Eastwest cross section (Figure 4.8c), clearly illustrates a structure plane with a NS strike, dipping 35°W. The focal mechanisms of 0928, 1446, 0213, 1335

indicate a nodal plane striking ~NS and dipping average 35°W, which suggests the major structure is a thrust fault.

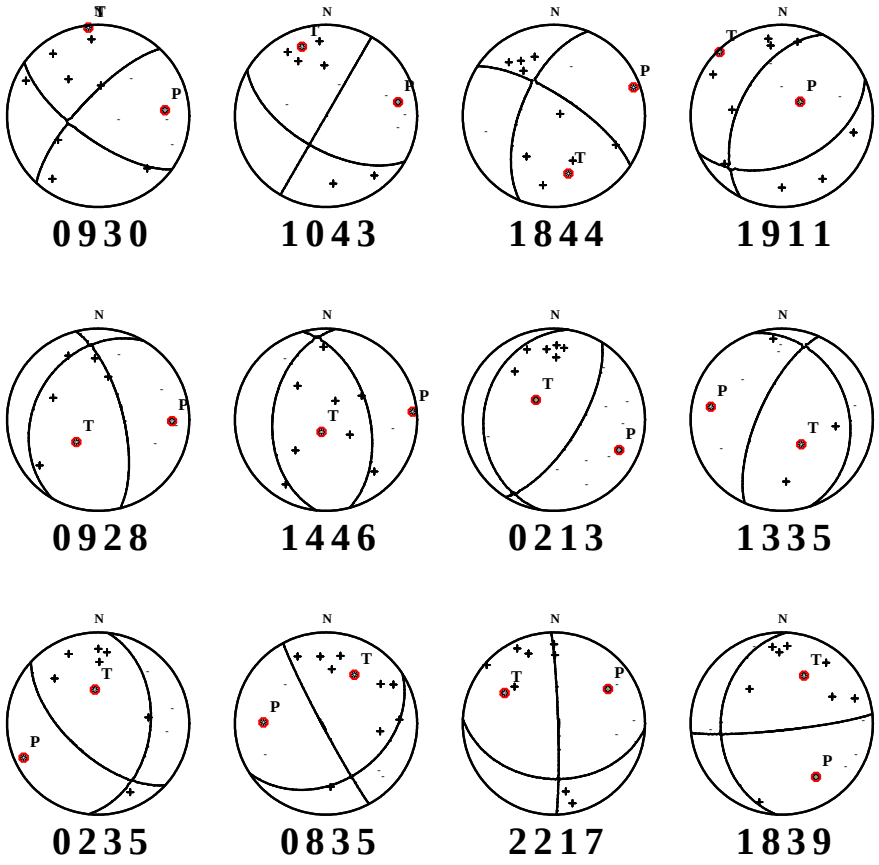

Fig. 4.8a. The focal mechanisms and hypocenters of the central NMSZ. The central segment (black) will be discussed in detail in Figure 4.8c.

A mixed focal mechanisms and lack of agreement between the nodal planes and the seismicity pattern were observed in the central segment. The mechanism of 1911 is normal faulting and has a nodal plane striking NE, which parallels the axial arm, and shows minor right-lateral component, this is a possible fault plane. The

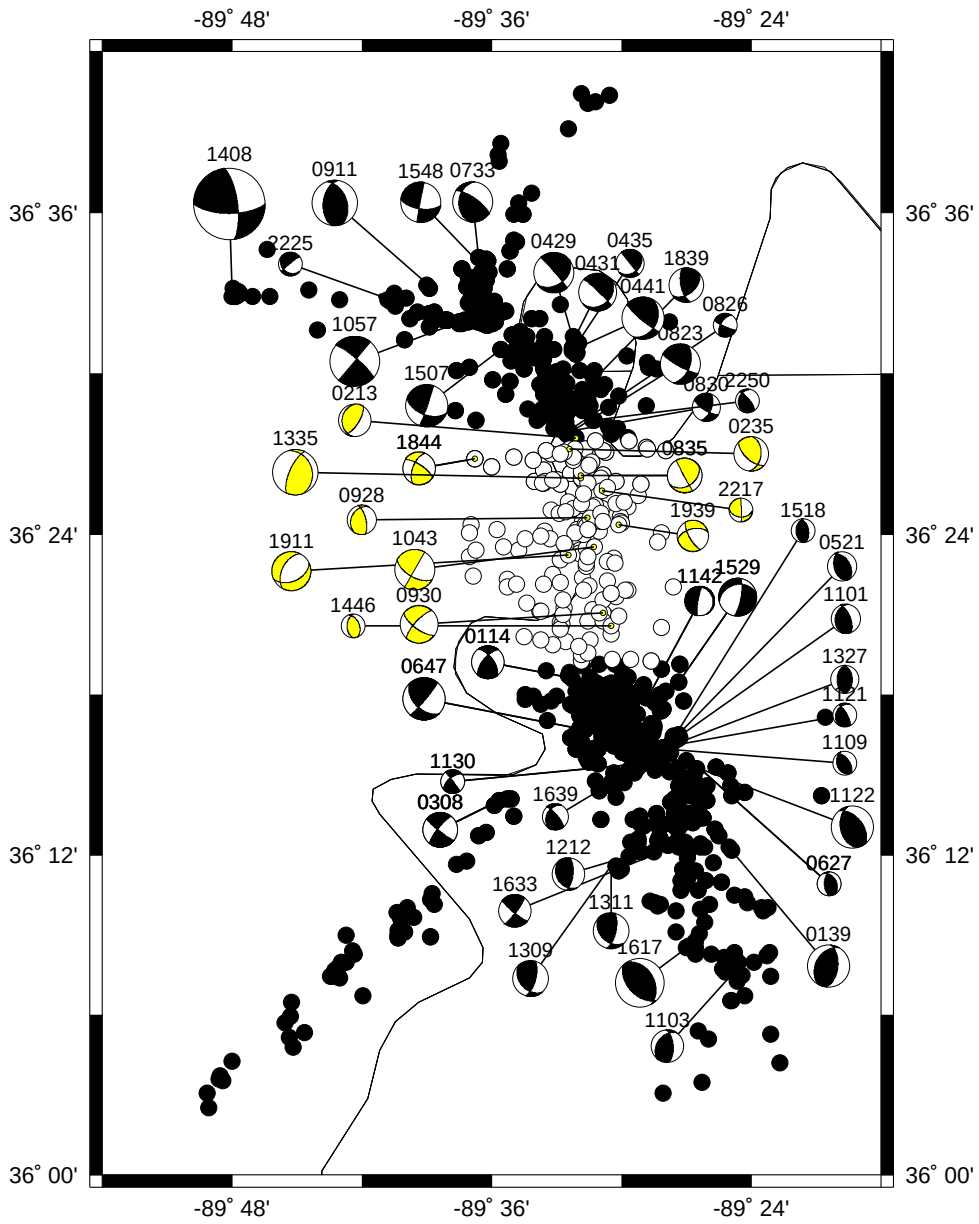

Fig. 4.8b. Focal mechanisms at the central segment (white)of NMSZ. Complex focal mechanisms are observed. The mechanisms of 0928, 1446, 0213, 1335 and 0235 suggest the central segment is a major thrust fault. The strike-slip motions may reflect interaction with nearby seismic faults (see text).

mechanisms of 0930, 1844, and 1043 may be interpreted as either a right-lateral strike-slip fault, that is parallel to the southern axial

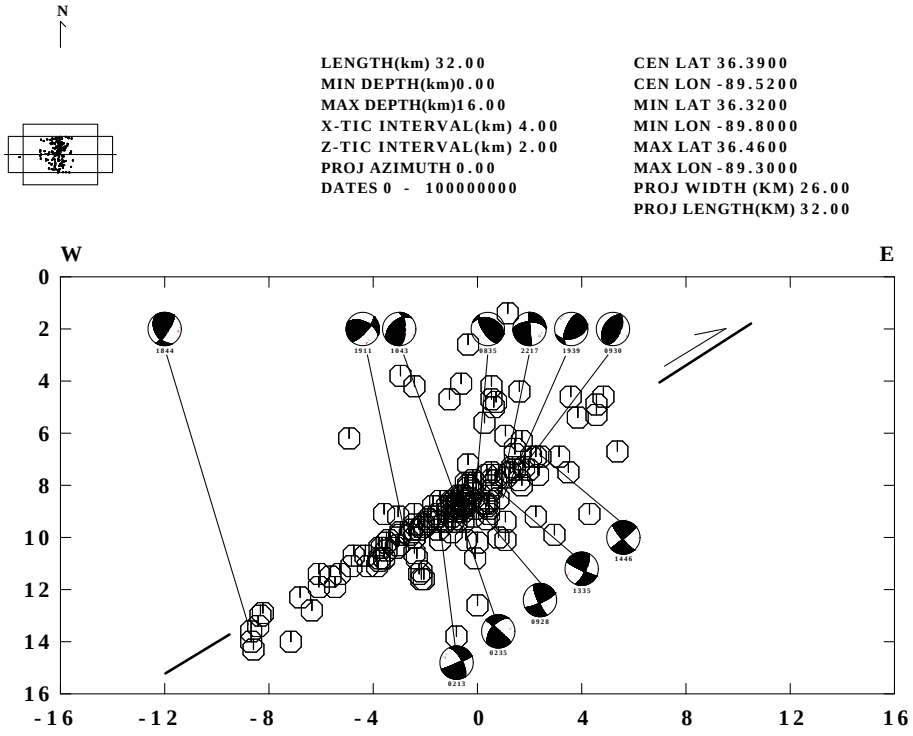

Fig. 4.8c. Cross section of earthquake hypocenters with strike North in the area between Northern and southern intersections. A structure striking north and dipping 35°W was defined clearly. The projection of the focal mechanism onto the vertical plane of 1446, 1335, 0928, 0235 and 0213 suggest the structure is thrust fault. The lack of agreement between the nodal plane and the seismicity pattern are also observed. This indicates the strong effect of neighboring faults.

arm, or a left-lateral strike-slip fault. The P-axes are horizontal and are oriented approximately east-west. Based on the P-axis trending and NE seismicity pattern, we selected the vertical NE nodal plane as the fault plane. Therefore 0911, 0930, 1043 and 1844 are related to the southern axial arm. A rapid shift in focal mechanisms from the northern side of the event 1043 occurs. The focal mechanisms of events 0235, 0835, 2235 and 1939 have a near vertical nodal plane.

The left-lateral strike-slip movement occurred on the nodal plane. The P-axes trend NE-SW. These nodal planes are parallel to the nearby NW segment, which is a left-lateral oblique reverse fault. Therefore the selection of the NW nodal plane as the fault plane is reasonable. The mechanism of 2217 has a NE trending P-axis and indicates a dip-slip motion on a vertical plane. The mixed focal mechanisms suggest that 1) the occurrence of these earthquakes in the central segment are effected by the neighboring faulting; and/or 2) the earthquakes occur on pre-existing weaknesses in the structure.

(4) The NW Segment

The NW segment lies between the kink and northern intersection and locates south of New Madrid (Figure 4.2). The trend in seismicity changes from North to North-West at the Mississippi River. The cross section of the hypocenters indicates the NW segment is a listric fault with a strike N40°W and a dip 70°SW near the surface (depth < 10 km) and 35°SW at depth > 10 km (Figure 4.9b, 4.9c). The focal mechanisms of 13 events were determined including 2 swarms (0429, 0431, 0435, 0441, m_{Lg}=2.8, depth =~5 km and 0823, 0826, 0830, m_{Lg}=2.6 and depth=~9 km, respectively), and 2220, 1839, 1507 (Figure 4.9a). The mechanisms of 13 events indicate a average NE compression and have similar vertical nodal planes striking NW-NWW, on which the left-lateral motion occurs. These nodal planes are parallel to the NW striking vertical listric fault at depth <9 km. The mechanism of 2250 (depth = 9 km) has a NE trending P-axis and shows reverse motion occurring on a NW striking near vertical nodal plane. The event of

1507 (m_{Lg} = 2.7, depth = 11.4) occurred at the deep depth of the listric fault. Its focal mechanism may be interpreted as either a right-lateral movement on a striking NE and near vertical plane or a left-lateral oblique-reverse movement on another nodal plane striking NW and dipping 54° SW. The focal mechanism of 1507 shows a NE trending P-axis (N70°E). Based on the location of 1507 and orientation of the NW low-angle nodal plane, which parallels the trend of the listric fault, this nodal plane is the most likely fault plane. These focal mechanisms at different depths support a listric fault that is a left-lateral oblique reverse fault.

A P- and SH-wave seismic reflection investigation of the Kentucky Bend Scarp (KBS) in the NMSZ found that a N30°W striking vertical reverse fault, which is the northern extension of the Reelfoot scarp. This shallow vertical reverse fault (Woolery *et al*., 1993, 1996) may be the upward extension of the NW listric fault dipping ~70° and the KBS may be its surface expression.

(5) Northern Intersection

The northern end of the central NMSZ is a intersection of the NW segment of the central NMSZ with the right-lateral strike-slip NE arm near New Madrid and the left-lateral strike-slip westerly arm (Herrmann and Canas, 1978; Herrmann and Ammon, 1997). The focal mechanisms of this area are somewhat complex. First, the mechanisms of the largest event 1408 (m_{Lg}=4.6) and 1548, 0743 (both m_{Lg}=2.6, Figure 4.10a) as well as the historical events (m_{Lg}>4.5, 03/03/63, (001) and 06/13/75, (003), Table 1) have similar horizontal N-

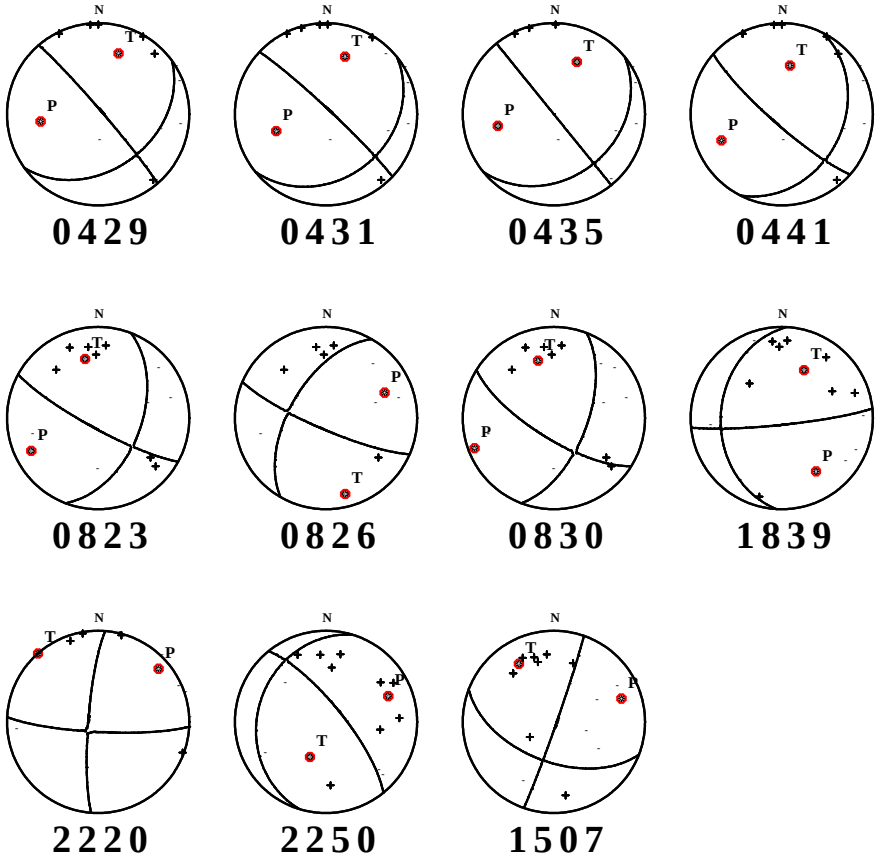

Fig. 4.9a. Focal mechanisms at the NW segment. Note the horizontal NE trending P-axis and the major vertical nodal planes striking NW with left-lateral strike-slip motion, which parallel the seismic pattern.

E trending compressional P-axes, and indicate a left-lateral strike-slip faulting on a vertical fault plan striking NW or NWW in response the NE compression and the NW-NWW seismicity pattern orientation (Herrmann and Ammon, 1997). The mechanisms of 0743 and 1548 may also be explained by extension of the NW segment. The vertical cross projection (Figure 4.10b) along the westerly arm and the back-projection of the focal mechanisms indicate a vertical plane striking

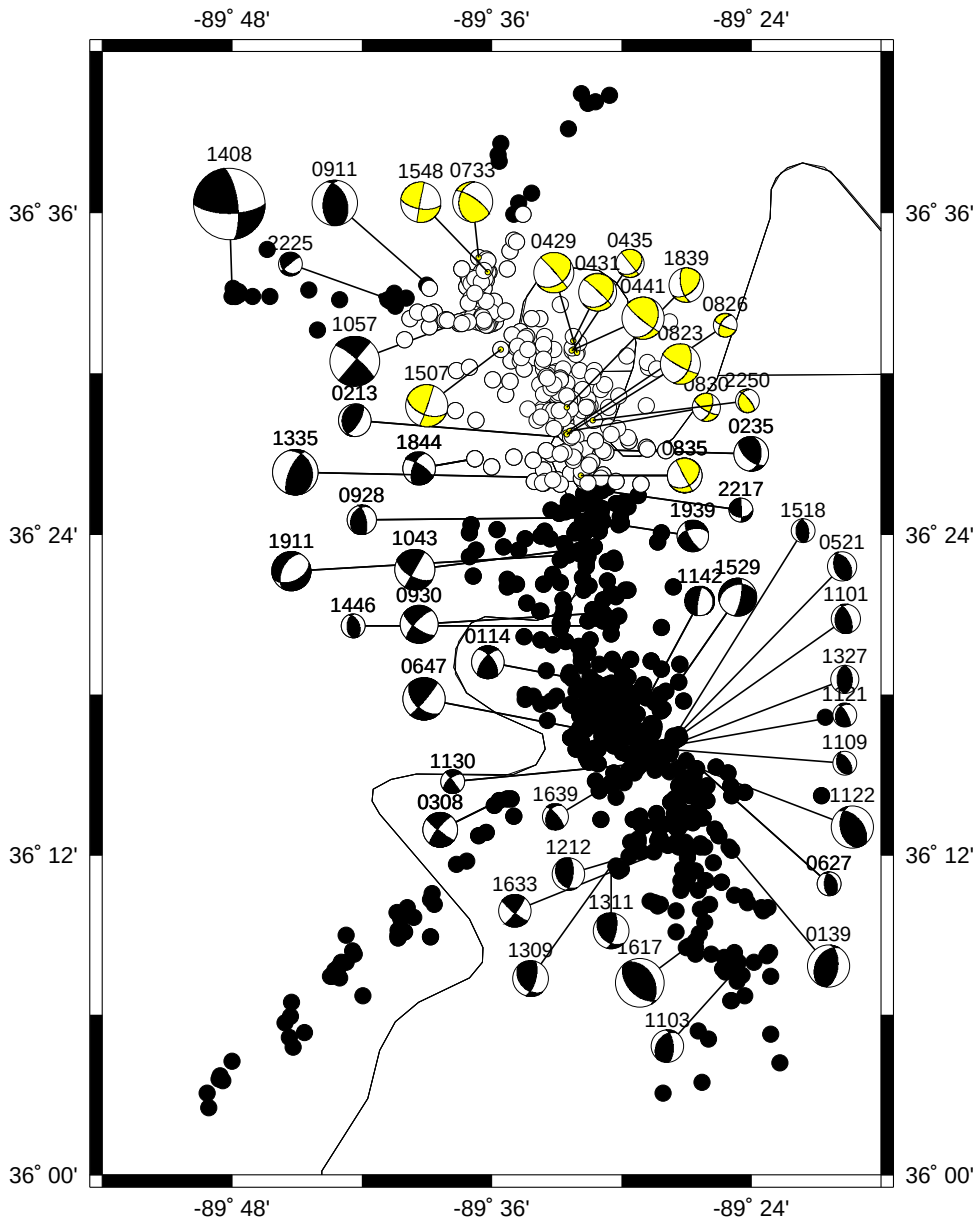

Fig. 4.9b. The focal mechanisms and hypocenters of the central NMSZ, NW segment (white), will be discussed in detail in Figure 4.9c.

N80°W and 4-14 km depth, which is consistent with the left-lateral strike-slip focal mechanism of the 1408.

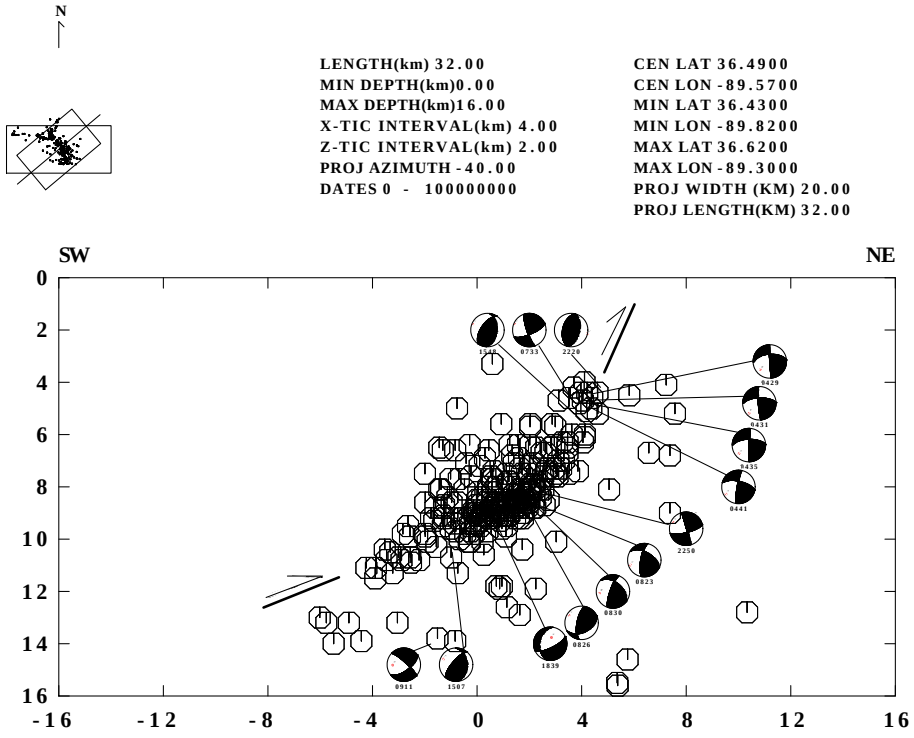

Fig. 4.9c. Cross section of earthquake hypocenters with strike N40°W in the NW segment suggests a listric structure striking N40°W dipping ~70°SW near surface and ~35°SW in depth > 9 km. The projection of the focal mechanism onto the vertical plane of 0429, 0431, 0435, 0441 (all depths<5 km) indicate a reverse motions with large left-lateral slip on a vertical nodal plane striking NW. Those of 0823, 0830, 1839, 1507, 1548 suggest left-lateral oblique reverse motion on similar striking nodal planes with smaller dip angles with deeper depth than that of 04 events. Those of 2250 and 0911 show major reverse faulting on similar striking plane.

Second, the focal mechanism of event 1057 (m_{Lg}=3.2) suggests a right-lateral strike-slip movement on a vertical nodal plane striking NE, which is aligned with the NE arm. The focal mechanisms indicate a horizontal E-W compression. This is a typical focal mechanism characteristics of the right-lateral strike-slip fault system with a left-stepping offset. A seismic cross projection along the NE arm shows a

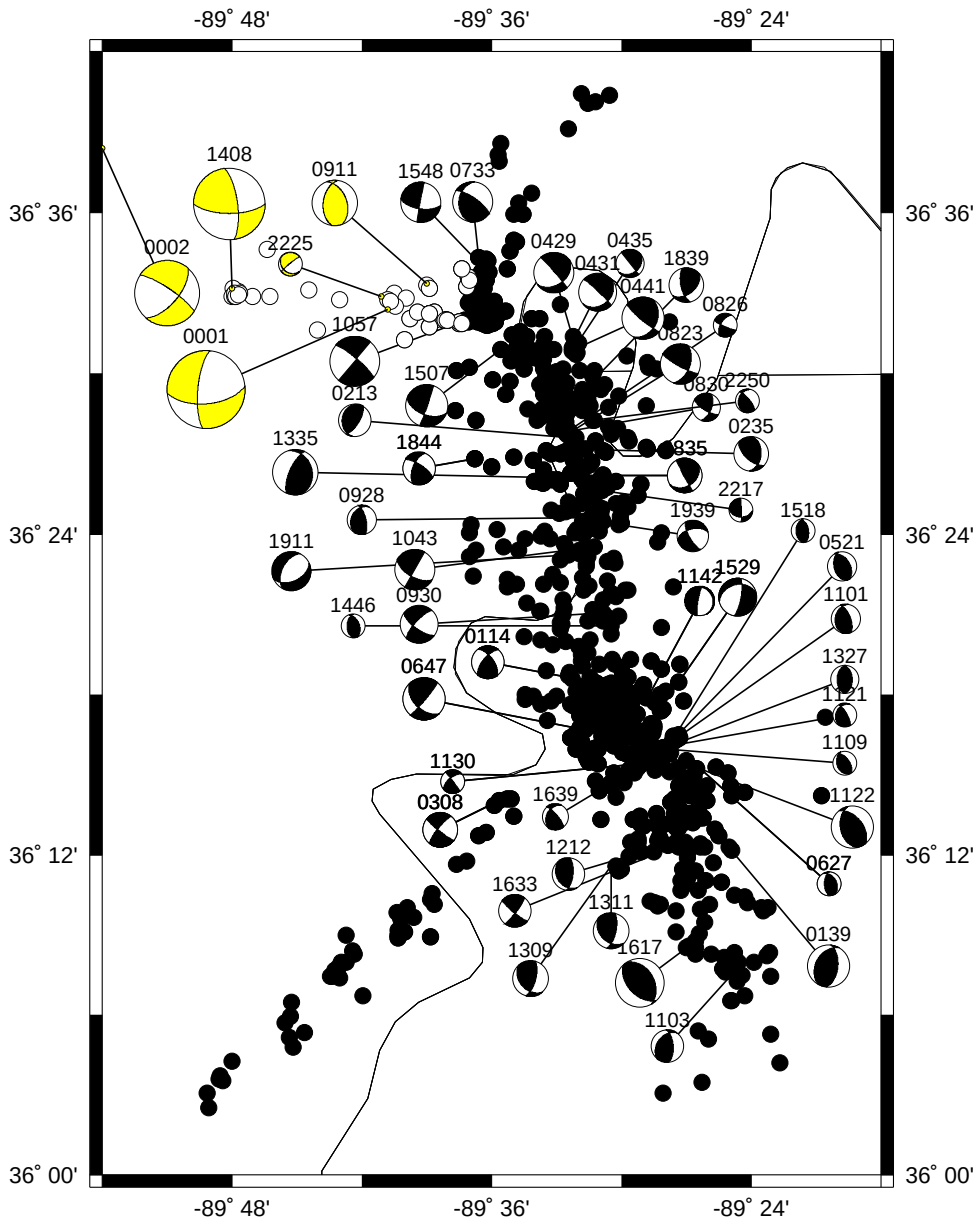

Fig. 4.10a. The focal mechanisms and hypocenters of the central NMSZ, westerly arm (white), will be dicsussed in detail in Figure 4.10b.

vertical fault plane with width of 8 km and depth 4-14 km (Figure 4.11a,b).

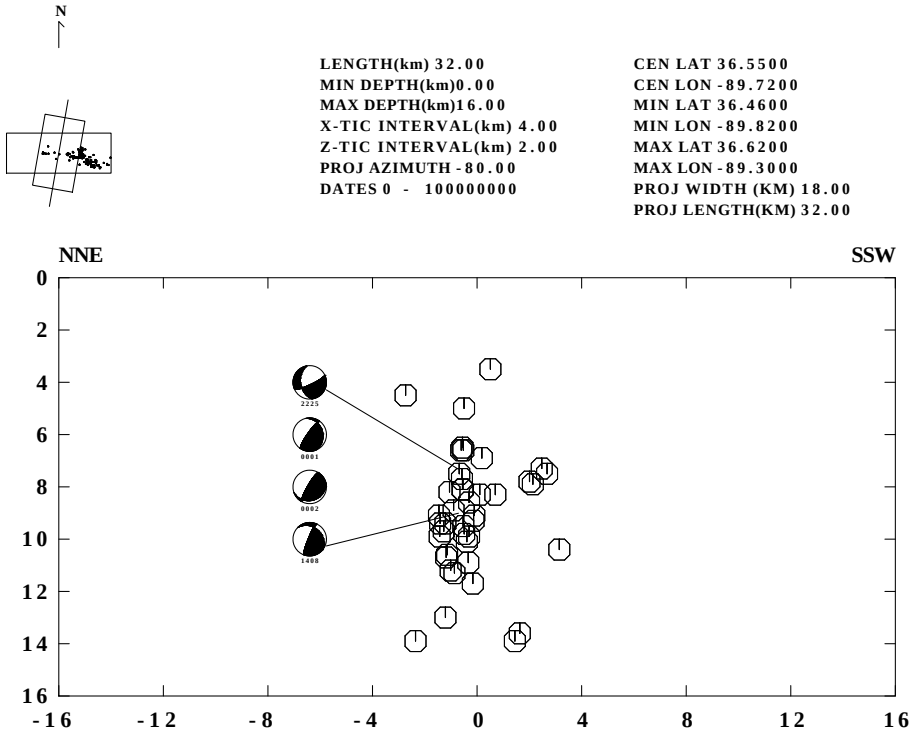

Fig. 4.10b. Cross section perpendicular to N80°W suggests the westerly arm is a narrow vertical (width ~4 km) fault striking ~NWW with left-lateral strike-slip motion.

Third, the focal mechanism of event 0911 (m_{Lg}=2.9 and depth=12.9 km) indicates a pure thrust motion occurred on striking NS and dipping W nodal plane in response to the E-W compression. There is no evidence to consider the dipping east nodal plane as a fault plane (Figure 4.10a). It can be explained as either a deep event on the extension of NW left-lateral oblique-reverse fault or similar thrust event to that of central segment.

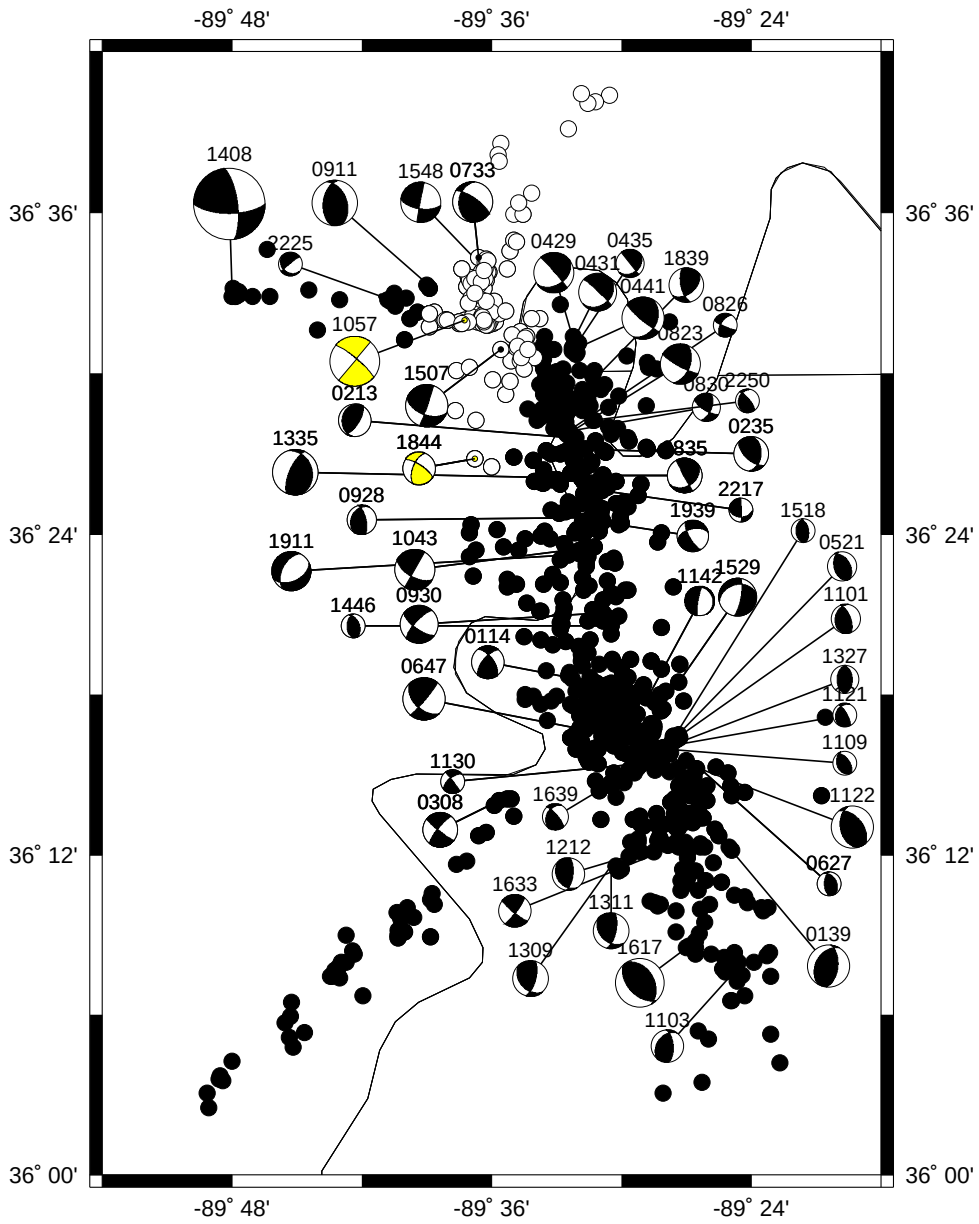

Fig. 4.11a. Focal mechanisms and hypocenters of the central NMSZ, N-E arm (white), will be discussed in detail in Figure 4.11b."

4.2.3 A new structure in the South NMSZ

In the southern end of NMSZ, the earthquake locations of the last 30 years shows a seismicity pattern striking NE and parallel to the

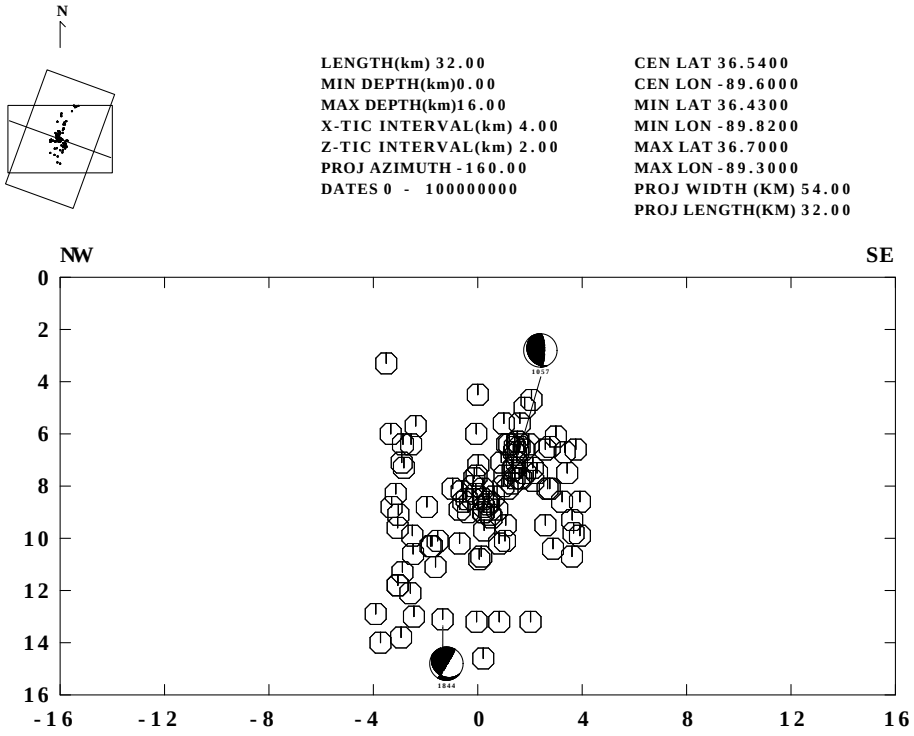

Fig. 4.11b. Cross section perpendicular to N20°E indicates the NE arm is a vertical fault with width of 8 km and depth 4 - 14 km. Vertical plane projections of 1057 and 1844 suggest this is a right-lateral strike-slip fault.

southern axial arm (Figure 4.1). In a period of nine months of PANDA recording 3 earthquakes with m_{Lg} >3.0 occurred on the seismic pattern. The Ripley, Tennessee earthquake of 29 August 1990 (0907, m_{Lg} = 3.8) is the largest, and western Tennessee was shaken by it. A total of 45 P-wave first motions from PANDA and Saint Louis University regional network are used to determine the focal mechanism of the event (Figure 4.12). The result with well-constrained nodal planes indicates right-lateral strike-slip movement on a vertical nodal plane striking NE (strike = 222, dip = 79, slip = -162) under N85°E

compression. This focal mechanism is consistent with the result (strike = 222.9, dip = 86.8, slip = -179.5) obtained by Taylor and Wuenscher (1990). The mechanism of 0907 is similar to the right-lateral strike-slip mechanisms for events located along the southern axial arm. It is important to note that the 1981 event (August 7, m_{Lg} = 4.0) appears to be associated with the newly defined fault. The similarity of the focal mechanism, coupled with the Ripley epicenter on the southern border of the Reelfoot Rift, strongly suggests that this fault parallel to the axial arm is also active. The intersection of the new southernmost arm with the SE segment of the central NMSZ may explain the thrust seismicity of the SE segment.

4.2.4 Stress field analysis of the central NMSZ

Figures 4.13a, b show the P- and T- axis map view. Most focal mechanisms with the horizontal P-axis trending EW are located in the SE, central segment and southern intersection, although the most mechanisms with horizontal NE-SW P- axis are concentrate near the northern end of NMSZ. This study also shows that most right-lateral strike-slip and thrust focal mechanisms have near EW horizontal P-axes, while the most focal mechanisms with left-lateral strike-slip component have horizontal near NE-SW P-axis. A N84°E maximum horizontal stress is inferred in the central and SE segment by averaging P-axis direction, whereas N65°E maximum horizontal stress is inferred for the northern end of the central NMSZ near New Madrid.

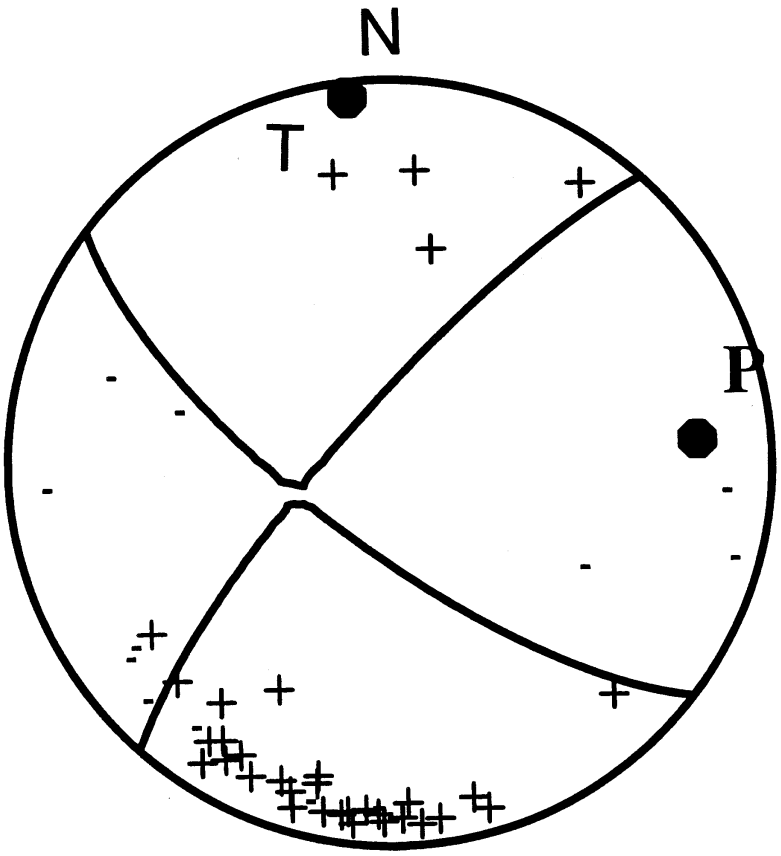

Fig. 4.12. Focal mechanism of 0907, total 45 P-first motions from PANDA and regional networks are used. The focal mechanism is similar to those of SW axial arm.

The difference stress situation in central part and northern end of NMSZ are also observed by previous authors (O'Connell *et al.*,1982, Andrews *et al.*,1985; Nicholson *et al.*, 1984). Russ (1982) suggested that the NE stress results from a local rotation of the EW regional stress field in the left-step over area.

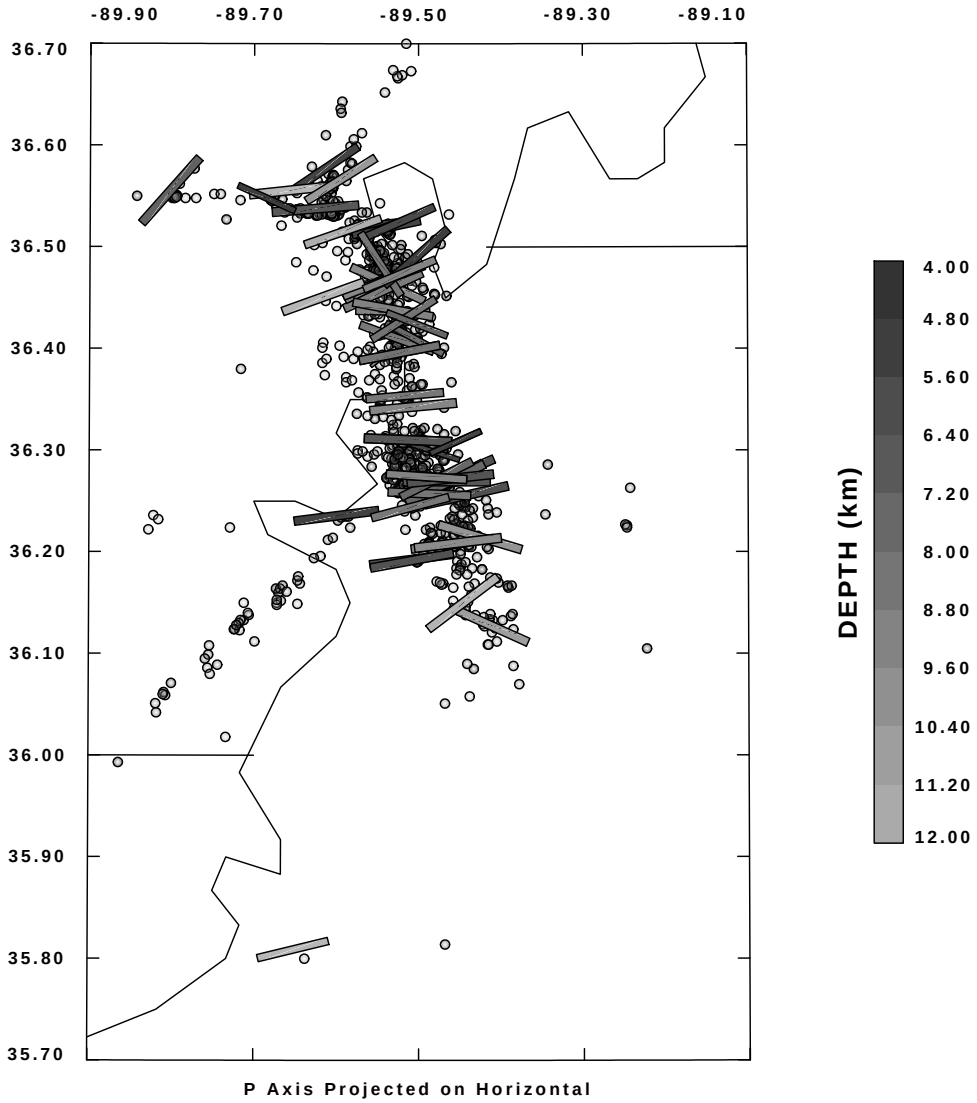

Fig. 4.13a. Projection of P-axis onto horizontal. The length of the projected bar is proportional to the degree that the axis is horizontal, e.g., a vertical axis has zero length. Note the uniform orientations.

4.2.5 Seismic moment

In addition to the geometry of faulting, the seismic moment was obtained from moment-tensor inversion of P-, SV-, and SH-amplitudes. Figure 4.14 shows a relationship between seismic moment and

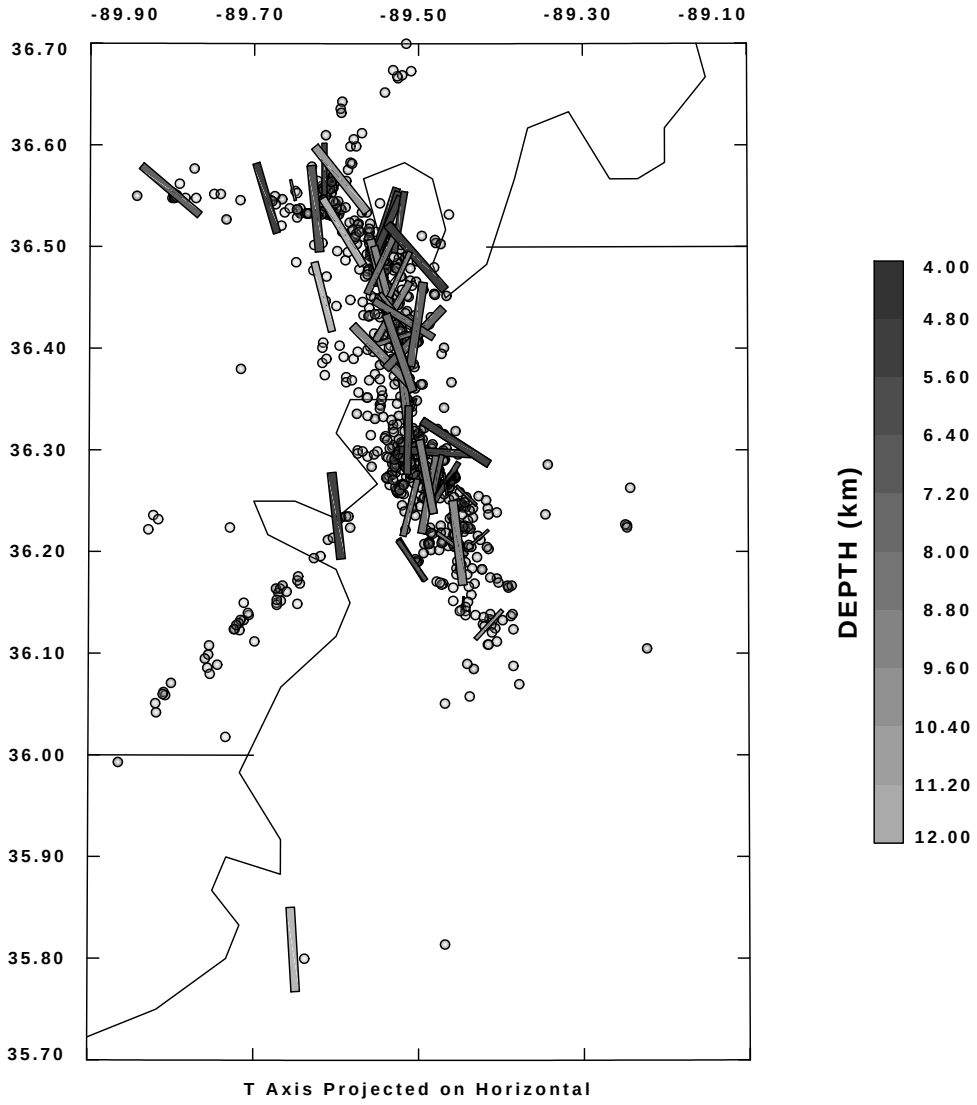

Fig. 4.13b. Projection of T-axis onto horizontal. The length of the projected bar is proportional to the degree that the axis is horizontal, e.g., a vertical axis has zero length. Note the somewhat uniform orientations.

reported Saint Louis University network's magnitude m_{Lg}:

$$\log M_0 = (17.8 \pm 0.18) + (1.01 \pm 0.08) m_{Lg}$$

where M_0 is seismic moment and m_{Lg} is magnitude from "Central

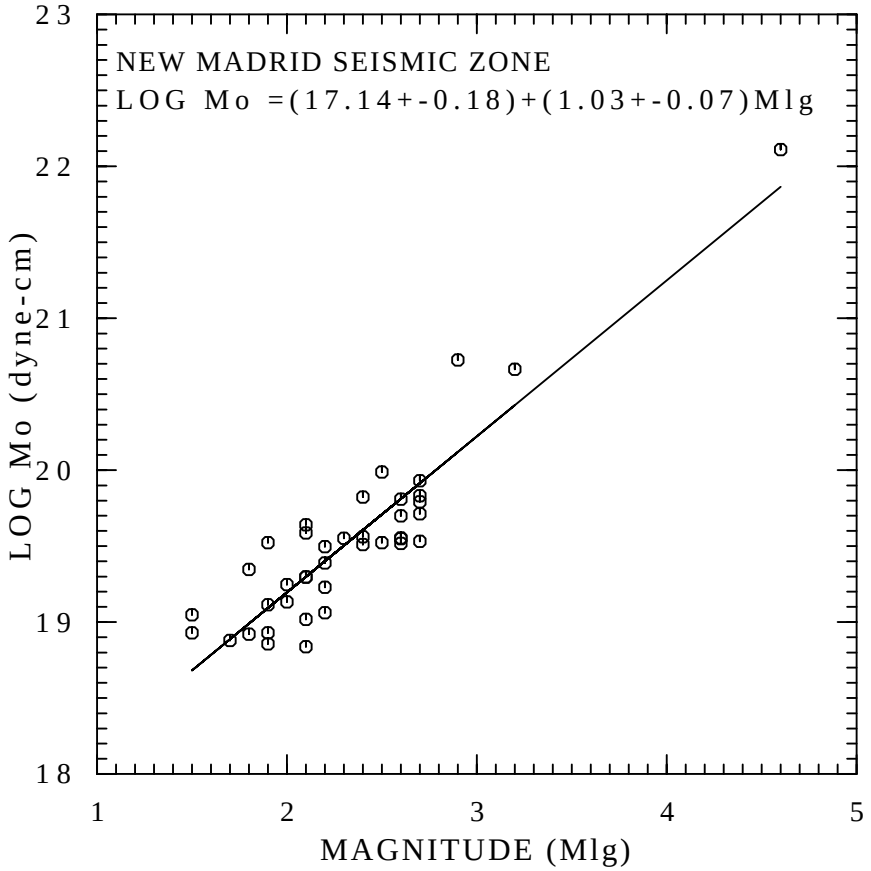

Fig. 4.14. Relationship between M_0 and m_{Lg}.

Mississippi Valley Earthquake Bulletin" of Saint Louis University.

4.3 Discussion

Focal mechanisms of 54 microearthquakes located in the central NMSZ were determined using three-component digital PANDA data and waveform modeling. Spatial distribution of hypocenter was given by JHD relocation (Pujol, 1997). The results allow us to establish a

seismotectonic model of the NMSZ, to examine the correlation between seismicity and geologic features and to discuss the seismogenesis.

4.3.1 A seismotectonic model

A seismotectonic model was developed (Figure 4.15) based on the three-dimensional pictures of the fault slip. The model supports previously identified three major seismic arms of Southern axial arm, Westerly arm and Northeast arm. The southern axial arm is a ~100 km long, right-lateral strike-slip fault along the Reelfoot rift axis. Reflection surveys show that this rift axis is an axial fault zone at seismogenic depths within the crystalline crust. The axial fault zone is a first-order feature in the Reelfoot evolution (Hildenbrand and Hendricks, 1995). The first event of December 16, 1811 (M = 8.1) was probably on the axial fault (Nuttli, 1973a; Johnston and Schweig, 1996) Its northeast extension, Called the Blytheville fault zone, across the river is also coincident with the concentrated zone of seismicity. Johnston and Schweig (1996) suggested the BFZ could continue and intersect the Reelfoot fault at the southwest end of Reelfoot Lake. Rapid intraplate strain accumulation since 1950 in the NMSZ was found by remeasurement of triangulation network in the southern part of the NMSZ with the Global Positioning System. The orientation and sense of shear is consistent with right-lateral strike-slip motion along the southern axial arm (Liu *et al*., 1992).

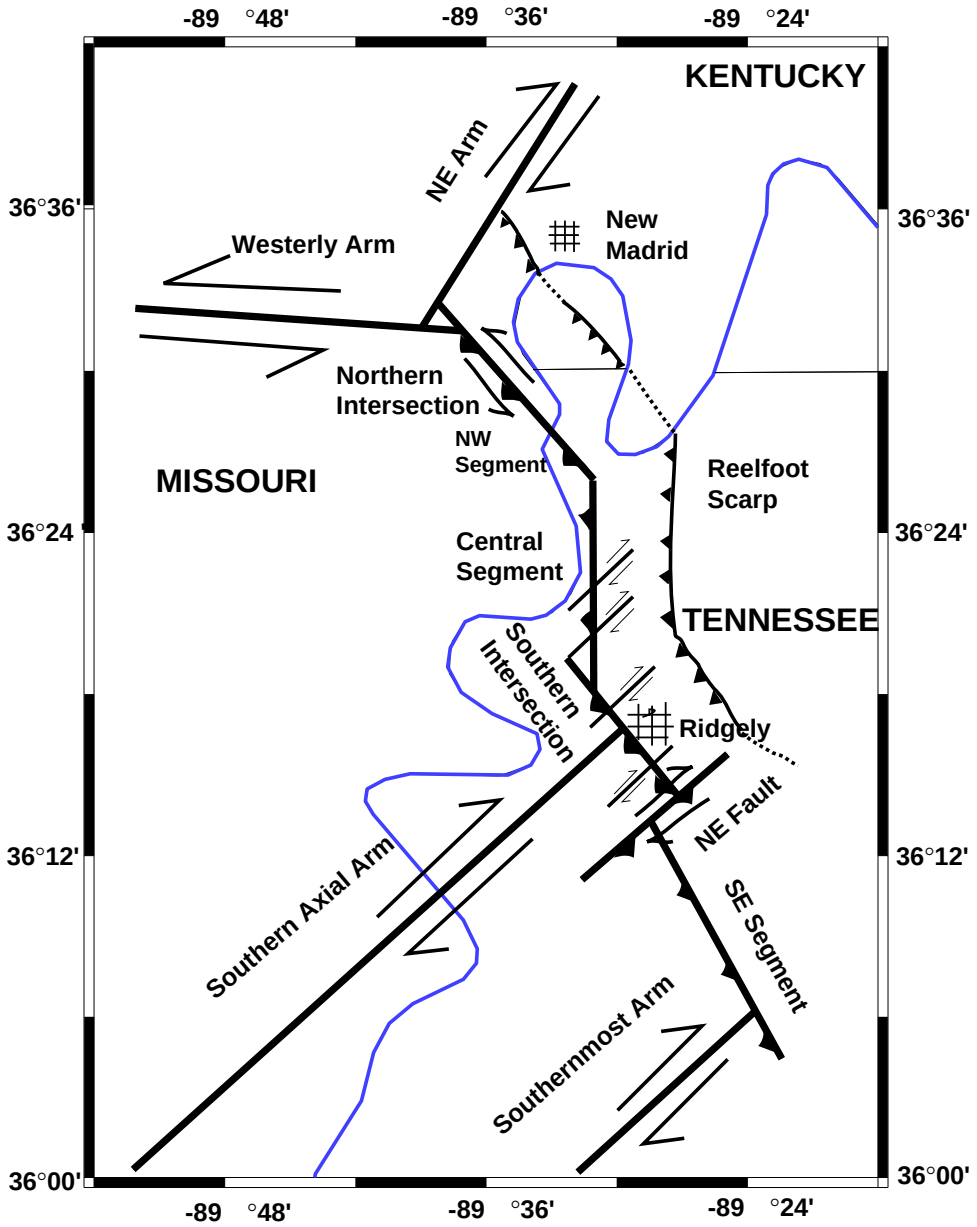

Fig. 4.15. A sketch map of seismotectonic model of the NMSZ (Herrmann and Canas *et al*. 1978; Herrmann, 1979; Herrman and Ammon, 1997 and this study)

The westernly arm is a narrow (only 4 km wide) left-lateral strike-slip fault. Most events are located at 4-14 km depth, implying that the earthquakes occur in the granitic basement. This NWW trending arm

correlates well with the western boundary of the Mississippi Valley. The current seismicity is more active than other arms. Three earthquakes with magnitude m_{Lg}>4.2 concentrated on the Westerly arm. The maximum horizontal compressive stress trends N65°E in the westernly arm. Gravity data suggest a strong correlation between the seismic arm and the region of the thickest anomalous crust (Hildenbrand, 1985). The highest heat flow anomaly of the Mississippi Valley is discovered in this area (Swanberg *et al*., 1982). A component of convective heat flow due to ground water ascending along active faults provides possible explanation for the anomaly. All of the evidences supports the active seismicity in this area is related with the deep structure activity corresponding to a major basement offset boundary of the rift. The NE arm near New Madrid with right-lateral strike-slip is also determined. The New Madrid north fault parallels the NE arm but is slightly offset from it. Johnston and Schweig (1996) suggested the earthquake of Jan. 23, 1812 occurred either in the New Madrid westerly arm or New Madrid north fault.

The central NMSZ is characteristized by local Bouguer gravity anomalies (Stearns, 1979), due to a series of igneous intrusive mass as inferred from seismic-reflections profiles. Most of the current microseismicity in the central NMSZ underlies the Lake County Uplift, a broad, low-amplitude anticline. We divided the central NMSZ into three segments and two intersections. The SE segment is oriented N30°W, 45° SW and is characterized by the thrust type focal mechanisms. A right-lateral oblique reverse fault striking NE and dipping 60

- 70° SE formed a NW boundary of the SE segment. At the southern intersection located near Ridgely, a major reverse fault striking NNW and dipping 40° SW was defined. The shallow right-lateral strike- slip faults are parallel to the Southern axial fault and located on the hanging wall of the reverse fault. The central segment is a thrust fault striking NS and dipping 30°W, called . the Reelfoot fault (Johnston and Schweig, 1996), which is expressed at the surface as the Reelfoot scarp (Figure 4.15). The surface projection of the central segment would reach the surface approximately at the Reelfoot scarp if the 60-70° dip (Sexton and Jones, 1986) is used at depths < 5 km.

We did not find the reverse fault dipping 60-70° at depth < 5 km in the central segment but in the NW segment. The NW segment is a listric fault with a strike N40°W and a dip 70°SW near surface and 35° SW at depth > 9 km. This segment implies left-lateral oblique-reverse slip. The surface trace of the listric fault is just the site of the KBS, which is the northern extension of the Reelfoot Scarp. The central NMSZ is on or near a crest of a north-trending elongated positive Bouguer gravity anomaly (Stearns, 1962). The sources for such an anomaly are likely to occur at least 5 km deep and just at the earthquake focal depths. The earthquake of Feb. 7, 1812 (M =8.0) with the reverse movement occurred at the Reelfoot fault site. The tectonic deformation in the central NMSZ is reflected in the seismicity, the Lake County Uplift, Reelfoot Lake. Lake County Uplift is upwards as much as 10 m above the general level of the Mississippi River valley (Russ, 1982). Because the major structures in the central NMSZ are

the N-NW striking reverse faults, then the Lake County Uplift would be on the upthrown hanging wall and Reelfoot lake on the downthrown footwall. The Reelfoot Scarp, it's northern extension and the Lake County Uplift are the surface expression of faulting along the central NMSZ. The new evidences supplied here provides a consistent explanation for the existence and location of the Lake County Uplift, the wide-to-the north, narrow-to-the south shape of the Lake County Uplift, and the subsidence and/or impoundment of Reelfoot Lake (Chiu *et al*. 1993).

More complex focal mechanisms are determined in the area between Ridgely and New Madrid (O'Connell *et al*. 1982; Nicholson *et al*. 1984; Andrews *et al*. 1985; Young *et al*. 1995; and this study). We inferred that these complex focal mechanisms are correlated with the complex cross faulting procedure in the left-step offset. The strike-slip earthquakes in the central segment might relate with the vicinity faulting (figure 4.15).

A new right-lateral strike-slip seismic arm was defined at the southernmost end of the central NMSZ, which parallels the southern axial arm and intersects with the central NMSZ. We suggested that the effect of compression of the new NE on the SE segment provides an explanation for the thrusting observed on the SE segment.

All of the NMSZ is controlled by a regional N84°E maximum horizontal compressive stress. Two major north-east striking zones with right-lateral strike-slip movement cause strong compression in the NMSZ left step. Thrust faulting and uplift is produced here. The

N65°E maximum horizontal stress at the northern end of the NMSZ represents a localized change, perhaps due to the influence of local intrusions (O'Connell *et al*.1982; Russ, 1982).

4.3.2 Seismogenesis of the NMSZ

Hildenbrand and Hendricks (1995) and Hildenbrand *et al*. (1996) studied the relationship between seismicity and geophysical features. They found that 1) many of the earthquakes are within the region defined by the intersection of the Missouri Gravity Low (MGL) and the Reelfoot Graben; 2) the seismic zone is underlain by igneous intrusions within the graben, which exhibit the magnetic and gravity highs. 3) earthquakes are concentrated near Bloomfield pluton (Figures 1.3, 1.5). The rock weakness is due to preexisting rift fractures and/or high pore fluid pressure (Al-Shukri and Mitchell, 1988) at the intersection of the MGL with Reelfoot graben and the far field stress's concentration around the intrusions are the possible seismogenesis in the NMSZ area. To the west of New Madrid, the seismic trend changes direction and forms two arms. These changes may be controlled by presence of the Bloomfield pluton. The resulting preferred directions of strain release parallel the southern and eastern edges of the pluton. Thus, the linear seismic zones changed trend to follow paths of less resistance (Hildenbrand and Hendricks, 1995).

4.4 Summary

1) Source parameters of 54 microearthquakes (m_{blg}=1.5-4.6) located in the central NMSZ were estimated using high-quality, three-component digital PANDA data with waveform modeling techniques. The waveform inversion procedure includes: a) computing Green's function based on well defined velocity (Chiu *et al*., 1993) and attenuation models (Liu *et al*., 1994); b) a grid search of P-, SV- and SH- amplitudes for all possible values of strike, dip, and rake, at 3° increments. The best fit between observed and synthetic seismograms determines the optimal source parameters. c) application of an F-test permits confidence bounds on the P , T and B axes of the focal mechanisms.

2) The polarizations, amplitudes, amplitude ratios and arrival times of the direct P-, SV-, SH-, even PS and SP converted phases of the synthetic seismograms are consistent with those observed. These facts imply that the velocity and attenuation model, the focal mechanism solutions obtained using the grid search method are reliable. A test of method's reliability indicate the good reliability of both moment tensor inversion and grid search techniques.

3) A seismotectonic model was created, which supports previously identified epicentral trends and clearly illustrates the relationship between the seismicity pattern and the major feature of the rift. The right-lateral strike-slip southern axial arm trend closely approximates the rift axis. The trend west of New Madrid is

aligned with a segment of the western boundary of the Mississippi valley graben and shows left-lateral strike-slip movement. The consistency of higher seismicity activity, higher heat flow anomaly (Swanberg *et al.* 1982), the thicker crust (Hildenbrand, 1985) provide the evidence of that the higher seismic action results from the deep active structure.

4) In the seismotectonic model, the geometry and style of faulting of the central NMSZ are defined. The central NMSZ is a major reverse faulting seismic zone with variable orientations and seismicity. We divided the central NMSZ into 3 segments called SE, central and NW according to the orientation of seismic pattern, seismicity characteristics and focal mechanism. The SE segment is oriented N30° W, 45°SW and is characterized by thrust type focal mechanisms. The other conjugate thrust fault strikes NE and dips SE and may be a subfault of the axial arm. The central segment strikes NS and dips 30°W, and displays thrust mechanisms. Some events with mixed focal mechanism may be affected by nearby faulting. The NW segment is a listric fault with a strike N40°W and dips 70°SW near the surface and 35°SW at depths>9 km. Focal mechanisms along this segment imply left-lateral oblique-reverse slip. A series of shallow earthquake zone with right-lateral strike-slip faulting may be the extension or subfault of the SW axial fault.

5) Cross faulting is observed at the southern and northern intersections. At the southern intersection of the central NMSZ with the

right-lateral strike-slip southern arm of NMSZ we observed both right-lateral strike-slip and thrust faulting. A vertical cross projection defined the intersection of the two faults and indicates the strike-slip movement occurred on the hanging wall of the thrust faulting. Some events with large normal faulting components on vertical nodal plane are located on the NE end of the intersection. Two cross fault systems occur at the northern intersection of the NW segment with the right-lateral N-E arm and the left-lateral westerly arm of the NMSZ. As mentioned before, higher seismic activity occurred here. The complex focal mechanisms between Ridgely and New Madrid found by many authors can be explained by the complex cross faulting environment.

6) The relationship between seismicity and geological feature in the central NMSZ were studied. The Lake County Uplift, the KBS of the northern extension of the Reelfoot scarp are the surface expressions of the thrust faulting along the central NMSZ. The Lake County Uplift would be on the upthrown hanging wall and Reelfoot Lake on the downthrown footwall.

7) A N84°E maximum horizontal stress is inferred in the central NMSZ by averaging the P- axis directions on the SE, central segment and southern intersection. This direction is consistent with regional stress field. A N65°E maximum horizontal stress is inferred for the northern end of the central NMSZ. This is related to a local change of regional stress in the left-step over area. This NE striking stress is also consistent with the stress field of the

central United States of America (Zoback and Zoback, 1991).

8) The crustal weakness resulting from the preexisting rift fractures and the high pore fluid pressure at the intersection of the Missouri Gravity Low with the Reelfoot graben and the far field stress's concentration around the intrusions are the possible causes for seismogenesis in the NMSZ area.

9) We identify a new active right-lateral strike-slip arm in the southern most of the NMSZ that is parallel to the southern axial arm. The thrust seismicity in the SE segment of the central NMSZ may be explained by the intersection with the new arm.

10) This successful study demonstrated that waveform inversion technique can be applied to high frequency data for nonrock sites. In particular, the thick sedimentary column was beneficial to the study because the S-wave particle motion was forced to be horizontal and the P-wave vertical. The use of F-test statistics provides the basis for follow up studies on stress patterns by quantifying the P- and T-axis orientations.

CHAPTER 5

CONCLUSIONS

5.1 Contributions of this study

The major contributions of this study include:

1) modeling of body wave propagation in the sediments of the NMSZ,
2) estimating a data set of the focal mechanisms and their seismic moments for microearthquakes in the NMSZ,
3) developing a seismotectonic model of the NMSZ, inferring the geometry and style of the active faulting of the central NMSZ as well the relationship to geologic features,
4) determining the stress field in this area, and
5) developing a procedure to determine source parameters using earthquake modeling.

5.2 Future research areas

Zoback and Zoback (1991) mentioned that the focal mechanism records deformation and not stress. The P and T axes are not the maximum and minimum principal stress directions, but are the compressional and extensional strain directions for the two possible faults. However, in most intraplate areas, P axes do seem to represent good approximations of the maximum horizontal stress direction. Zoback and Zoback (1991) also suggest that to optimize the use of focal plane mechanism data for determining stress orientations it is necessary to consider multiple events in a given region and use either the average P-axis direction as the maximum horizontal stress direction or to formally invert a group of focal plane mechanisms to determine the orientation and relative magnitude of the principal stress tensor. In this study, we have determined the orientation of maximum horizontal stress by average orientation of the P-axes of the well constrained focal mechanisms. However, the relative magnitude of the principal stress is not defined. Therefore, a inversion of the focal mechanisms determined in this study is necessary to determine the orientation and relative magnitude of the principal stress tensor (Gephart and Forsyth, 1984).

A new southernmost seismic arm is indicated in this study, which is a right-lateral strike-slip fault striking NE and parallel to the NE-SW axial arm. The intersection of the new southernmost arm with the central NMSZ may explain the thrust seismicity of the SE segment.

This hypothesis needs a numerical examination as well are data from future earthquakes along this trend.

There are three basic hypotheses to explain the seismic trends of the NMSZ. First, the southern axial arm is along the axis of the graben. However the right-lateral strike-slip movement along the zone is incompatible with that of extensional features such as rifts. Hildenbrand (1985) proposed that the complex tectonic evolution of the upper Mississippi Embayment since late Precambrian time involves rift formation possibly along a pre-existing shear zone. Second, the seismicity trends change abruptly from northeast to slightly west of north at the intersection of the graben with the Missouri Gravity Low (Hildenbrand and Hendricks, 1985). This trend change may be intimately related to inferred igneous masses emplaced along the axis of the graben. The third hypothesis explains the linear seismic zones that strike in westerly and northeasterly directions. The Bloomfield pluton influences the distribution of stress in this region (Hildenbrand and Hendricks, 1995). The stresses are concentrated around the periphery of plutonic masses in much the same manner as stress concentrations occur near holes in plates under stress. McKeown (1978) hypothesized that earthquakes in the central and eastern United States are the result of local high-stress concentrations at the boundaries between mafic alkaline plutons and their host rocks. Andrews *et al*. (1985) suggested that this hypothesis can be reasonably invoked to explain the concentration of seismicity between Ridgely and New Madrid because gravity and aeromagnetic data indicate a ring dike

complex south of New Madrid (Hildenbrand, 1985). Seismic reflection profiles reveal localize intrusions of estimated middle Eocene age in the Ridgely area (Zoback *et al*. 1980). Seismic refraction studies suggest that the altered lower crustal layer, which is considered a zone of mantle intrusives, thickens beneath this area (Mooney *et al*. 1983). The intrusion hypothesis might also explain the diversity of focal mechanisms for the events between Ridgely and New Madrid, because local changes in the direction of stress would be expected in an area of complex geologic discontinuities.

Andrews *et al*. (1985) point out that the main problem with the intrusion hypothesis is that there is no unique association of seismicity with intrusive rocks. These intrusion occur all along the otherwise aseismic rift boundary. Thus on the basis of the available evidence, Andrews *et al*. (1985) conclude that neither the rift structure nor the distribution of plutons completely explains the present-day distribution of seismicity. We need a detailed mechanical analysis for the seismic cause of the NMSZ.

We have mentioned that the existence of the interpreted weak zone at the intersection of the Missouri batholith and the Reelfoot graben (Hildenbrand and Hendricks, 1985) and increased pore pressure (Hildenbrand and Hendricks, 1985; Al-Shukri and Mitchell, 1988) are the two major contributing factors to the occurrence of earthquakes in the NMSZ. Another factor is the far field stress concentration around the periphery of these individual intrusions (Hildenbrand and Hendricks, 1985; Andrews *et al*. 1985). In the central and eastern

United States, other large rift systems, like the Oklahoma aulacogen and Midcontinent rift system, are similar to the Reelfoot rift and represent major crustal flaws. Why the NMSZ is the most active in the Eastern United States? We need further studies to combine the several factors to distinguish the New Madrid seismic zone as the particularly active area in the Eastern United States.

Nuttli (1973a) estimated the epicenters of the earthquakes in the winter 1811-1812. Two of them were located at axial seismic zone and the Reelfoot fault, and other one was near New Madrid. The larger earthquakes of recent seismicity were located near the ends of the main trends of seismic activity (Mitchell *et al*. 1991), and the westerly arm is more active (Gomberg, 1994). Johnston and Nava (1985) estimated that there is a 40 to 63 percent probability of an $m_b \geq 6.0$ and 1 percent probability of an $m_b \geq 7.0$ event occurring by the year 2000. These probabilities increase to 86 to 97 percent for $m_b \geq 6.0$ and 4 percent for $m_b \geq 7.0$ by the year 2035 in the New Madrid Seismic Zone. Future work should concern this question "Where will the next large earthquake be ?" The practical long-term objective is to define criteria for delimiting high-risk zones in the NMSZ and throughout the eastern United States (Liao and McMechan, 1996).

Al-Shukri and Mitchell (1988) reported reduced seismic velocities in the source zone of New Madrid earthquake. This is an interesting result. Similar results were also found in Kobe, Japan. Recently, Zhao *et al*. (1996) developed a seismic tomography technique, which can determine the P-, S-wave velocity and Poisson' ratio anomaly. He

discovered a low velocity (-5%) and high Poisson's ratio (+6%) anomaly covering about 300 square kilometers at the hypocenters of 17 January 1995, magnitude 7.2, Kobe earthquake in Japan. He explained that this anomaly may be due to an overpressurized, fluid-filled, fractured rock matrix that contributed to the initiation of the Kobe earthquake. A new tomography study is necessary using 3-component PANDA data with the regional network data and Zhao's technique to extend Al-Shukri and Mitchell's (1988) findings. This study will determine not only P-wave but also S-wave velocity and Poisson's ratio anomaly. Higher resolution can be obtained. This work may be helpful in determining the detailed crustal structure in the NMSZ and answer "Where will the next large earthquake be ?".

To reduce the future seismic hazard, the strong ground motion analysis and seismic hazard estimation are the most important work. This work depends on the source parameters and the seismotectonics. The focal mechanisms and the seismic moments data set has been obtained, and a seismotectonic model has been developed. The next work should be its application to seismic hazard reduction. The three component PANDA deploy was only for a period of three years, concentrated around the central part of the NMSZ. A permanent three component, high-resolution digital seismic array is being deployed throughout the NMSZ as part of the cooperation New Madrid Seismic Network.

We successfully applied a waveform modeling technique to the local seismic data. We need to extend this technique to combine local,

regional, and teleseismic network data to determine the earthquake focal parameters.

BIBLIOGRAPHY

Aki, K. and P. G. Richards (1980). Quantitative seismology: Theory and Methods, W.H. Freeman and Co., New York, San Francisco, 932. pp.

Al-Shukri, H. J., and B. J. Mitchell (1988). Reduced seismic velocities in the source zone of New Madrid earthquakes, *Bull. Seism. Soc. Am.* **78,** 1491-1509.

Al-Shukri, H. J., and B. J. Mitchell (1990). Three-Dimensional attenuation structure in and around the New Madrid seismic zone, *Bull. Seism. Soc. Am.* **80,** 615-832.

Al-Shukri, H. J., and B. J. Mitchell and A. A. Ghalib (1988). Attenuation of seismic waves in the New Madrid seismic zone, *Seismo. Res. Letters* **59,** 133-140.

Andrews, M. C., W. D. Mooney and R. P. Meyer (1985). The Relocation of Microearthquake in the Northern Mississippi Embayment, *J. Geophys. Res.* **90,** 10223-10236.

Austin. C. B., and G. R. Keller (1982). A crustal structure study of the northern Mississippi Embayment, Investigations of the New Madrid, Missouri, Earthquake Region, edited by F. A. McKeown and L. C. Pakiser, *U. S. Geol. Surv. Prof. Pap.,* **1236-G,** 83-93.

Braile, L. W., W. J. Hinze, G. R. Keller, and E. G. Lidiak (1982). The

northeastern extension of the New Madrid, Missouri, Earthquake Region, edited by F. A. McKeown and L. C. Pakiser, U.S. Surv. Prof., 1236-L 175-184.

Braile, L. W., W. J., Hinze, G. R., Keller, E. G., Lidiak, and J. L., Sexton (1986). Tectonic development of the New Madrid rift complex, Mississippi Embayment, North America, *Tectonophysics,* **51,** 1494-1486.

Burke, K. and J. F. Dewey(1973). Plume-generated triple Junctions: key indicators in applying plate tectonics to old Rocks, *J. Geology* **81,** 406-433.

Cagniard, L. (1962). Reflection and refraction of progressive seismic waves, transl. by E. A. Flinn and D. H. Dix, McGraw-Hill, New-York.

Chen, K. C., J.-M. Chiu, and Y. T. Yang (1993). 3-Dimensional Configuration of the Sedimentary Basin in the Upper Mississippi Embayment using S-to-P Conversion Waves, *(unpublished manuscript)* University of Memphis.

Chen, K. C., J.-M. Chiu, and Y. T. Wang (1993). Q_P - Q_S relations in the sedimentary basin of the upper Mississippi Embayment using converted waves, *Bull. Seism. Soc. Am.* **84,** 1861-1868.

Chiu, J.-M., G. Steiner, R. Smalley, Jr., and A. C. Johnston (1991). PANDA: a simple, portable seismic array for local to regional-scale seismic experiments, *Bull. Seism. Soc. Am.* **81,** 1000-1014.

Chiu, J.-M., A. C. Johnston and Y. T. Yang (1992). Imaging the active faults of the central New Madrid seismic zone using PANDA array data, *Seism. Res. Lett.,* **63**, 375-393.

Cordell. L. (1977). Regional positive gravity anomaly over the Mississippi Embayment, *Geophys. Res. Lett.,* **4,** 285-287.

Draper and Smith (1966). Applied regression analysis, New York, Wiley.

de Hoop, A. T. (1960). A modification of Cagniard's method for solving

seismic pulse problems, *Appl. Sci. Res. Section B,* **8,** 349-356.

Ervin, C. P., and L. D., McGinnis (1975). Reelfoot rift-reactivated precursor to the Mississippi Embayment, *Bull. Geology. Soc. Am.* **86,** 1287-1295.

Fan, G.-W., S. L. Beck and T. C. Wallace (1993). The seismic source parameters of the 1991 Costa Rica aftershock sequence: evidence for a transcurrent plate boundary, *J. Geophys. Res.* **98,** 15759-15778.

Frohlich, C. and K. D. Apperson (1992). Earthquake focal mechanisms, moment tensors, and the consistency of seismic activity near plate boundaries, *Tectonics,* **11,** 279-296.

Gephart, J. W., and D. Forsythe (1984). An improved method for determining the regional stress tensor using earthquake focal plane mechanism data; Application to the San Fernado earthquake sequence, *J. Geophys. Res.* **89,** 9395-9320.

Ginzburg, A., W.D. Mooney, A.W. Walter, W.J. Lutter, and J. H. Healy (1983). Deep structure of the Mississippi Embayment, *AAPG Bull.,* **67,** 2031-2046.

Gomberg, J. (1993). Tectonic Deformation in the New Madrid Seismic Zone: Inferences From Map View and Cross-Sectional Boundary Element Models, *J. Geophys. Res.* **98,** 6639-6664.

Gomberg, J. and M. Ellis (1994). Topography and Tectonics of the central New Madrid Seismic Zone: Results of Numerical Experiments Using A Three-Dimensional Boundary Element Program, *J. Geophys. Res.* **99,** 20299-20310.

McKeown, F. A, R. M. Hamilton, S. F. Diehl and E. E. Glick (1990). Diapiric origin of the Blytheville and Pascola arches in the Reelfoot rift, Eastcentral United States: relation to New Madrid seismicity, *Geology,* **18,** 1158-1162.

Haminton, R. M. and M. D. Zoback (1982). Tectonic features of the New Madrid Seismic Zone from seismic reflection profiles, Investigations of the New Madrid, Missouri, Earthquake Region,

Geological Survey Professional Paper 1236. 55-82.

Harkrider, D. G. (1976). Potentials and displacements for two theoretical seismic sources, *Geophy. J. R. astr. Soc.* **47,** 97-133.

Hamilton, R. M. and W. D. Mooney (1990). Seismic-wave attenuation associated with crustal faults in the New Madrid seismic zone, *Science* **248,** 351-354.

Haskell, N. A. (1964). Radiation pattern of surface waves from point sources in a multilayered medium, *Bull. Seis. Soc. Am.* **54,** 377 - 393.

Heaton, T. H. (1978). Generalized Ray Models of Strong Ground Motion, *California Institute of Technology, Ph.D. dissertation.* 292.

Helmberger, D. V. (1968). The crust-mantle transition in the Bering sea, *Bull. Seis. Soc. Am.* **58,** 179-214.

Helmberger, D. V. and D. G. Harkrider (1978). Modeling earthquakes with generalized ray theory, in Modern Problems in Elastic Wave Propagation, Editors: J. Miklowitz and J. Achenbach, John Wiley and Sons, New York. 499-518. Helmberger, D. V. (1983). Theory and application of synthetic seismograms, in Earthquakes: Observation, Theory and Interpretation, Editors: H. Kanamori and E. Boschi, North-Holland for the Italian Physical Society, New York.

Hendricks, J.D., 1988. Bouguer gravity of Arkansas: U.S. Geological Survey Professional Paper **1474,** 31p.

Herrmann, R. B. (1978). A note on causality problems in numerical solution of elastic wave propagation in cylindrical coordinate systems, *Bull. Seis. Soc. Am.* **68,** 117-124.

Herrmann, R. B. (1979b). SH-wave generation by dislocation sources-A numerical study, *Bull. Seis. Soc. Am.* **69,** 1-15.

Herrmann, R. B. (1984). Regional seismograms wavenumber frequency, Computer Programs in Seismology, Sanit Louis University.

Herrmann, R. B. and J. A. Canas (1978). Focal mechanism studies in

the New Madrid Seismic Zone, *Bull. Seis. Soc. Am.* **68,** 1095-1102.

Herrmann, R. B. (1979a). Surface wave focal mechanisms for Eastern North American Earthquakes with Tectonic Implications, *J. Geophys. Res.* **84,** 3543-3552.

Herrmann, R. B., and C. Y. Wang (1985). A comparison of synthetic seismograms, *Bull. Seism. Soc. Am.* **75,** 41-56.

Herrmann, R. B. (1991). Computer Programs in Seismology - VI, Saint Louis University.

Herrmann, R. B. and Charles J. Ammon (1997). Faulting Parameters of Earthquakes in the New Madrid, Missouri Region, *Engineering Geology (in press)*

Hildenbrand. T. G. (1982). Model of Southeastern margin of the Mississippi Valley Graben near Memphis, Tennessee, From interpretation of trunk-magnetometer data, *Geology,* **10,** 467-480.

Hildenbrand, T. G. (1985), Rift structures of the northern Mississippi Embayment from the analysis of gravity and magnetic data, *J. Geophys. Res.* **90,** 12607-12622.

Hildenbrand, T. G., and J. D. Hendricks (1995), Geophysical setting of the Reelfoot rift and relations between rift structures and the New Madrid seismic zone, *U.S.Geol. Surv. Prof. Pap.,* **1528E,** 1-30.

Hildenbrand, T. G., Andrew Griscom, W. R. Van Schmus and W. D. Stuart (1996). Quantitative investigations of the Missouri gravity low: A possible expression of a large, Late Precambrian batholith intersecting the New Madrid seismic zone, *J. Geophys. Res.* **101, B10** 21921-21942.

Himes L, W. Stauder, R. B. Herrmann (1988). Indication of active faults in the New Madrid seismic zone from precise location of hypocenters, *Seismol. Res. lett.* **59(4),** 123-131.

Hough, S. E., J. G. Anderson, J. Brune, F. Vernon, III, J. Berger, J. Fletcher, L. Haar, T. Hanks, and L. Baker (1988). Attenuation near Anza, California, *Bull. Seism Soc. Am.* **78,** 672-691. Howe, J. R.,

and T. L. Thompson (1984). Tectonics, sedimentation, and hydrocarbon potential of the Reelfoot Rift, *Oil Gas J.* **82,** 179-190.

Hudnut, K. W., L. Seeber, and J. Pacheco (1989). Cross-Fault Triggering the November 1987 Superstition hills Earthquake Sequence, Southern California, *Geophy. Res. Letters.* **16,** 199-202.

Hwang, H. J., and B. J. Mitchell (1987). Shear velocities, Q_β, and the frequency dependence of Q_β in stable and tectonically active regions from surface wave observations, *Geophys. J. Roy. Astr. Soc.* **90,** 575 -613.

Johnson, L. R. (1974). Green's functions for Lamb's problem, *Geophys. J. B 37,* 99-131.

Johnston, A. C, S. J. Nava (1985). Recurrence rates and probability estimates for the New Madrid seismic zone, *J. Geophys. Res.* **90,** 6737-6753.

Johnston, A. C. (1996). Seismic moment assessment earthquakes in stable continental regions-III. New Madrid 1811-1812, Charleston 1886 and Lisbon 1755, *Geophys. J. Int.* **126,** 314-344.

Johnston, A. C. and E. S. Schweig (1996). The enigma of the New Madrid earthquakes of 1811-1812, *Annu. Rev. Earth Planet. Sci.* **24,** 339-384.

Jost, M. L. and R. B. Herrmann (1989). A student guide and review of moment tens ors, *Seism. Res. Letters.* **60,** 37-57.

Kane, M. F., T. G. Hildenbrand, and J. D. Hendricks (1981). A model for the tectonic evolution of the Mississippi Embayment and its contemporary seismicity, *Geology* **9,**

Knopoff, L., R. W. Fredericks, A. F. Gangi and L. D. Porter (1957). Surface amplitudes of reflected body waves, *Geophysics,* **22,** 842-847.

Langston, C. A. and D. V. Helmberger (1975). A procedure for modeling shallow dislocation sources, *Geophys. J. R. astr. Soc.* **42,** 117-130.

Langston, C. A. (1981). Source inversion of seismic waveform: the

KOYNA, INDIA, earthquakes of 13 September 1967, *Bull. seism. Soc. Am.* **71,** 1-24.

Lamb, H. (1904). On the propagation of tremors over the surface of an elastic solid, *Phy. Rev.* **51,** 660-676.

Liao, Qingbo and G. A. McMechan (1996). Simulation and analysis of 1991 U. S. Geological Survey refraction data from the New Madrid Seismic Zone, *J. Geophys. Res.* **101,** 27865-27881.

Liu Z., R. B. Herrmann, J. Xie, and E. D. Cranswick (1991). Waveform characteristics and focal mechanisms of five aftershocks of the 1983 Goodnow, New York, earthquake by polarization analysis and waveform modeling, *Seism. Res. Letters.* **62**, 123-133.

Liu Z., M. E. Wuenscher and R. B. Herrmann (1994). Attenuation of body waves in the central New Madrid Seismic Zone, *Bull. Seism. Soc. Am.* **84,** 1112-1122.

Liu Z., R. B. Herrmann and J. Xie (1996). Microearthquake source parameters in the central New Madrid Seismic Zone from waveform modeling, *Seism. Res. letters.* **45,** 45.

Liu Z. and R. B. Herrmann (1996). Seismotectonics of the central New Madrid Seismic Zone, *EOS, Transactions, AGU* **77** 521.

Liu, L., M. D. Zoback and P. Segall (1992). Rapid intraplate strain accumulation in the New Madrid Seismic Zone, *Science,* **257,** 1666-1669.

Maruyama, T. (1964). Statical elastic dislocations in an infinite and semi-infinite medium, *Bull. Earthquake Res. Inst.* **42,** 289-368.

McCamy, K. and R. P. Meyer (1966). Crustal results of fixed multiple shots in the Mississippi Embayment, in *The Earth Beneath the Continents, Geophys. Monogr, Ser.,* **10,** 370-381.

McKeown, F. A. (1978). Hypothesis-Mafic intrusions and their contact zones are source zones of many earthquakes in central and southeastern United States; *U.S. Geological Survey Journal of Research,* **6,** 41-50.

McKeown, F. A., and S. F. Diehl (1994). Evidence of contemporary and ancient excess fluid pressure in the New Madrid seismic zone of the Reelfoot rift, Central United States, *U. S. Geol. Surv. Prof. Pap.,* **1538N,** 1-24.

Mendiguren, J. A. (1977). Inversion of surface wave data in source mechanism studies, *J. Geophys. Res.* **82,** 889-894.

Mitchell, B. J. (1973). Radiation and attenuation of Rayleigh waves from the southeastern Missouri earthquake of October 21, 1965, *J. Geophys. Res.* **78,** 886-899.

Mitchell, B. J. (1975). Regional Rayleigh wave attenuation in North America, *J. Geophys. Res.* **80,** 4904-4916.

Mitchell, B. J. (1980). Frequency dependence of shear wave internal friction in the continental crust of the United States, *J. Geophys. Res.* **85,** 5212-5218.

Mitchell, B. J. (1981). Regional variation and frequency dependence on Q_β in the crust of the United States, *Bull. Seism. Soc. Am.* **71,** 1531-1538.

Mitchell, B. J., O. W. Nuttli, R. B. Herrmann and W. Stauder (1991). Seismotectonics of the central United States, in *Neotectonics of North America,* D. B. Slemmons, E. R. Engdahl, M. D. Zoback and D. D. Blackwell, eds., Geological Society of America, Boulder, pp 245-260.

Mooney, W. D. M. C. Andrews, A. Ginsberg, D. A. Peters and R. M. Hamilton (1983). Crustal structure of the northern Mississippi and a comparison with other continental rift zones, *Tectonophysics,* **94,** 327-348.

Nelson, J. W. and Zhang Jie (1991). A COCORP deep reflection profile across the buried Reelfoot rift, south-central United States, *Tectonophysics* **196,** 1-23.

Nicholson, C. and D. W. Simpson (1984), Crustal Studies Velocity Inversions, and Fault Tectonics: Results From A Microearthquake survey in the New Madrid Seismic Zone, *J. Geophy. Res.* **89,**

4545-4558.

Nuttli, O. W. (1973a). The Mississippi valley earthquakes of 1811 and 1812: intensities, ground motion and magnitude, *Bull. Seis. Soc. Am.* **63,** 227-248.

Nuttli, O. W. (1973b). Seismic wave attenuation and magnitude relations for eastern North America, *J. Geophys. Res.* **78,** 876-885.

Nuttli, O. W. (1978). A time domain study of the attenuation of 10 Hz waves in the New Madrid seismic zone, *Bull. Seism. Soc. Am.* **68,** 343-355.

O'Connell, D. R., C. G. Bufe and M. D. Zoback(1982). Microearthquakes and Faulting in the area of New Madrid, Missouri-Reelfoot lake, Tennessee, in *Investigations of the New Madrid, Missouri, Earthquake Region,* F. A. McKeown and L.C. Pakiser, editors, U.S. Geol. Surv. Prof. Paper, **1236,** 31-38.

Pujol, J., A. Johnston, J.-M. Chiu, Y. T. Yang (1997). Refinement of thrust faulting models for the Central New Madrid seismic zone, *Engineering Geology (in press)*

Russ, D. P. (1982). Style and Significance of surface Deformation in the Vicinity of New Madrid Missouri, in *Investigations of the New Madrid, Missouri, Earthquake Region,* F.A. McKeown and L. C. Pakiser, editors, *U. S. Geol. Surv. Prof. Paper,* **1236,** 95-114.

Saikia, C. K. (1985). Waveform modeling of eastern north american earthquakes using short-distance recordings, Ph.D Dissertation, Saint Louis University.

Saikia, C. K. and R. B. Herrmann (1985). Application of waveform modeling to determine focal mechanisms of four 1982 Miramichi aftershocks, *Bull. Seis. Soc. Am.* **75**, 1021-1040.

Saikia, C. K. and R. B. Herrmann (1986). Moment-Tensor Solutions For Three 1982 Arkansas Swarm Earthquakes by Waveform Modeling, *Bull. Seis. Soc. Am.* **76,** 709-723.

Saikia, C. K. and R. B. Herrmann (1987). Determination of focal

mechanism solutions for four earthquakes from Monticello, South Carolina, and crustal structure by waveform modeling, *Geophys. J. R. Astr. Soc.* **90**, 669-691.

Schweig E. S and M. A. Ellis (1994). Reconciling short recurrence intervals with minor deformation in the New Madrid seismic zone, *Science,* **264,** 1308-1311.

Schwartz, S. Y. (1995). Source parameters of aftershocks of the 1991 COSTA RICA and 1992 CAPE MENDOCINO, CALIFORNIA earthquakes from inversion of local amplitude ratios and broadband waveforms, *Bull. Seis. Soc. Am.*

Segall, P. and D. D. Pollard (1980). Mechanics of Discontinuous Faults, *J. Geophys. Res.* **85,** 4337-4350.

Sexton, J. L. and P. B. Jones (1986). Evidence for Recurrent Faulting in the New Madrid Seismic Zone From Mini-Sosie High-Resolution Reflection Data, *Geophysics,* **51,** 1760-1788.

Singh, S. and R. B. Herrmann (1983). Regionalization of crustal coda Q in the continental United States, *J. Geophys. Res.* **88,** 527-538.

Stauder, W., M. Kramer, G. Fischer, S. Schaefer and S. T. Morrissey (1976). Seismic characteristics of southeast Missouri as indicated by a regional telemetered microearthquake array, *Bull. Seis. Soc. Am.* **66,** 1953-1964.

Stearns, R. G. and M. V. Marcher (1962). Late Cretaceous and subsequent structural development of the northern Mississippi Embayment area, *Geol. Soc. Am. Bull.,* **73,** 1387-1394.

Steinhart, S. W., and R. P. Meyer (1961). Explosion studies of continental structure, Carnegie Inst. Washington Publ. 622.

Stuart, W. D. and T. G. Hildenbrand (1994). Stress concentration mechanisms for the New Madrid seismic zone, *Eos Trans. AGU, 75(44), Fall Meet. Suppl.,* **179,** 1994.

Swanberg, C. A., Mitchell, B. J. and Lohse, R. L. (1982). Heat Flow in the upper Mississippi embayment, Investigations of the New

Madrid, Missouri, Earthquake Region, Geological Survey Professional Paper 1236, 185-189.

Taylor, K. B. and M. E. Wuenscher (1990). Special investigations of seismic Activity: The Ripley, Tenn. earthquake of 29 Aug. 1990 and the New Hamburg, Missouri Earthquake of 26 Sept. 1990, *Central Mississippi Valley Earthquake Bulletin* **65,** July 01-September 30, 1990.

Thomas, W. A. (1991). The Appalachian-Ouachita rifted margin of southeastern North America, *Geol. Soc. Am. Bull.* **103,** 415-431.

Van Arsdale R. B, K. I. Kelson, C. H. Lumsden (1995). Northern extension of the Tennessee Reelfoot scarp into Kentucky and Missouri, *Seismol. Res. lett.* **66,** 57-62.

Velasco, A. A., C. J. Ammon and T. Lay (1994). Empirical Green function deconvolution of broadband surface waves: rupture directivity of the 1992 Landers, California (M_W = 7.3), earthquke, Bull. Seis. Soc. Am. **84,** 735-750.

Wang, C. Y. and R. B. Herrmann (1980). A numerical study of P-, SV-, and SH-wave generation in a plane layered medium, *Bull. Seis. Soc. Am.* **70,** 1015-1036.

Woolery, E. W., R. Street, Z. Wang and J. Harris (1993). Near-surface deformation in the New Madrid Seismic Zone as imaged by high resolution SH-wave seismic methods, *Seism. Res. Letters.* **20,** 1615-1618.

Woolery, E. W., Z. Wang, R. L. Street and J. B. Harris (1996). A P- and SH-wave seismic reflection investigation of the Kentucky bend scarp in the New Madrid Seismic Zone, *Seism. Res. Letters.* **67, NO. 2** 67-74.

Xie, J., Z. Liu, R. B. Herrmann, and E. Cranswick (1991). Source processes of three aftershocks of the 1983 Goodnow, New York earthquake: High resolution images of small, symmetric ruptures, *Bull. Seism. Soc. Am.* **81** 818-843.

Xie, J., Z. Liu, L. Cong, R. B. Herrmann and J.-M., Chiu (1997).

Rupture properties of clustered microearthquakes near intersecting intraplate faults of New Madrid Seismic Zone: Implication on fault weakening *J. Geophys. Res.* **102,** 8187-8202.

Yang, Y. T., J.-M. Chiu, K. C. Chen, Z. S. Liaw, S. C. Chiu and A. C. Johnston (1995). Single-event, first motion, focal mechanism studies in the central NMSZ using PANDA data (unpublished manuscript), University of Memphis.

Zhao Dapeng, Kanamori Hiroo, Hiroaki Negishi, D. A.. Wiens, (1996). Tomography of the Source area of the 1995 Kobe earthquake: Evidence for fluids at the hypocenter? *Science,* **274,** 1894.

Zoback, M. D., R. M. Hamilton, A. J. Crone, D. P. Russ, F. A. McKeown, S. R. Brockman (1980). Recurrent intraplate tectonism in the New Madrid seismic zone, *Science,* **209,** 971-976.

Zoback, M. L. and M. D. Zoback (1989). Tectonic stress field of the continental United States, in Pakiser, L. C. and W. D. Mooney, eds, Geophysical Framework of the Continental United States, *Geol. Soc. Am.* **172**, Boulder, Colorado, 525-539.

Zoback, M. L. and M. D. Zoback (1991). Tectonic stress field of North America and relative plate motions, in *Neotectonics of North America,* D. B. Slemmons, E. R. Engdahl, M. D. Zoback and D. D. Blackwell, eds., Geological Society of America, Boulder, 339-366.

VITA AUCTORIS

Zuyuan Liu was born in Changsha, Hunan Province, China on February 15, 1945. He attended the Peking University, Beijing, China and received Bachelor of Science degree in geophysics in 1969.

From 1969 to 1979, he served at the Hunan Seismological Bureau, Changsha as an Assistant Engineer. After that he attended the University of Science and Technology of China, Beijing, and received a Master of Science degree in Seismology in 1982. From March 1982 to 1986, He joined the Institute of Geology, State Seismological Bureau of China (SSB, Beijing, China) as a Senior Researcher in March 1982 and remained there until 1986. In September 1986 he was invited by the late Dr. Otto Nuttli to come to the United States as an exchange visiting scholar. Since January 1991, he has been a Ph.D student in the Department of Earth and Atmospheric Sciences of Saint Louis University. He was employed by the same department as a graduate research assistant during his graduate study.